Precision Measurement of the Proton's Weak Charge using Parity-Violating Electron Scattering

Wade S. Duvall

Dissertation submitted to the Faculty of the
Virginia Polytechnic Institute and State University
in partial fulfillment of the requirements for the degree of

Doctor of Philosophy
in
Physics

Mark L. Pitt, Chair
Patrick Huber
Leo E. Piilonen
Eric R. Sharpe
John H. Simonetti

October 19, 2017
Blacksburg, Virginia

Keywords: nuclear physics, electromagnetic, electroweak, parity violation, symmetry, proton, weak charge, Qweak

Precision Measurement of the Proton's Weak Charge using Parity-Violating Electron Scattering

Wade S. Duvall

(ABSTRACT)

The Q_{weak} experiment has precisely determined the weak charge of the proton Q_w^p by measuring the parity-violating asymmetry in elastic electron-proton scattering at a low momentum transfer of $Q^2 = 0.0249$ $(\text{GeV}/c)^2$. Q_w^p has a definite prediction in the Standard Model, and a value of $\sin^2\theta_W$ can be extracted from it for comparison with other neutral current observables. Q_{weak} measured the weak charge of the proton to be $Q_w^p(PVES) = 0.0719 \pm 0.0045$, which is consistent with the Standard Model value of $Q_w^p(SM) = 0.0708 \pm 0.0003$.

Q_{weak} ran at the Thomas Jefferson National Accelerator Facility for two and a half years and was installed in experimental Hall C. A 180μA beam of longitudinally polarized electrons at 1.16 GeV scattered off a liquid hydrogen target of unpolarized protons. The electrons were collimated to an acceptance of 5.8° to 11.6° and then passed through a magnetic spectrometer and onto quartz Čerenkov detector bars.

A detailed description of the theory and motivation behind the Q_{weak} experiment is given. An overview of the Q_{weak} apparatus and an in-depth discussion of the luminosity monitor performance is presented. A general overview of the Q_{weak} analysis is also presented, with a focus on the beamline background correction, the nonlinearity measurement, and the simulation to constrain error for a rescattering effect. Also detailed here is the final, unblinded Q_{weak} result, which determined Q_w^p to 6.2% and provided the highest precision measurement of $\sin^2\theta_W$ at low energy.

Precision Measurement of the Proton's Weak Charge using Parity-Violating Electron Scattering

Wade S. Duvall

(GENERAL AUDIENCE ABSTRACT)

Q_{weak} is a precision-frontier accelerator driven experiment that took place at Thomas Jefferson National Accelerator Facility. Precision-frontier exists alongside the better known energy-frontier (which includes well known labs like the Large Hadron Collider) and refers to experiments which precisely measure values which are predicted by the latest theory. Deviations in these measurements help rule out theories and are used by energy-frontier experiments to know where to look for new physics. The Q_{weak} experiment measured the weak charge of the proton, which can be though of as the weak analog to electric charge. This value has never been measured before, and, since it is predicted to be small by current theory, is a good place to look for new physics. The value measured by this experiment indicates good agreement with the current theory. Even though there is good agreement with theory, Q_{weak} is an important result which will help define future physics models.

In this thesis is an overview of the theoretical motivation of Q_{weak}, a general overview of the experimental design, in-depth discussion of the background detectors, general overview of the analysis with detailed descriptions of the several important corrections.

Acknowledgments

First I would like to thank my advisor Mark Pitt for all his help and understanding through the last seven years. I am grateful for the opportunity to work with Mark on Q_{weak} as well as making graduate school a wonderful experience. I would also like to thank the entire Q_{weak} collaboration, without whom none of this would have been possible. I would especially like to thank the senior Q_{weak} collaborators who I have worked closely with during my time as a graduate student. Kent Paschke for his invaluable feedback and help on many topics, Greg Smith for being helpful and understanding even when giving all of his time to Q_{weak} publications, Dave Mack for always being available to bounce ideas off, and Paul King for always helping with software tasks, and for not being mad when I crashed CEBAF with a database query. I would also like to thank Roger Carlini and Wim van Oers for all their work promoting Q_{weak}. Finally, I would like to thank my committee, Patrick Huber, Leo Piilonen, Eric Sharpe and John Simonetti for their help.

I would like to thank the friends I made during my time at Q_{weak}. I would like to thank John Leacock, in whose footsteps I followed, for all of the help, explanations, and assistance when I was just starting out in Q_{weak}; also for his friendship during and after his time at Virginia Tech, and for his professional help after he left. I would also like to thank the beam corrections group, particularly Peng Zang for his invaluable work; the PMTDD group, particularly

Ciprian Gal for putting much of his postdoc into this unexpected correction and for taking the time to help me often; and the beamline background group, particularly Emmanouil Kargiantoulakis for his valuable help. Scott MacEwan for all his help with ROOT and for being an great office mate; Buddhini Waidyawansa, Rakitha Beminiwattha, and Josh Magee for making me feel welcome and helping explain the Q_{weak} experiment; Martin McHuge, Juan Carlos Cornejo, and Kurtis Bartlett for the invaluable help writing software. I would especially like to thank Anna Lee, whose emotional support and assistance with many aspects of Q_{weak} helped me get to where I am today.

Writing a dissertation takes a lot of work and effort, so I would like to thank everybody who helped me get through this period. I would especially like to thank Phil Dick, whose brilliance and sacrifice were invaluable in the past few months. To all my friends, Kristen Brown, Blair Crawford, Mitch Davis, Marc Fitzgerald, Lynn Langley, Zack Lewis, Kyle Racette, William Rotondi, Calvin Winkowski, and Zach Yokley, thank you for your support. Finally, I would like to thank my family, Jeffrey and Susan Duvall, for their love and support.

Contents

List of Figures

List of Tables

Chapter 1

Introduction

This thesis will describe the precision measurement of the weak charge of the proton, Q_w^p. Q_w^p was measured by scattering polarized electrons off unpolarized protons. This measurement was taken using the Q_{weak} apparatus, which was designed and built specifically for this purpose. Details on the apparatus components will be given in chapter 3, with more in-depth details on the upstream luminosity monitors in chapter 4. An overview of the analysis is given in chapter 5, with more details on the beamline background (section 5.3.3), the nonlinearity measurement (section 5.3.4), and the simulation to constrain errors on a rescattering effect (section 5.3.6).

The measurement was done by determining the asymmetry between the positive and negative helicity states. This is done such that the experiment is only sensitive to interference between the electromagnetic and weak interactions. Since electromagnetic interactions are

parity conserving and weak interactions are parity-violating, the asymmetry ensures Q_{weak} is sensitive to the parity-violating weak interaction magnitude.

Q_{weak} is a precision, intensity frontier Standard Model (SM) test and search for new physics. Q_w^p can be extracted from the elastic electron-proton asymmetry. This measurement is made at low momentum transfer $Q^2 = 0.0249$ $(\text{GeV}/c)^2$ to increase sensitivity to Q_w^p and reduce sensitivity to hadronic effects. Any statistically significant deviations from the Standard Model predicted value would indicate new physics, with sensitivity and mass reach to be determined by the final error bar on Q_w^p.

The Q_{weak} apparatus consisted of a ring of eight quartz Čerenkov main detector bars, three lead collimators, a spectrometer magnet, and a 35 cm long liquid hydrogen target. Jefferson Lab Continuous Electron Beam Accelerator Facility (CEBAF) provided 89 ± 1.8 % longitudinally polarized electrons at an energy of 1.115 GeV and 180 μA nominally. This experiment follows from a long line of parity-violating electron scattering (PVES) experiments which laid the groundwork for Q_{weak} in terms of hadronic data and experimental techniques.

Q_{weak} is the first direct measurement of weak charge of the proton to a precision of 6.2%. The weak charge is a fundamental property of the proton and is the weak analog to the electromagnetic charge. Q_{weak} also measured the weak mixing angle $\sin^2\theta_W$ to a precision of 0.47%. The running of the weak mixing angle vs energy transfer is show in Figure 1.1.

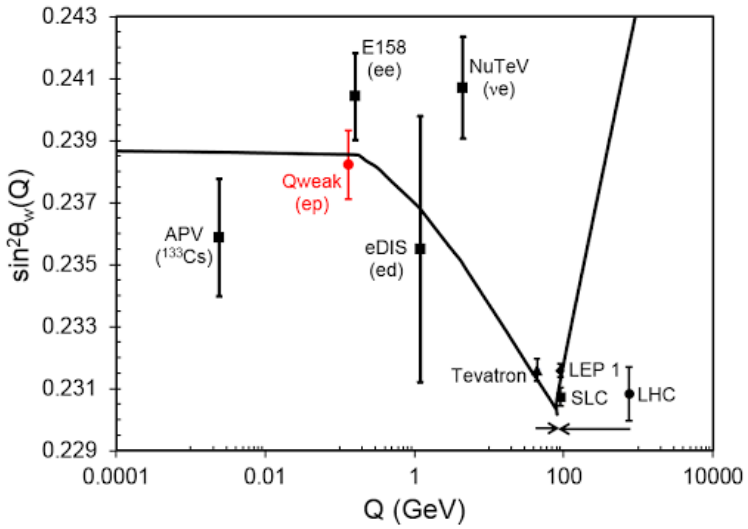

Figure 1.1: The calculated running of the weak mixing angle in the Standard Model, as defined in the modified minimal subtraction scheme, is shown as the solid line. The black data points are from published results: Atomic Parity Violation (APV), parity-violating Møller scattering (SLAC E158), deep inelastic neutrino-nucleus scattering (NuTeV), and the Z-pole measurements at LEP and SLC. The red data point shows the final Q_{weak} result [11].

At tree level, the weak charge is related to $\sin^2\theta_W$ as $Q_w^p = 1 - 4\sin^2\theta_W$. θ_W, the weak mixing angle, governs the mixing of the neutral weak and electromagnetic currents as

$$\begin{pmatrix} B_\mu \\ W_\mu^3 \end{pmatrix} = \begin{pmatrix} \cos\theta_W & -\sin\theta_W \\ \sin\theta_W & \cos\theta_W \end{pmatrix} \begin{pmatrix} A_\mu \\ Z_\mu \end{pmatrix}, \tag{1.1}$$

which shows how the observed γ and Z^0 neutral bosons are actually a mixture of B_μ and W_μ^3 gauge fields. See section 2.3.1 for details.

In addition to measuring Q_w^p, Q_{weak} took several ancillary measurements at a variety of beam energies and on a variety of targets. This includes the transverse parity-conserving transverse

LH_2 asymmetry, the asymmetry on Al, the $N \rightarrow \Delta$ asymmetry at two beam energies, and several other measurements.

1.1 Physics motivation

The Standard Model of electroweak physics has been precisely tested at very low and high energies by Atomic Parity Violation (APV), by measurements at the Z-pole by SLAC and LEP, and by Møller scattering at SLAC. Q_{weak} offers a medium energy measurement to help determine the running of $\sin^2\theta_W$ at low Q^2.

Purely by luck, the $Q_w^p = 1 - 4\sin^2\theta_W$ is suppressed in the Standard Model since $4\sin^2\theta_W$ is very close to 1. Compared this to the weak charge of the neutron, $Q_W^n = -1$. This means that in order to observe new physics via scattering off the proton, you would need to be much less precise than you would need to be to observe the same effect with scattering off the neutron. Also, experiments with both protons and neutrons have to make significant many-body atomic structure corrections.

Q_{weak} also has to make a many-body correction arising from the fact that the proton is made up of quarks. This correction is small due to the low Q^2 of the experiment. Thanks to a series of experiments, including G0 [9, 18] and PV-A4 [21, 69, 70], which measured the strange form factors, the error arising from the proton structure is acceptable.

Unlike energy frontier experiments such as CMS [28] and ATLAS [2], Q_{weak} is sensitive to both high energy and low energy physics beyond the Standard Model (BSM). Some possible

examples of new high energy physics to which Q_{weak} would be sensitive include B-L violating supersymmetry (supersymmetry where baryon and lepton number are no longer conserved), and leptoquarks (which would imply a new boson that transforms an electron into an up quark) [48]. An example of new low energy physics to which Q_{weak} is sensitive is the dark Z boson (a theoretical particle which would link the weak and dark sectors) [30]. The dark Z boson would couple ordinary particles in the electroweak Standard Model to dark matter particles. The existence of dark matter particles is one possible explanation for discrepancies in the amount of matter astronomically observed versus the amount of matter indicated by gravitational effects.

Chapter 2

Theory

2.1 Introduction

The electron has long been a useful probe for studying the structure of matter as the electron itself has no structure. This makes its interactions with matter well understood without complex structure corrections. It has been used in both direct, high energy experiments as well as precision, parity-violating experiments, like Q_{weak}. Q_{weak} makes use of a large set of previous PVES experiments [4, 7, 9, 13, 14, 15, 18, 21, 56, 69, 70, 90] which helped to pioneer precision techniques as well as help to reduce errors arising from the proton structure (via precision measurements of proton form factors).

Q_{weak} measured the parity-violating asymmetry produced by scattering longitudinally polarized electrons elastically on a target of unpolarized protons at low momentum transfer

($Q^2 = 0.0249$ (GeV/c)^2) and forward angle. The low momentum transfer and forward angle makes the experiment more sensitive to Q_w^p as well as reduces the correction from hadronic contributions.

2.2 The Standard Model

The Standard Model [25] is, at present, the theory which best describes the interactions of matter. It has a few major flaws (most importantly, it does not include gravitation or explain dark matter) and many unsatisfactory explanations (such as the hierarchy problem) but it represents the best model upheld by physical results.

Within the Standard Model, particles are broken up into three families: leptons, quarks, and gauge bosons. There is also the standalone Higgs boson [47, 55]. Figure 2.1 shows the three families and gives the mass, charge, and spin of the particles. There are three generations of leptons and quarks, though the Standard Model offers no special significance to the number 3. Quarks and leptons make up all known matter.

The gauge bosons are spin 1 particles that carry force. The gluon is the force carrier for the strong force, and only couples to quarks and other gluons. The photon (γ), Z^0 boson, and $W^{\pm}$ bosons are the force carriers for the electroweak forces. Electrons and quarks can couple with all three, but neutrinos are only able to couple via Z^0 and $W^{\pm}$ bosons, not γ. The Higgs boson is a newly discovered spin 0 boson [3] whose presence explains why some bosons whose symmetry indicate they should be massless in fact have mass.

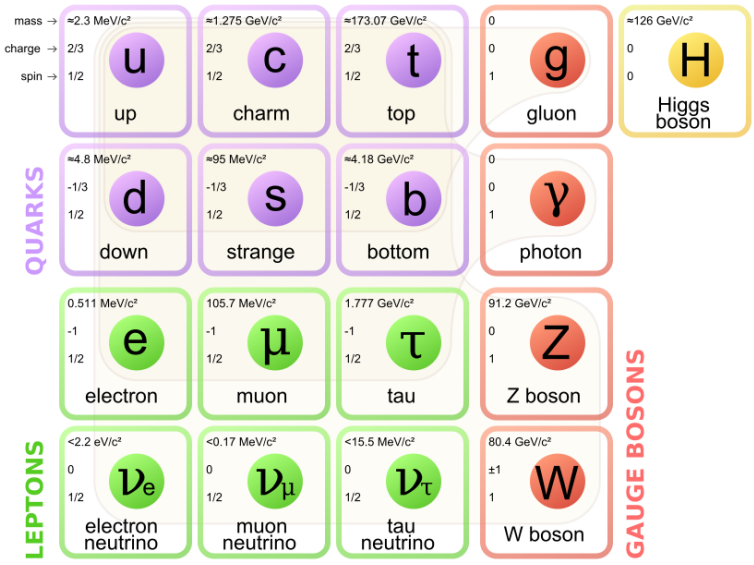

Figure 2.1: All known particles within the Standard Model. The three main groups of fermions are shown as well as the gauge bosons and Higgs boson. Image from PDG [85].

2.3 Electroweak interaction and parity violation

As stated in the introduction, the electroweak interaction is how the electromagnetic and weak force manifest themselves in the Standard Model. The electroweak force undergoes spontaneous symmetry breaking at energies near the mass of its mediating particles, the Z^0 (mass 91.1876 GeV/c^2) and $W^{\pm}$ (mass 80.385 GeV/c^2) [85]. The Z^0 is the force carrier for the neutral current reaction and the $W^{\pm}$ is the force carrier for the charged current reaction. The masses of the two are related though the Weinberg angle (or weak mixing angle) as θ_W as $M_W^2 = M_{Z^0}^2 \cos^2 \theta_W$ [98].

The weak force is often made analogous to the electromagnetic force, but there are a few important differences. The weak force has a very short range, and the interactions violate parity (i.e. physics is not preserved under parity operation). For example, the parity opera-

tion $\mathbf{P}$ on the three-momentum vector $\mathbf{k}$ would be

$$\mathbf{k}'(x, y, z) = \mathbf{P}\mathbf{k}(x, y, z) = \mathbf{k}(-x, -y, -z) = -\mathbf{k}(x, y, z), \tag{2.1}$$

where $\mathbf{k}'$ is the parity operated three-momentum vector. Note that the parity operator preserves the magnitude of $\mathbf{k}$ as $|\mathbf{k}| = |\mathbf{k}'| = |-\mathbf{k}|$.

Parity is conserved for the electromagnetic and strong interactions, and was assumed to be conserved for the weak interaction as well, until, in 1950's, Chen Ning Yang and Tsung-Dao Lee proposed that weak interactions may in fact violate parity [67]. This was confirmed in 1957 by Chien Shiung Wu and collaborators after conducting an experiment which measured the angular distribution of gamma rays emitted by β decay of polarized ^{60}Co [100]. The ^{60}Co was polarized by a magnetic field at very low temperature. The result showed that the decay beta particles were emitted preferentially antiparallel to the spin of the ^{60}Co by 60%. If parity was conserved, there would have been no preference toward either direction.

2.3.1 Electroweak unification

In the Standard Model, all interactions between leptons and quarks are mediated by virtual bosons, i.e. bosons that do not materialize and cannot be observed. For example, in the case of an electron scattering off a proton, the only possible exchange bosons are the Z^0 or the γ since the particles must be neutral to conserve charge and the electron can only couple to the proton via the weak or electromagnetic forces.

The mathematical formulation of the electroweak bosons in the Standard Model can be written as the electroweak Lagrangian [25]

$$\mathcal{L}_{\mathrm{EW}}^{\mathrm{MT}} = -\frac{1}{8}g'^2v^2\left|W_\mu^1 - iW_\mu^2\right|^2 - \frac{1}{8}v^2\left(g'^2B_\mu - g^2W_\mu^3\right)^2, \tag{2.2}$$

where W_μ^α and B_μ are the four-gauge fields, g and g' are the field coupling constants and v is the vacuum expectation value. It is important to note that the gauge fields W_μ^1 and W_μ^2 mix together, and separately, the fields W_μ^3 and B_μ mix together, allowing them to be treated individually.

The kinetic portion of the Lagrangian is equal to

$$-\frac{1}{2}M^2K^\mu K_\mu, \tag{2.3}$$

where M is the mass of the corresponding field and K is the four-momentum. By comparing the quadratic terms of the kinetic portion of the Lagrangian and equation 2.2, it is possible to determine the masses. For example, by comparing the quadratic term of $W_\mu^1W^{\mu 1}$ to equation 2.3, the mass can be determined as

$$-\frac{1}{2}M^2 = -\frac{1}{8}g'^2v^2, \tag{2.4}$$

$$M^2 = \frac{1}{4}g'^2v^2. \tag{2.5}$$

A similar result is found for $W_\mu^2 W^{\mu 2}$. These fields can be written as mass eigenstates and are invariant under electromagnetic charge Q, $Q = T_3 + Y$ where T is the $SU_c(3)$ isospin and Y is the weak hypercharge [25]. These fields can be defined as the real charged gauge bosons of the weak force as

$$W_\mu^+ \equiv \frac{1}{\sqrt{2}} \left(W_\mu^1 - i W_\mu^2 \right), \tag{2.6}$$

$$W_\mu^- \equiv \frac{1}{\sqrt{2}} \left(W_\mu^1 + i W_\mu^2 \right), \tag{2.7}$$

which are the same $W^\pm$ bosons discussed in section 2.3. They have identical mass, which can be determined from 2.5 to be

$$M_{W_\mu^\pm} = \frac{1}{2} g' v. \tag{2.8}$$

For the remaining W_μ^3 and B_μ fields, follow the same procedure for the second half of equation 2.2. Define two new vectors as the mass eigenstates described by the gauge fields as

$$Z_\mu = -B_\mu \sin\theta_W + W_\mu^3 \cos\theta_W, \tag{2.9}$$

$$A_\mu = B_\mu \cos\theta_W + W_\mu^3 \sin\theta_W. \tag{2.10}$$

The sine and cosine of the weak mixing angle are defined in terms of g and g' as

$$\begin{aligned} \sin\theta_W &\equiv \frac{g}{\sqrt{g^2 + g'^2}}, \\ \cos\theta_W &\equiv \frac{g'}{\sqrt{g^2 + g'^2}}. \end{aligned} \tag{2.11}$$

To determine the masses of the bosons as before, transform back to W_μ^3 and B_μ with the mixing relation

$$\begin{pmatrix} B_\mu \\ W_\mu^3 \end{pmatrix} = \begin{pmatrix} \cos\theta_W & -\sin\theta_W \\ \sin\theta_W & \cos\theta_W \end{pmatrix} \begin{pmatrix} A_\mu \\ Z_\mu \end{pmatrix}. \tag{2.12}$$

Apply equation 2.2 to equation 2.12 to obtain

$$-\frac{1}{8}v^2\left[-Z_\mu\left(g'\cos\theta_W + g\sin\theta_W\right) + A_\mu\left(-g'\sin\theta_W + g\cos\theta_W\right)\right]^2, \tag{2.13}$$

which, when the quadratic terms are compared with equation 2.3 gives the masses to be

$$M_{Z_\mu} = \frac{1}{2}v\left(g'\cos\theta_W + g\sin\theta_W\right), \tag{2.14}$$

$$M_{A_\mu} = \frac{1}{2}v\left(-g'\sin\theta_W + g\cos\theta_W\right). \tag{2.15}$$

If these masses are combined with equations 2.11, they reduced to

$$M_{Z_\mu} = -\frac{1}{2}v\sqrt{g^2 + g'^2}, \tag{2.16}$$

$$M_{A_\mu} = 0. \tag{2.17}$$

The Z_μ field corresponds to the massive neutral weak boson Z^0 and the A_μ corresponds to the massless neutral electromagnetic boson γ, or photon. Thus, the neutral electroweak interaction is a combination of electromagnetic and weak interactions, and equation 2.12 governs how this mixing occurs.

2.3.2 The weak charge

The concept of electromagnetic charge and the underlying theory is well understood. Here, the analog of a weak charge will be established for the electroweak interaction. Take the fermion kinetic terms from the invariant Standard Model Lagrangian

$$\mathcal{L}_{\text{EW}} = -\frac{1}{2}\bar{L}_m \not{D} L_m - \frac{1}{2}\bar{E}_m \not{D} E_m - \frac{1}{2}\bar{Q}_m \not{D} Q_m - \frac{1}{2}\bar{U}_m \not{D} U_m - \frac{1}{2}\bar{D}_m \not{D} D_m, \tag{2.18}$$

where L_m and E_m are the left and right hand lepton terms, Q_m is the electromagnetic terms of the quarks, and U_m and D_m are the up- and down-like terms. Equation 2.18 uses Feynman slash notation with $\not{D} = \gamma^\mu D_\mu$. In order to develop the weak charge, only take terms that interact though the neutral gauge field A_μ and the neutral weak field Z_μ. These interactions are shown in figures 2.2a and 2.2b respectively.

(a) Electromagnetic interaction via γ

(b) Weak interaction via Z^0 boson

Figure 2.2: The neutral current exchanged vertices for some fermion f where either a Z^0 or γ is exchange, leaving the fermion unaltered. (TikZ [92] courtesy of J.C. Cornejo.)

Expanding equation 2.18 in terms of the mass eigenstates and only taking the neutral current terms of W_μ^3 and B_μ gives

$$\mathcal{L}_{\mathrm{EW}}^{\mathrm{NC}} = \sum_i \left[-\bar{\psi}_i \gamma^\mu P_{\mathrm{L}} \left(-ig' W_\mu^3 T_3 - igB_\mu Y_{\mathrm{L}} \right) \psi_i - \bar{\psi}_i \gamma^\mu P_{\mathrm{R}} \left(-igB_\mu Y_{\mathrm{R}} \right) \psi_i \right], \tag{2.19}$$

where ψ_i is any given fermion spinor, and P_{L} and P_{R} are the left and right projection operators given as

$$\begin{aligned} P_{\mathrm{L}} &= \frac{1}{2}\left(1 - \gamma^5\right), \\ P_{\mathrm{R}} &= \frac{1}{2}\left(1 + \gamma^5\right). \end{aligned} \tag{2.20}$$

Using the weak mixing matrix (given in equation 2.12), it is possible to rewrite equation 2.19 in terms of the gauge fields Z_μ and A_μ as

$$\begin{aligned} \mathcal{L}_{\mathrm{EW}}^{\mathrm{NC}} = \textstyle\sum_i \quad & [ig' \cos\theta_W \bar{\psi}_i \gamma^\mu P_{\mathrm{L}} Z_\mu T_3 \psi_i + ie\bar{\psi}_i \gamma^\mu P_{\mathrm{L}} A_\mu T_3 \psi_i \\ & + ie\bar{\psi}_i \gamma^\mu P_{\mathrm{L}} A_\mu Y_{\mathrm{L}} \psi_i + -ig \sin\theta_W \bar{\psi}_i \gamma^\mu P_{\mathrm{L}} Z_\mu T_{\mathrm{L}} \psi_i \\ & + ie\bar{\psi}_i \gamma^\mu P_{\mathrm{R}} A_\mu Y_{\mathrm{R}} \psi_i - ig \sin\theta_W \bar{\psi}_i \gamma^\mu P_{\mathrm{R}} Z_\mu Y_{\mathrm{R}} \psi_i], \end{aligned} \tag{2.21}$$

where $e \equiv g\cos\theta_W = g' \sin\theta_W$.

From the previous section, $Q = T_3 + Y$, and given that no right-handed neutrinos have been observed [85], and consequently, the Standard Model was designed to not have any, it can be assumed that the weak hypercharge for right-handed fermions is the electromagnetic charge Q, and thus

$$Q = T_3 + Y_{\mathrm{L}} = Y_{\mathrm{R}}. \tag{2.22}$$

Taking only terms with A_μ and rewriting Y_L and Y_R in terms of Q to derive the electromagnetic portion of the Lagrangian

$$\mathcal{L}_\mathrm{EM} = \sum_i ieQ_i\bar{\psi}_i\gamma^\mu(P_\mathrm{L} + P_\mathrm{R})A_\mu\psi_i, \tag{2.23}$$

$$= \sum_i ieQ_i\bar{\psi}_i\gamma^\mu A_\mu\psi_i, \tag{2.24}$$

where, in equation 2.24, $P_\mathrm{L} + P_\mathrm{R} = 1$. It becomes clear that e represents the electromagnetic coupling constant though careful choice in equation 2.22. It is also possible to define the electromagnetic neutral current as

$$j^\gamma_\mu \equiv Q_i\bar{\psi}_i\gamma^\mu\psi_i. \tag{2.25}$$

As before, now taking only the Z_μ terms from equation 2.21, gives the weak Lagrangian as

$$\mathcal{L}_\mathrm{weak} = \sum_i i\left(g'\cos\theta_W + g\sin\theta_W\right)\bar{\psi}_i\gamma^\mu P_\mathrm{L}Z_\mu\psi_i - igQ\sin\theta_W\bar{\psi}_i\gamma^\mu Z_\mu\psi_i. \tag{2.26}$$

With some manipulation, and by defining

$$\begin{aligned} g_V &\equiv 2T_3 - 4Q\sin^2\theta_W, \\ g_A &\equiv 2T_3, \end{aligned} \tag{2.27}$$

equation 2.26 can be rewritten as

$$\mathcal{L}_{\text{weak}} = \frac{ig'}{4\cos\theta_W} \sum_i \left[\bar{\psi}_i \gamma^\mu \left(g_V - g_A\gamma^5\right) Z_\mu \bar{\psi}_i\right]. \tag{2.28}$$

As for the electromagnetic case, careful choice of g_V and g_A results in the weak vector and axial-vector couplings, and the neutral current can be written as

$$j_\mu^{Z^0} \equiv \bar{\psi}_i \gamma^\mu (g_V - g_A\gamma^5)\psi_i. \tag{2.29}$$

Table 2.1: Fermions and their electromagnetic and weak couplings. See equation 2.27

Fermion	Particle	Q	g_V	g_A
Leptons	ν_e, ν_μ, ν_τ	0	1	-1
	e, μ, τ	-1	$-1 + 4\sin^2\theta_W$	-1
Quarks	u, c, t	$\frac{2}{3}$	$1 - \frac{8}{3}\sin^2\theta_W$	1
	d, s, b	$-\frac{1}{3}$	$-1 + \frac{4}{3}\sin^2\theta_W$	1

In equation 2.25, the electromagnetic charge of the fermion is represented by Q_i. By comparing to this to equation 2.29, it is clear that there are two coupling constants, the weak vector coupling constant g_V and the weak axial-vector coupling constant g_A, are the components of the weak charge. This weak charge is named as such only as an analogy to the electromagnetic charge. Table 2.1 contains a list of all of the fermions in the Standard Model and their electroweak coupling constants.

2.4 Elastic electron-proton scattering

Electron-proton scattering, as discussed in the previous section, only involves electroweak interactions. This is much simpler than hadron-hadron scattering, where there is also a strong force coupling. There is a hadronic structure contribution since the proton is made up of quarks, but this contribution is dependent on the momentum transfer. The electron has no known structure. By design, the Q_{weak} experiment runs at low Q^2 so it is not dominated by hadronic effects. To make matters even simpler, Q_{weak} only detects elastic scattering processes (there is some small fraction of inelastic scattered electrons, for which a correction is applied). At tree level, there are only two Feynman diagrams that contribute to the interaction, shown in figure 2.3.

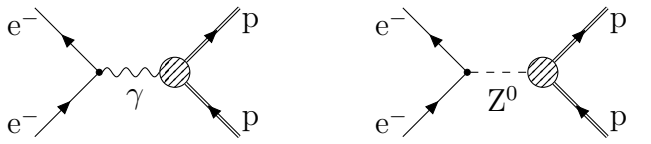

(a) Electron scattering via photon

(b) Electron scattering via Z^0 boson

Figure 2.3: Tree level Feynman diagrams for electroweak interactions between electron and proton. γ is the electromagnetic exchange boson an Z^0 is the neutral weak exchange boson. (TikZ [92] courtesy of J.C. Cornejo.)

This section will discuss the derivation of the parity-violating asymmetry from the Feynman diagrams in figure 2.3.

2.4.1 Electroweak cross sections and form factors

In the previous section, the neutral currents arising from the exchange of the electromagnetic boson γ and the weak boson Z^0 were derived in section 2.3.2 and are reproduced below

$$j_\mu^\gamma \equiv Q_i \bar{\psi}_i \gamma^\mu \psi_i, \tag{2.30}$$

$$j_\mu^{Z_\mu} \equiv \bar{\psi}_i \gamma^\mu (g_V - g_A \gamma^5) \psi_i. \tag{2.31}$$

Henceforth, j_μ^V refers to the current from elementary fermions (i.e. leptons or quarks) exchanging boson V, and J_μ^V refers to the charge current from from composite hadrons (i.e. baryons and mesons) exchanging boson V. It is possible to write the scattering matrix of the electromagnetic component of the electron-proton scattering as [78, 91]

$$\mathcal{M}_{\text{EM}} = \frac{4\pi\alpha}{Q^2} j_{\gamma e}^\mu J_\mu^{\gamma p}, \tag{2.32}$$

where α is the find structure constant, Q is the four-momentum transfer, and $j_{\gamma e}^\mu$ and $J_\mu^{\gamma p}$ are the charge currents from the electron and proton exchanging γ. The proton charge current can be written as [79, 91]

$$J_p^\mu = \bar{\psi}_p \left[F_1^\gamma \left(Q^2\right) \gamma^\mu + F_2^\gamma \left(Q^2\right) \frac{i\sigma^{\mu\nu} q_v}{2m_p} \right] \psi_p, \tag{2.33}$$

where F_1 is the invariant Dirac form factor, F_2 is the invariant Pauli form factor, $\sigma^{\mu\nu}$ is the Minkowski transformation metric, and m_p is the mass of the proton. Note that both form factors are dependent on the momentum transfer Q^2. For the purposes of experiment, it can be useful to use Sachs form factors, which are linear combinations of the Dirac and Pauli form factors. The Sachs form factors are written as [79, 91]

$$G_{\mathrm{E}}^{N}\left(Q^2\right) \equiv F_1\left(Q^2\right) - \tau F_2\left(Q^2\right), \tag{2.34}$$

$$G_{\mathrm{M}}^{N}\left(Q^2\right) \equiv F_1\left(Q^2\right) + \tau F_2\left(Q^2\right), \tag{2.35}$$

where

$$\tau = \frac{Q^2}{2m_p}, \tag{2.36}$$

and N can be any nucleon. G_{E} is referred to as the electric form factor, and G_{M} is referred to as the magnetic form factor. In the limit $Q^2 \to 0$, G_E becomes the electric charge and G_M becomes the magnetic moment.

It is, similar to the electromagnetic case, possible to write the weak scattering matrix as [91]

$$\mathcal{M}_{\mathrm{weak}} = \left(\frac{G_F}{\sqrt{2}}\right) j_{Z_e}^{\mu} J_{\mu}^{Zp}, \tag{2.37}$$

where G_F, known as the Fermi coupling constant, is defined as

$$G_F \equiv \sqrt{2}\left(\frac{g'}{4\cos\theta_W}\right)^2, \tag{2.38}$$

j^{μ}_{Ze} and J^{Zp}_{μ} are the neutral weak currents coming from an electron and proton exchanging a Z^0. The proton current can be written as [79, 91]

$$J^{Zp}_{\mu} = \bar{\psi}_p \left[F_1^Z \left(Q^2\right) \gamma^{\mu} + F_2^Z \left(Q^2\right) \frac{i\sigma^{\mu\nu} q_{\nu}}{2m_p} + \gamma^{\mu}\gamma^5 G_A^Z \right] \psi_p, \tag{2.39}$$

where G_A^Q is the axial form factor.

Next, these can be rewritten such that they are made up of the form factors of the underlying quarks. Despite the fact that the proton is made up only of up and down constituent quarks, there is a sea of virtual quarks that also has a contribution, and thus all quarks must be considered [79]. The electromagnetic form factors for the proton can be written as a sum over all quarks as

$$G^{\gamma p}_{\mathrm{E,M}} = \sum_q Q^q G^q_{\mathrm{E,\ M}}, \tag{2.40}$$

where $\sum_q$ is a sum over quarks. Similarly, the weak form factors can be written as

$$G^{Zp}_{\mathrm{E,M}} = \sum_q g_V^q G^q_{\mathrm{E,M}}, \tag{2.41}$$

and finally, the weak axial form factor can be written as

$$G_A^{Zp} = \sum_q g_A^q G_A^q. \tag{2.42}$$

Ideally, this sum would take place over all 6 known quarks, but in reality, only the up, down and strange quarks have significant contributions [79]. This means, using the values from

table 2.1, the form factors can be written as

$$G_{\mathrm{E,M}}^{\gamma p} = \frac{2}{3} G_{\mathrm{E,M}}^{u} - \frac{1}{3}\left(G_{\mathrm{E,M}}^{d} + G_{\mathrm{E,M}}^{s}\right), \tag{2.43}$$

$$G_{\mathrm{E,M}}^{Zp} = \left(1 - \frac{8}{3}\sin^2\theta_W\right) G_{\mathrm{E,M}}^{u} - \left(1 - \frac{4}{3}\sin^2\theta_W\right)\left(G_{\mathrm{E,M}}^{d} + G_{\mathrm{E,M}}^{s}\right), \tag{2.44}$$

$$G_A^{Zp} = G_A^d - G_A^u - G_A^s. \tag{2.45}$$

The neutron form factors can be written as

$$G_{\mathrm{E,M}}^{\gamma n} = \frac{2}{3} G_{\mathrm{E,M}}^{d} - \frac{1}{3}\left(G_{\mathrm{E,M}}^{u} + G_{\mathrm{E,M}}^{s}\right), \tag{2.46}$$

$$G_{\mathrm{E,M}}^{Zn} = \left(1 - \frac{8}{3}\sin^2\theta_W\right) G_{\mathrm{E,M}}^{d} - \left(1 - \frac{4}{3}\sin^2\theta_W\right)\left(G_{\mathrm{E,M}}^{u} + G_{\mathrm{E,M}}^{s}\right), \tag{2.47}$$

$$G_A^{Zp} = G_A^d - G_A^u - G_A^s, \tag{2.48}$$

by exploiting the charge symmetry between the up (down) quarks in the proton and the down (up) quarks in the neutron [22].

The values of form factors have been studied extensively. Of most recent interest have been the contribution from the strange quark sea and the proton and neutron strange form factors. A series of experiments starting with SAMPLE [56, 90] and including HAPPEX [4, 7, 13, 14, 15], G0 [9, 18], and PVA4 PV-A4 [21, 69, 70] explored the strange form factor [17].

2.4.2 Elastic parity-violating asymmetry

In section 2.4.1, the electromagnetic and weak scattering matrices were derived. Using equation 2.32 and equation 2.37 the elastic e-p scattering cross section can be written as

$$\sigma_{ep} \propto |\mathcal{M}_{\text{EM}} + \mathcal{M}_{\text{weak}}|^2 = |\mathcal{M}_{\text{EM}}|^2 + |\mathcal{M}_{\text{weak}}|^2 + 2\Re(\mathcal{M}_{\text{EM}}\mathcal{M}_{\text{weak}}), \tag{2.49}$$

Due to the massive nature of the Z^0 boson, the electromagnetic matrix dominates σ_{ep} since the strength of the weak interaction is $\propto 1/(Q^2 - M_Z^2)$ versus the strength of the electromagnetic interaction which is $\propto 1/Q^2$ [29].

In order to access the weak portion of the scattering matrix, parity violation must be exploited. Because the electromagnetic component is parity conserving, and the weak component is parity-violating, it is possible to design an experiment where the electromagnetic component cancels out. If the cross section of left and right handed electrons are subtracted as

$$\sigma_L - \sigma_R \propto 2\Re(\mathcal{M}_{\text{EM}}\mathcal{M}_{\text{weak}}), \tag{2.50}$$

the electromagnetic portion flips sign under parity transformation and thus cancels. Experimentally, helicity ($\mathbf{h} = \mathbf{s}\cdot\mathbf{p}$, where $\mathbf{h}$ is the helicity, $\mathbf{s}$ is the spin and $\mathbf{p}$ is the three-momentum) is used to access chirality (or handedness), given by γ^5. In the limit where the mass of the target particle is much larger than the mass of the scattered particle, or $m_e \ll m_p$, chirality and helicity may be treated the same since $\mathbf{s} \cdot \mathbf{p} \to \gamma^5$. In this thesis, L and R are used to

refer to left and right handedness, and + and − are used to refer to positive and negative helicity.

It can be experimentally favorable to measure an asymmetry over a cross-section since many systematic errors cancel in the ratio. The parity-violating asymmetry can be written as

$$A_{ep}^{\mathrm{PV}} \equiv \frac{\sigma_+ - \sigma_-}{\sigma_+ + \sigma_-} \approx \frac{2\Re(\mathcal{M}_{\mathrm{EM}}\mathcal{M}_{\mathrm{weak}})}{|\mathcal{M}_{\mathrm{EM}}|^2 + \Re(\mathcal{M}_{\mathrm{EM}}\mathcal{M}_{\mathrm{weak}})}. \tag{2.51}$$

By assuming $2\Re(\mathcal{M}_{\mathrm{EM}}\mathcal{M}_{\mathrm{weak}}) \ll |\mathcal{M}_{\mathrm{EM}}|^2$, equation 2.51 can be rewritten as

$$A_{ep}^{\mathrm{PV}} \approx \frac{2\mathcal{M}_{\mathrm{EM}}^{*}\mathcal{M}_{\mathrm{weak}}}{|\mathcal{M}_{\mathrm{EM}}|^2}. \tag{2.52}$$

This allows an experiment to access the weak sector via interference between the weak and electromagnetic portion of the scattering matrix (the $2\Re(\mathcal{M}_{\mathrm{EM}}\mathcal{M}_{\mathrm{weak}})$ term in A_{ep}^{PV} is the interference term). By looking at the scale set by [25]

$$\frac{\mathcal{M}_{\mathrm{weak}}}{\mathcal{M}_{\mathrm{EM}}} \propto \frac{Q^2}{(M_{Z^0})^2}, \tag{2.53}$$

and using $Q^2 = 0.0249$ $(\mathrm{GeV}/c)^2$ (the nominal Q_{weak} momentum transfer), and $M_{Z^0} = 91.1$ GeV/c^2, it can be determined that the asymmetry will be $\mathcal{O}(100$ ppm) [29].

The parity-violating asymmetry can also be written in terms of the Sachs form factors, which can be experimentally favorable, as [25]

$$A_{ep}^{\mathrm{PV}} = \left(\frac{-G_F Q^2}{4\pi\alpha\sqrt{2}}\right)\left(\frac{\varepsilon G_E^\gamma G_E^Z + \tau G_M^\gamma G_M^Z + g_V^e \varepsilon' G_M^\gamma G_A^e}{\varepsilon (G_E^\gamma)^2 + \tau (G_M^\gamma)^2}\right), \tag{2.54}$$

where τ is defined in equation 2.36, and ε and ε' are kinematic variables defined as

$$\varepsilon \equiv \frac{1}{1 + 2(1+\tau)\tan^2\frac{\theta}{2}}, \tag{2.55}$$

$$\varepsilon' \equiv \sqrt{\tau(1+\tau)(1-\varepsilon^2)}, \tag{2.56}$$

where θ is the polar scattering angle of the electron in the lab frame.

2.4.3 Parity-violating asymmetry and the proton weak charge

Now, the parity-violating asymmetry will be related to the weak charge of the proton. This is the theoretical basis for the Q_{weak} experiment. Using the vector and axial coupling constants from the Sachs form factors expressions given in equation 2.40 through equation 2.42, the weak Lagrangian can be written as

$$\mathcal{L}_{\mathrm{weak}}^{\mathrm{PV}} = -\frac{G_F}{\sqrt{2}}\left[g_A^e \bar{\psi}_e \gamma^\mu \gamma^5 \psi_e \sum_q g_V^q \bar{\psi}_q \gamma_\mu \psi_q + g_V^e \bar{\psi}_e \gamma^\mu \psi_e \sum_q g_A^q \bar{\psi}_q \gamma_\mu \gamma^5 \psi_q\right]. \tag{2.57}$$

Commonly, the axial and vector couplings for electron-quark interactions are written as [48]

$$C_{1q} \equiv \frac{1}{2} g_A^e g_V^q, \tag{2.58}$$

$$C_{2q} \equiv \frac{1}{2} g_V^e g_A^q. \tag{2.59}$$

Due to the coincidental value of $\sin^2\theta_W \approx 1/4$, C_{2q} is highly suppressed in the Standard

Table 2.2: Electromagnetic and weak charges of quarks at tree level.

	Q_{EM}	Q_W
u	$\frac{2}{3}$	$-2C_{1u} = 1 - \frac{8}{3}\sin^2\theta_W$
d	$-\frac{1}{3}$	$-2C_{1d} = -1 - \frac{4}{3}\sin^2\theta_W$

Model. Table 2.2 lists the weak charges of the up and down quarks. By adding electromagnetic charges for the proton and neutron constituent quarks, it can be shown that the expected values are $Q_p = 1$ and $Q_n = 0$. The same can be done to derive the weak charges of the proton and neutron to be

$$Q_w^p = 1 - 4\sin^2\theta_W, \tag{2.60}$$

$$Q_w^n = 1. \tag{2.61}$$

The final step is to now related the weak charge of the proton to the parity violating asymmetry. Take equation 2.51 and combine with the known form factors defined earlier in the

section to give [78, 79]

$$A_{ep}^{\mathrm{PV}} = \left(\frac{-G_F Q^2}{4\pi\alpha\sqrt{2}}\right)\left[Q_w^p + \frac{Q_w^n(\varepsilon G_E^{\gamma p} G_E^{\gamma n} + \tau G_M^{\gamma p} G_M^{\gamma n}) - g_V^e \varepsilon' G_M^{\gamma p} G_A^e}{\varepsilon(G_E^{\gamma p})^2 + \tau(G_M^{\gamma p})^2}\right]. \tag{2.62}$$

This can be significantly simplified by taking the forward angle limit ($\theta \to 0$) and the low momentum transfer limit ($Q^2 \ll m_p$) to give [78]

$$A_{ep}^{\mathrm{PV}} = \left(\frac{-G_F Q^2}{4\pi\alpha\sqrt{2}}\right)\left(Q_w^p + Q^2 B(Q^2,\theta)\right), \tag{2.63}$$

where $B(Q^2,\theta)$ is a nuclear structure term. In practice, it can be determined by fitting world PVES data. To isolate Q_w^p, define

$$A_0 \equiv \left(\frac{-G_F Q^2}{4\pi\alpha\sqrt{2}}\right), \tag{2.64}$$

and rewrite equation 2.63 to be

$$\frac{A_{ep}^{PV}}{A_0} = Q_w^p + Q^2 B(Q^2,\theta). \tag{2.65}$$

This is the most useful form for extracting Q_w^p from data.

Chapter 3

The $Q_{\mathbf{weak}}$ apparatus

The Q_{weak} experiment ran in experimental Hall C at the Thomas Jefferson National Accelerator Facility (Jefferson Lab) in Newport News, Virginia [68]. The experiment ran from fall 2010 through spring 2012. Due to a planned downtime to overhaul the Continuous Electron Beam Accelerator Facility (CEBAF), the experiment was split into two running periods, dubbed run 1 and run 2 in this thesis. There was also a commissioning period in the fall of 2010. Run 1 took place between January 2011 and May 2011. Run 2 took place between November 2011 and May 2012.

The Q_{weak} experiment was designed specifically to measure the parity-violating asymmetry from scattering polarized electrons off unpolarized protons at low momentum transfer and at forward angles. As stated in section 2.4.2, which set the scale of the parity-violating asymmetry, the measured asymmetry will be small. In fact, the Standard Model predicted

value is ~ -230 ppb. In order to precisely probe the Standard Model and new physics, Q_{weak} had a statistical error of ~ 7.3 ppb.

In order to achieve this low statistical error, a custom apparatus had to be constructed in Hall C, shown in 3.1. The apparatus was designed primarily to take data in integration mode, where, instead of detecting each electron, the signal is integrated over time. This allows for very high data rates. Q_{weak} used 8 radially symmetric Čerenkov detectors constructed from radiation hard quartz. In integration mode, these detectors saw a combined data rate of ~ 7 GHz [8]. The light from these detectors was detected via photomultiplier tubes (PMTs). This allowed precision measurement of the parity-violating asymmetry, and thus access to Q_w^p, in a reasonable amount of time.

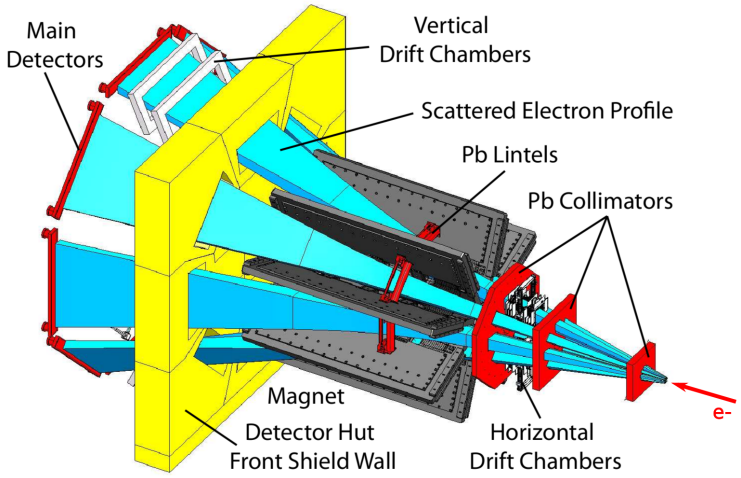

Figure 3.1: The Q_{weak} apparatus with lead collimators, horizontal drift chambers, lead lintels, spectrometer magnet, shield wall, vertical drift chambers and quartz main detector bar. Also shown is the scattered elastic electron path in blue.

Additionally, to accurately determine the momentum transfer Q^2, the apparatus could be switched to a low current mode, referred to in this thesis as event mode (since each event

was individually counted). In this mode, PMT bases were changed out, and removable wire drift chambers were moved into the scattered electron path. In this configuration, data rates were only about 100 kHz at most (data was taken at a variety of beam currents depending on the study). The effect of the additional material in the scattered electron's path was taken account of in simulation when the final Q^2 was determined.

3.1 Beamline

3.1.1 Polarized source

CEBAF is the primary accelerator at Jefferson Lab. Q_{weak} took beam from CEBAF in the so-called 6 GeV configuration; it has since been upgraded to provide up to 12 GeV beam energies. The basic layout of the accelerator and experimental halls can be seen in figure 3.2. CEBAF was ideal for the Q_{weak} experiment as it can provide high current and high polarization simultaneously [68].

The CEBAF polarized source uses three lasers (one for each of the halls, with Hall B and Hall D sharing a laser in the 12 GeV era) and a gallium arsenide superlattice crystal photocathode. The lasers are fired at 499 Hz, 1/3 of the accelerator operating frequency [89]. Using a technique called optical pumping and specialized doped crystals, high polarizations (up to $\sim$90%) [8] can be achieved. Optical pumping occurs when laser light excites electrons in an

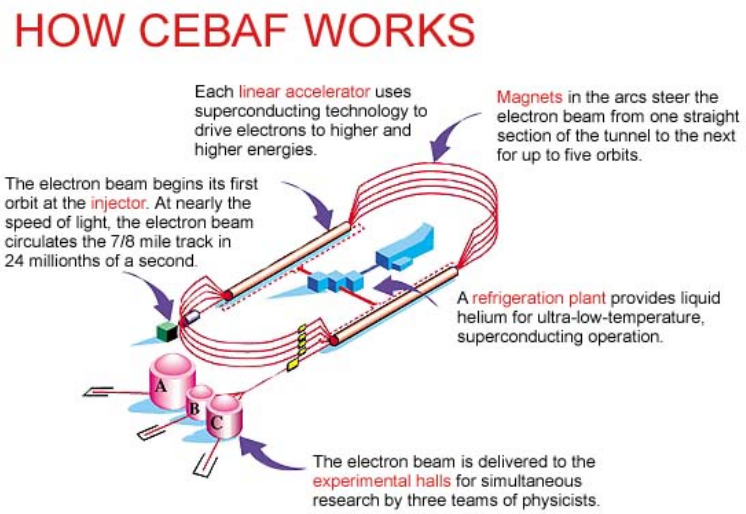

Figure 3.2: The Jefferson Lab Continuous Electron Beam Accelerator Facility. Image courtesy of Jefferson Lab [1].

atom to higher levels. If the light is circularly polarized, quantum mechanical selection rules require that the emitted electron be polarized [27]. The source can be seen in figure 3.3.

The polarized source has the ability to do rapid helicity reversal. This is done to prevent sensitivity to slow timescale changes in the accelerator. Fast helicity reversal was done by first passing the laser light though a Pockels cell, which acts like a quarter-wave plate when voltage is applied [8]. The polarization of the laser can be reversed by flipping the voltage on the Pockels cell, which in turn flips the helicity of the emitted electron. The helicity pattern is broken down into quartets which can be either (+ - - +) or (- + + -) [95]. Helicity correlated polarization was studied and determined to be a negligible effect for the Q_{weak} experiment. The quartet pattern is chosen pseudorandomly to reduce helicity-correlated noise. Each single helicity state in a quartet is referred to as macropulse (MPS). The helicity is reversed at 960 Hz.

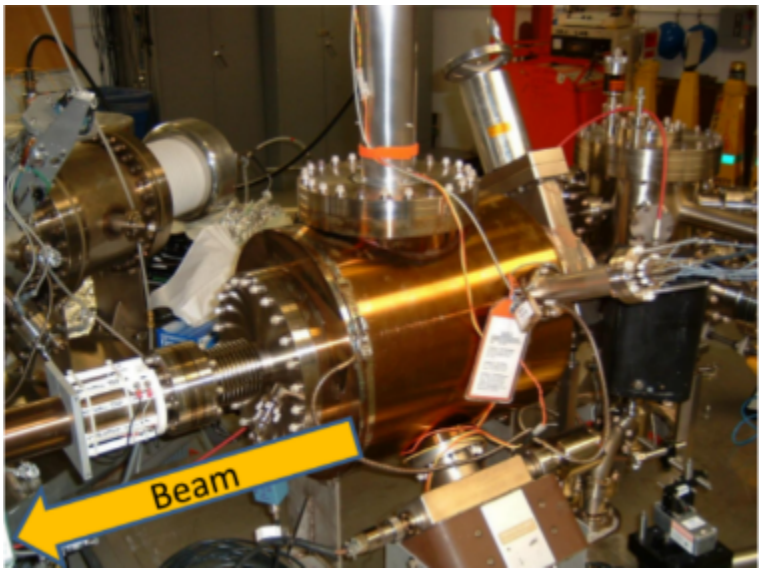

Figure 3.3: The CEBAF polarized source as configured during the running of Q_{weak}.

The Q_{weak} experiment also made use of a few slow helicity reversals, shown in the polarized source schematic in figure 3.4. These help to remove false asymmetries from backgrounds which do not flip with helicity. The first slow helicity reversal used was an insertable half-wave plate (IHWP) [8]. This allows the polarization of the laser to be flipped without changing the voltage in the Pockels cell. The IHWP was flipped every 8 hours and data taken within this 8 hour period is referred to as a slug.

A double Wien filter [5], shown in figure 3.4, was also used. The Wien filter was used in the source to ensure that the electrons arrived at the experimental hall with longitudinal polarization during ordinary running and to compensate for $g-2$ procession in the accelerator. It was also used periodically throughout the running of Q_{weak} to flip the polarization on the timescale of weeks. Data taken during a certain Wien filter setting is referred to as a wien. The Wien filter was also used to produce transverse polarizations used for measuring

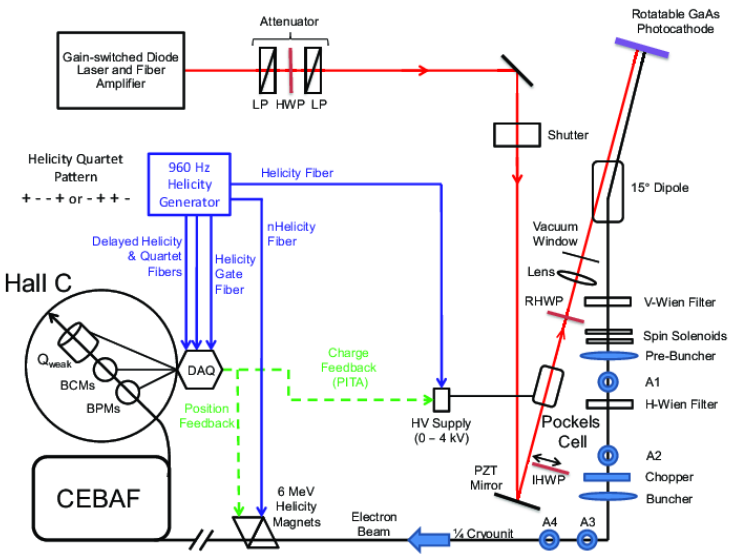

Figure 3.4: The Jefferson Lab polarized source optical table. Specifically of interest are the slow helicity reversal IHWP and the Wien filter.

transverse leakage as well as several ancillary data sets. This was used to make a correction for transverse leakage, see section 5.3.5.

3.1.2 Accelerator

Once the polarized electron is emitted from the photocathode, it is first accelerated to 45 MeV by superconducting radio frequency (SRF) cavity before being injected into the main accelerator. The source and initial linear accelerator are referred to as the injector. The CEBAF accelerator consists of a north and south linear accelerators (linacs), which also utilize SRF cavities to accelerate electrons. Each pass though a linac adds 600 MeV and one complete loop though the machine adds 1200 MeV [8].

The north and south linacs are connected via the east and west arcs, which are a string of magnets that allow the electrons to circulate though the machine up to 5 times. Each energy requires a different magnetic field to bend the electrons the proper amount, so different energy electrons are separated in the arcs, and then recombined for acceleration though the linacs.

Each experimental hall can receive a different number of passes and the linacs can be configured to give specific beam energies to meet experimental needs. Once the proper energy is achieved, individual beam buckets, or bunches of electrons destined for a specific experimental hall, enter the beam switchyard (BSY) and are separated and directed into the halls via a string of magnets.

3.1.3 Beam monitoring

Helicity-correlated beam motion can appear as a false asymmetry in the detector. Beam motion causes a false asymmetry by shifting the pattern of electrons on the main detector in one helicity state vs another, which will show up as a signal in the detector if they are not corrected. The false asymmetry can be quantified as [8]

$$A_{beam} = -\sum_i \frac{\partial A}{\partial \chi_i} \Delta_{\chi_i}, \tag{3.1}$$

where $\frac{\partial A}{\partial \chi_i}$ is the sensitivity of the asymmetry to some parameter χ_i and Δ_{χ_i} the difference of some parameter χ_i between helicity states. For example, for the X-axis position difference,

$$\Delta_X = X_+ - X_-. \tag{3.2}$$

Corrections are made for X and Y position differences as well as X' and Y' angle differences and energy.

In order to measure the differences and sensitivities, the Q_{weak} experiment used beam position monitors (BPMs) to measure position differences between helicity states. These values are read out and saved in the DAQ (see 3.9). Sensitivities ($\frac{\partial A}{\partial \chi_i}$) for beam position are calculated via correlations from data on the timescale of an hour, and a correction is calculated and applied for each quartet. This system was used as a systematic study and a verification for the beam modulation system (below) which was ultimately used to correct for helicity-correlated beam motion.

Over the running of the experiment, the beam energy was determined using a BPM at a position of highest dispersion in the accelerator, known as BPM3C12. BPM3C12 measured position and angle differences in X, and, by combining this information with standard beam position and angle data, it was possible to obtain the relative energy difference using BPM3C12 using [8]

$$\frac{\Delta P}{P} = \frac{\Delta X_{\text{3C12}}}{411} - \frac{\Delta X_{\text{target}}}{596} + \frac{\Delta X'_{\text{target}}}{0.443}, \tag{3.3}$$

where ΔX refers to the position difference measured by the BPM in the subscript. The relative energy measurement was used by beam modulation to correct for small energy fluctuations that naturally occurs in the accelerator. In addition, invasive measurements of the energy were made occasionally [8]. This was used to know the absolute incident beam energy. This was done by using the accelerator arc magnets as a spectrometer [101], and using 3 wire scanners, known as harps, to measure the beam positions.

Helicity-correlated charge asymmetry, i.e. change in the number of electrons in one helicity state versus another, can also cause a false asymmetry. Charge asymmetry is defined as

$$A_Q = \frac{Q_+ - Q_-}{Q_+ + Q_-}, \tag{3.4}$$

where $Q_\pm$ is the charge in a given helicity state. A charge feedback system was implemented to keep the charge asymmetry below ± 10 ppb [8]. Even with this small charge asymmetry, the signal was normalized by the charge as measured by a beam charge monitor (BCM) as

$$Y = \frac{S}{Q}, \tag{3.5}$$

where Y is the charge normalized yield, S is the integrated signal seen by the detector (see 3.6) and Q is the charge measured by the BCM. For more details see 5.3.1.

3.1.4 Beam modulation

In addition to using linear regression to correct for natural beam motion, a second method was also implemented. A series of coils would modulate the beam in X, X', Y, Y', and energy [58]. The changes induced were larger than natural beam motion. The sensitivity of the detectors ($\frac{\partial A}{\partial \chi_i}$) was then extracted using these modulations. For the final result, beam modulation was used to determine a correction for helicity-correlated beam motion [113]. See section 5.3.2 for details on the analysis.

3.2 Polarimetry

Since Jefferson Lab cannot produce a perfect, 100% polarized beam (as assumed by the derivation of Q_w^p in section 2.4.3), the polarization of the beam dilutes the true efficiency to the measured efficiency of

$$A_{msr}^{\text{PV}} = P_L A_{ep}^{\text{PV}}, \tag{3.6}$$

where A_{msr}^{PV} is the asymmetry as measured by the instrument, P_L is the longitudinal polarization, and A_{ep}^{PV} as the actual parity-violating asymmetry. Correcting for beam polarization is straightforward but requires accurately knowing the beam polarization.

To this end, Hall C implemented two polarimeters. The first was an existing Møller polarimeter, which scattered electrons off a highly polarized iron foil to determine the polarization of the beam to $\leq 1.5\%$. This measurement required a low beam current (between $\sim 2-20$ µA)

and was invasive, meaning Q_{weak} data could not be taken while obtain the polarization. Because the polarization changed over time (the quantum efficiency of the photocathode would slowly drop over about a week and then the laser spot would be moved), and because making invasive measurements often would greatly reduce statistics, a Compton polarimeter was constructed in Hall C. The Compton polarimeter was able to routinely achieve a statistical precision of $< 1\%$ per hour. For much of run 1, only Møller polarimetry data was available.

3.2.1 Møller polarimeter

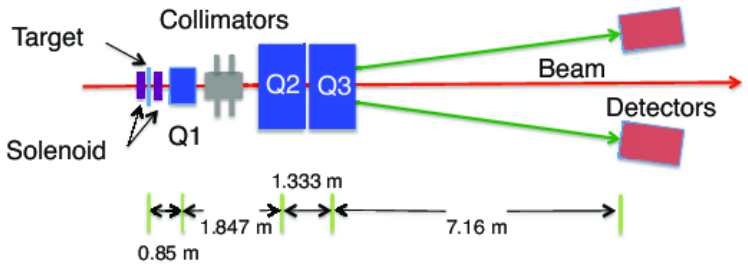

Figure 3.5: Schematic of the Møller polarimeter [8].

The Møller polarimeter [54], schematic shown in figure 3.5, measured the parity-conserving $\vec{e}\vec{e}$ asymmetry to determine the polarization. A thin iron foil was polarized using a 3.5 T superconducting solenoid (although the point at which the iron foil was fully saturated was 2.2 T) [8]. Scattered electrons as well as atomic recoil electrons were detected using lead glass calorimeters in coincidence. Movable collimators were used to help reduce the background of electrons which scattered off the nucleus (Mott scattering). Two quadrupole magnets focused the Møller scattered electrons onto the calorimeters.

Since Q_{weak} could not take data during a Møller polarimeter measurement, this was only done a few times per week. The Møller polarimeter could only be run at low beam currents, a systematic error was included for differences in polarization between beam currents.

3.2.2 Compton polarimeter

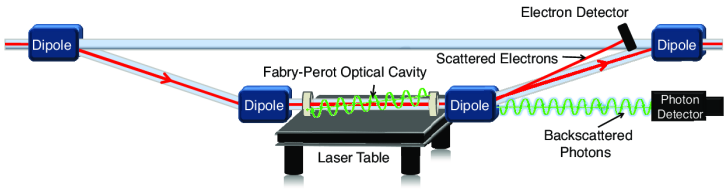

Figure 3.6: Schematic of the Compton polarimeter [8].

The Compton polarimeter [80], schematic shown in figure 3.6, uses $\vec{\gamma}\vec{e} \rightarrow \gamma e$ scattering to determine the polarization of the electron. The beam is deflected down and back up via four dipole magnets (referred to as the chicane). Here, the electrons would enter a Fabry-Perot optical cavity pumped with a 10 W 542 nm (green) laser [8]. Recoil electrons and photons were both detected in separate detectors.

The backscattered photons travel though the dipole magnet and into a lead tungstate ($PbWO_4$) crystal calorimeter, as shown in figure 3.6. A single PMT was attached to the back of the calorimeter. This was referred to as the photon detector. Because of a challenge in measuring and correcting for the nonlinearity in the relation between the incident photon rate and output detector current, this detector was never used to produce absolute polarization measurements.

Recoil electrons from Compton scattering are momentum analyzed by the dipole magnet and are detected by a diamond micro-strip detector inside the original beamline as shown in figure 3.6 [8]. The detector could be moved out of the path of the beam if the chicane magnets were not in use. The measured asymmetries were compared with QED to obtain the beam polarization [80].

3.3 Target

The Q_{weak} target [8] was designed and constructed by the Jefferson Lab target group. It consisted of a primary liquid hydrogen (LH_2) target and a matrix of solid, secondary targets. The primary liquid hydrogen target was used for the main measurement, and the solid targets were used to calculate the target window asymmetry contribution and for a variety of ancillary measurements. A CAD drawing of the target can be seen in figure 3.7.

3.3.1 Liquid hydrogen target

The liquid hydrogen target was designed to fit the specifications of Q_{weak}. The target had to be able to receive large amounts of energy from beam at high currents (more than 2100 W at 180 µA [8]) while also maintaining very low noise from target density fluctuations, or target boiling (less than 50 ppm noise).

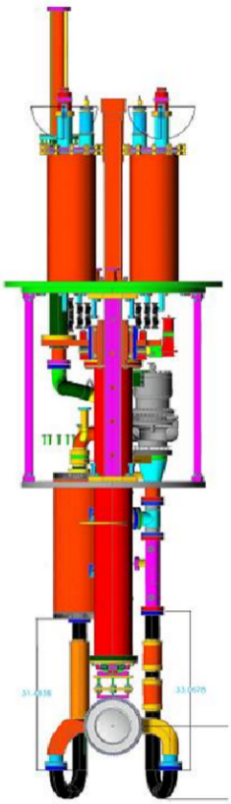

Figure 3.7: CAD drawing of the Q_{weak} target. Beam enters into the target window (grey disk at the bottom of the figure) and the cryogenic cooling loop is above.

The target used a 34.5 cm long scattering chamber made from aluminum and thin 7075-T6 aluminum entrance (0.10 mm) and exit (0.13 mm) windows [8]. LH_2 was circulated though a closed loop via a centrifugal pump. The horizontal flow of LH_2 was transverse to the direction of the beam. The closed loop consisted of a 3 kW resistive heater which would prevent the target from freezing when the beam was off and a counterflow heat exchanger which received both 5 K helium from the Central Helium Liquefier (CHL) and 14 K helium from the End Station Refrigerator (ESR). This was designed to keep the LH_2 at 20 K.

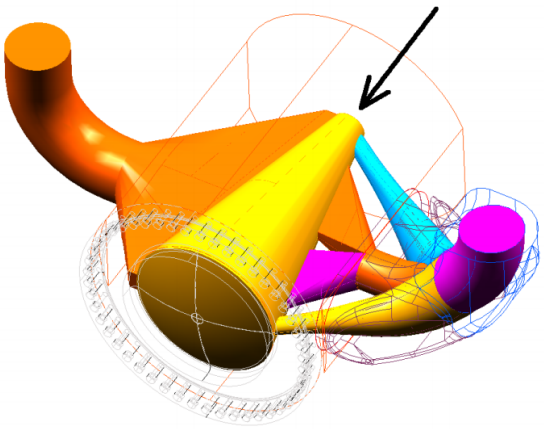

Figure 3.8: Computational fluid dynamics simulation of the Q_{weak} target scattering chamber. The beam direction is indicated by the arrow and the LH_2 flows in from the right and out though the left. Darker colors indicate cooler LH_2.

Providing a high power target with low localized density fluctuations (and thus low noise) was one of the technical challenges of Q_{weak}. This goal was achieved by using computational fluid dynamics (CFD) to determine the optimal geometry for minimal boiling. Figure 3.8 shows a detailed simulation of the scattering chamber temperature. The beam was also passed though a raster which usually had a 4 mm $\times$ 4 mm pattern [8]. This also helped to prevent target boiling as well as preventing the beam burning though the aluminium windows.

The noise contribution was extensively studied. Main detector (see section 3.6 for more details) asymmetry widths were plotted versus either beam current, rastered beam size, and rotational frequency of the LH_2 pump. All studies were consistent [8], and results for the study using LH_2 pump frequency can be see in figure 3.9. Under typical conditions, the target noise was $\sim$ 40 ppb, performing better than designed.

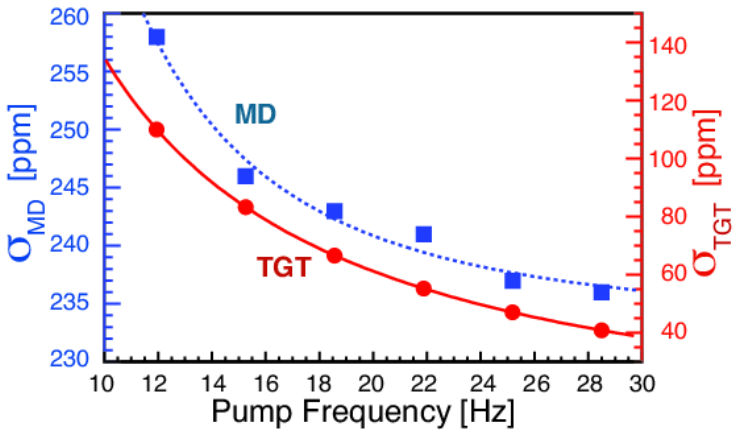

Figure 3.9: Target boiling noise study results, showing main detector asymmetry width σ_{MD} and implied noise contribution from the target σ_{TGT} vs pump frequency. The target pump operated at $\sim$ 29 Hz nominally. This data was taken with a 4 $\times$ 4 mm^2 raster size and 169 µA beam current.

3.3.2 Solid targets

The Q_{weak} target system also used a variety of solid targets. They were placed on an array below the primary LH_2 target, and were cooled via thermal conductivity with the LH_2 vessel. The solid targets were primarily used to determine the asymmetry from the aluminium window background as well as a number of ancillary studies. There were also centering targets which were useful for positioning the target using event mode detectors (see section 3.8). The array, with various targets, is shown in figure 3.10 in the run 2 configuration.

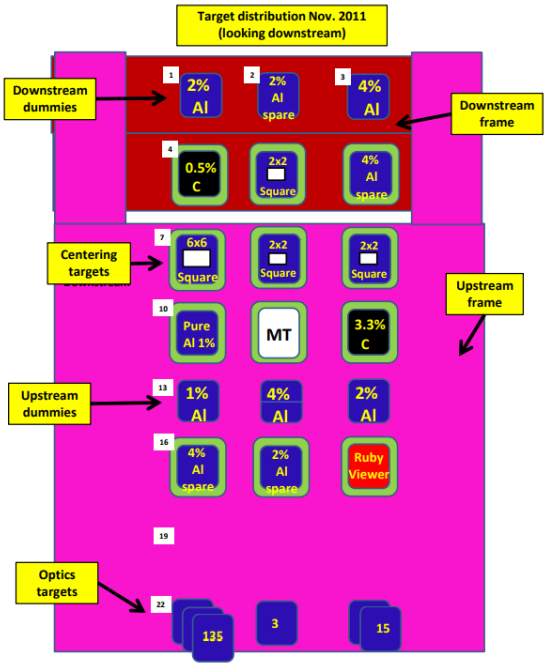

Figure 3.10: Schematic showing positions of various Q_{weak} solid targets. The upstream frame holds targets at the same z-position as the upstream target window, and the downstream frame at the same z-position as the downstream target window.

3.4 Collimation and shielding

The Q_{weak} apparatus used a variety of shielding systems to handle very large amounts of radiation produced by the accelerator and to reduce the signals in detectors from electrons that scatter along the beamline. This included collimators of various types and concrete shielding.

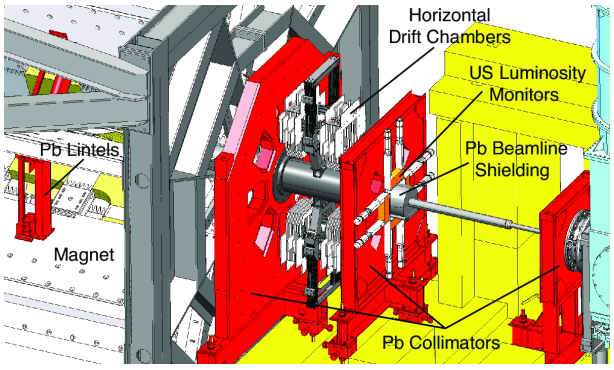

Figure 3.11: Schematic showing the three collimators. The far right collimator is the first collimator, the middle collimator is the second defining collimator, and the far left collimator is the third collimator. Beam goes from right to left. Also shown are the lintels (see section 3.4.3).

3.4.1 Triple collimator

Q_{weak} made use of three collimator made from a lead antimony alloy (95.5% Pb) [8]. These collimators had eight six-sided holes corresponding to the eight main detectors. The size of the holes varied according to how far downstream from the target they were.

The first and third collimator, placed 74 cm and 3.8 m downstream of the target respectively, were so-called clean up collimators. They help to reduce beamline backgrounds, i.e. electrons that interact with the beamline and end up in the detector. Section 5.3.3 has details on the beamline background and correction.

The second collimator, or defining collimator was at 2.7 m downstream of the target. This is the most important collimator as the downstream face determined the angular acceptance of the experiment, defining the angular acceptance to be $\theta \approx 5.8^\circ - 11.6^\circ$ [8]. The actual acceptance depends upon where in the target the scattering occurs. Each hole is about 400 cm^2 [79].

3.4.2 Beam collimator

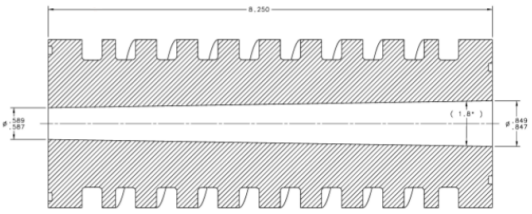

(a) Drawing of tungsten beam collimator.

(b) Photograph of the tungsten beam collimator after installation into the first collimator.

Figure 3.12: The water cooled tungsten beam collimator.

Simulations showed [76, 79] that the best way to reduce beamline backgrounds was to place a water cooled solid tungsten beam collimator around the beam pipe in the first collimator. A schematic of the beam collimator is shown in figure 3.12a and picture after installation can be see in figure 3.12b. Measurements of water flow and temperature showed that ~ 1.6 kW [8] of energy were deposited into the collimator.

The beam collimator functioned very well, and was able to dissipate heat effectively. However, it was determined late in run 2 that it did still contribute some signal into the main detectors and a large signal into the upstream luminosity monitors (which were totally unshielded from the beamline collimator). A systematic study was done to help understand this effect, and it was also studied using simulation. See section 5.3.3 for details.

In addition to the tungsten beam collimator, lead shielding was clamped to the beamline just upstream of the defining collimator. This was done after some shielding trials showed

that steel beamline components produced unexpected backgrounds. This can also be seen in figure 3.11.

3.4.3 Lintels

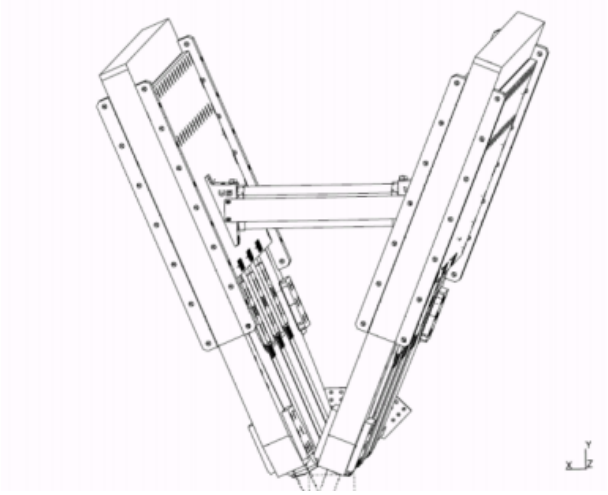

Figure 3.13: Drawing of the horizontal lead lintels installed between coils of the spectrometer magnet.

Eight lead lintels were installed between the coils of the Q_{weak} spectrometer magnet [79]. These were designed to stop neutral particles generated at the inner edges of the defining collimator holes. They were located 70 cm upstream of the magnets center [8]. Their placement can be seen in figure 3.11 and a schematic is show in figure 3.13.

3.4.4 Concrete shielding

Concrete shielding was used in several key areas. The very high radiation area just downstream of the target, between the first and second collimators, was completely enclosed in a

concrete hut. This helped to reduce backgrounds as well as protect workers who needed to access the apparatus.

A barite loaded ($Ba_2\,SO_4$) [8] concrete shielding wall was built just upstream of the main detector. Eight holes with several centimeters of clearance allowed scattered electrons to reach the main detectors. Like the beam collimator, this wall was built after several simulations [79] indicated line of site between sources of background and the main detectors.

3.5 Spectrometer

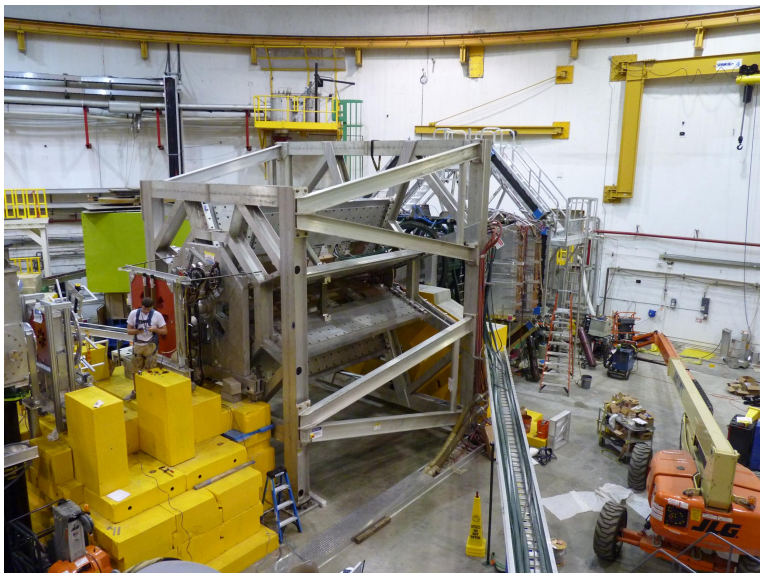

Figure 3.14: The Q_{weak} apparatus during installation. The Q_{weak} toroidal magnet can be seen in the gray aluminum support structure in the middle and the main detector bars it focuses on can be seen behind in the center-right of the photo.

The Q_{weak} toroidal magnet (QTor) focused elastically scattered electrons onto the eight main detector bars while at the same time sweeping away lower energy electrons from Møller

scattering (electron-electron scattering) [96]. QTor is shown in the installation photo in figure 3.14. The magnet was designed to run on a 10 kA at 130 V power supply and provide a integrated field $\int \mathbf{B} \cdot d\mathbf{l} = 0.67$ T $\cdot$ m along the trajectory of the electron [8].

The QTor magnet was built using eight separate copper coils made from very pure, low iron content copper. Any iron inside the magnetic field would become polarized and would pollute the asymmetry if electrons were to scatter off of it. These coils were water cooled with pure low conductivity water.

The magnetic field from the QTor magnet focuses the elastically scattered electrons onto a 2 m by 10 cm image [65]. This matched the design specifications of the main detector bars. The image on the bar has a unique moustache shape (see section 3.8.4), which is caused by fringe magnetic fields [83].

3.6 Main detectors

The eight Q_{weak} main detectors bars are quartz Čerenkov detectors and use quartz light guides and photomultiplier tubes (PMTs) to detect Čerenkov light. They needed to be constructed to be low noise, have a linear response to signal, and be radiation hardened. The eight main detector bars were made up of two 1 m Spectrosil© 2000 fused quartz bars which were glued together using UV transparent optical adhesive (SES-406) [8]. Spectrosil© 2000 was chosen because it is non-scintillating, low-luminescent, and radiation hard up to 1 MRad (around what simulation showed Q_{weak} detectors would be subject to). Each bar was

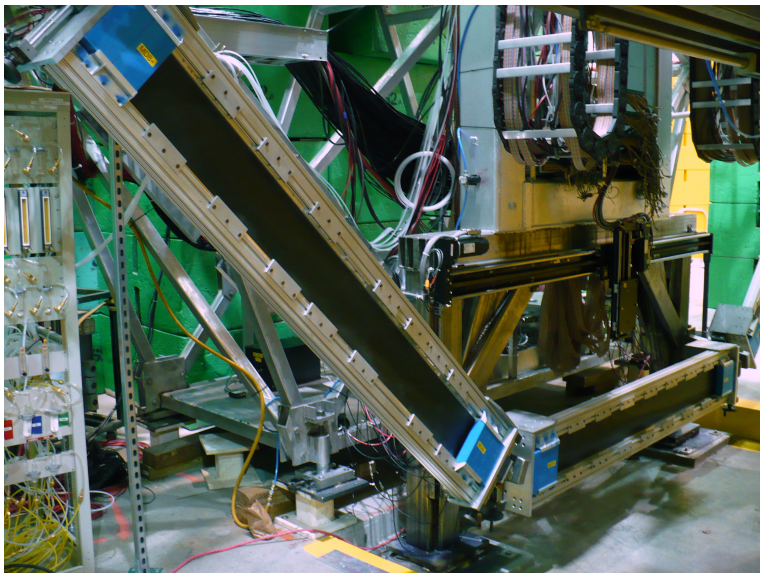

Figure 3.15: Photo of the Q_{weak} main detector bars without lead preradiators installed. Shown here are the upstream faces of MD7 (bottom) and MD8 (left side). The focal plane scanner can be seen behind MD7.

1.25 cm thick and 18 cm wide. Quartz light guides where then glued to both edges of the main detector bars, and PMTs were then glued to the ends of the light guides. The light guides allows the sensitive PMT's to be further away from the path of scattered electrons. Q_{weak} used Electron Tubes 9312WKB PMTs with a multi-alkali S20 photocathode and UV window.

2 cm thick lead preradiators where installed in front of the main detector bars [8]. This was done to boost the signal in the detector of the elastically scattered electrons, and to reduce (by acting as a filter) lower energy backgrounds. The trade-off with using a preradiator is a slight increase in noise by increasing the number of electrons per event. The signal-to-background ratio was improved by a factor of 20, but increased noise 10% [8]. The

preradiators also ended up causing an unexpected asymmetry due to transverse polarized electrons interacting in the lead. See section 5.3.6 for details.

The main detector bars, light guides and PMTs were mounted in a custom aluminum frame. These can be see in figure 3.15. These frames were in turn mounted onto a large structure referred to as the Ferris wheel, as it resembled the carnival ride. Part of this structure can be seen in figure 3.14. All parts of the support structure were designed to have low-iron content. The PMTs were magnetically shielded using mu-metal cases [8].

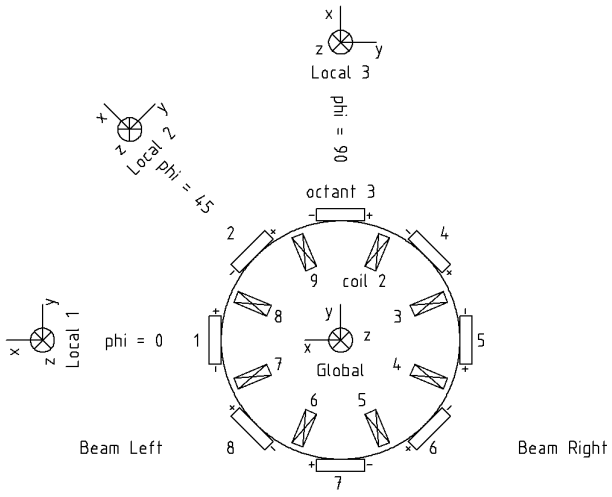

Figure 3.16: Schematic of the Q_{weak} azimuthal symmetry. Main detector bars are labeled 1 though 8 and the QTor coils are labeled 2-9. In this figure the beam goes into the page. + and − is the naming scheme of the individual PMTs.

The detectors were placed with azimuthal symmetry shown in figure 3.16. This figure shows the relationship between the QTor spectrometer magnet and the main detector bars. The main detectors were numbered MD1 through MD8 clockwise starting with the beam left

main detector. The individual PMTs were named e.g. MD1 negative and MD1 positive clockwise.

When a relativistic ($E_e > m_e$) electron enters the quartz bar, it produces Čerenkov light. Total internal reflection inside the bar causes the light to make its way to the light guide after a few bounces and eventually make its way to the PMT where the photons are converted into an electric signal.

Two sets of custom PMT bases were fabricated for Q_{weak}. They provided high voltage power to the PMTs as well as output for the signal. During high current integration mode running, the primary bases with a low-gain bases (~ 440) were used [8, 83]. These bases reduced the nonlinearity of the PMTs. When in event mode, high gain bases (2×10^6) were installed.

3.7 Background detectors

Despite strong efforts in engineering the Q_{weak} shielding, completely removing backgrounds is impossible. Thus, several background detectors were implemented in the design of Q_{weak}.

The first set of background detectors were constructed from two unused main detector PMTs which were placed in dark boxes [8]. The first one, referred to as the PMT only background detector (PMTONL) was placed as is into the beamline with an integration mode base [77]. The second detector was the same as the first, except a light guide, the same as was used in the main detectors, was glued to the PMT; this was referred to as the PMT light guide

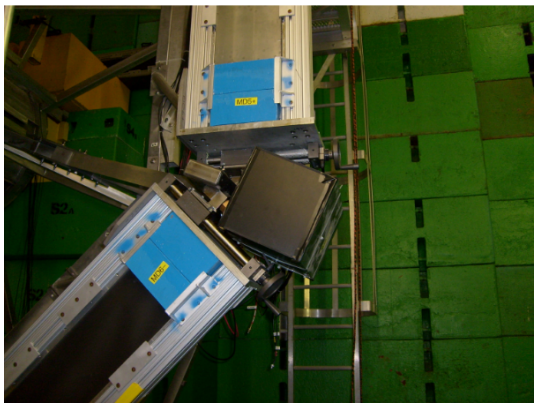

(a) PMTLTG in its original position between MD 5 and MD 6. PMTONL was on the same position on the opposite side. Beam goes into the page.

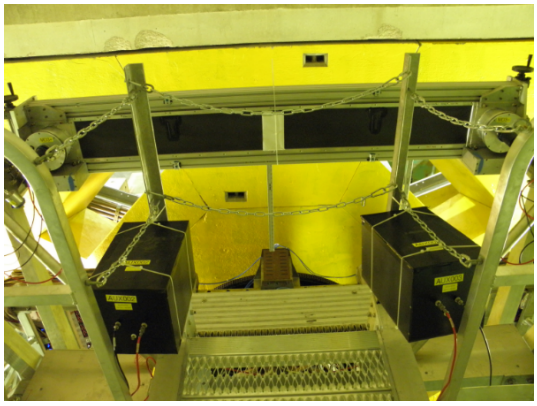

(b) PMTONL (left) and PMTLTG (right) in their final configuraiton behind MD 3, which can also be seen at the top of the picture. Beam comes out of the page in this picture.

Figure 3.17: PMT and light guide (PMTLTG) and PMT only (PMTONL) background detectors in both configurations used in Q_{weak}.

(PMTLTG) background detector. They can be seen in figure 3.17. Finally, a 9th main detector bar, MD 9, was constructed to serve as a background detector.

The positions of these background detectors was not consistent throughout run 1, however the positions in run 2 remained constant. During commissioning and the beginning of run 1, PMTONL was located between MD 5 and MD6 and PMTLTG was located between MD8 and MD1, as shown in figure 3.17a [77]. Then they were moved downstream of MD 3, as shown in figure 3.17b. During run 1, MD 9 was placed on top of the beamline shielding downstream of the main detector Ferris wheel; in run 2, out from MD 5 radially, and slightly downstream of the focal plane.

Halo monitors were also installed between 1 m and 5 m downstream of the target [8]. While not strictly background monitors, beam halo can scatter off beamline elements and generate

background. The Q_{weak} halo monitors used lucite or scintillator blocks fused to Photonis XP2262B PMTs. Additionally, an aluminum halo target, consisting of a frame with both a circular and a round hole cut in it, could be inserted 6 m upstream of the LH_2 target. This could be positioned such that the beam went though the round hole, square hole, or into the frame.

Two sets of luminosity monitors were also included on the Q_{weak} apparatus [8, 65]. Initially designed to serves as a null asymmetry check, monitor target boiling, and measure beam position and current for very low current running, they proved to be very useful for measuring background, as they were consistently placed throughout the entire running period and were placed close to a major source of background. Please see chapter 4 for details on the luminosity monitors.

3.8 Event mode tracking system

The Q_{weak} event mode system was made up of two detectors; a set of horizontal wire drift chambers (HDCs) between the second and third collimator (they can be seen in figure 3.11) just upstream of the QTor magnet, and a set of vertical wire drift chambers (VDCs) downstream of QTor just in front of the focal plane main detectors [8]. The purpose of the tracking system was primarily to measure the four-momentum transfer squared Q^2 but the system was also used for a variety of systematic studies.

As shown in equation 2.63, accurately knowing the momentum transfer is important for relating the asymmetry to the weak charge of the proton. Based on the geometry of the Q_{weak} apparatus, Q^2 could be determined to 1%. However, in order to make the systematic error budget, Q^2 needed to be known to 0.5%, and thus the tracking system was designed to meet this goal.

Q^2 can be related as

$$Q^2 = 2E^2 \frac{1 - \cos\theta}{1 + \frac{E}{m_p}(1 - \cos\theta)}, \tag{3.7}$$

where E is the incident beam energy and θ is the lab scattering angle. Through careful tracking of electrons, the scattering angle can be accurately determined. Combined with measurements of beam energy (see section 3.1.3), Q^2 can accurately be determined.

Q_{weak} used wire drift chambers to measured the scattering angle of electrons, as mentioned above. Wire drift chambers are a kind of detector with good position resolution which uses charged wires surrounded by a gas mixture. When a charged particle passes though, it leaves a trail of ionized gas along its path. These ions drift towards the wires and eventually strike, allowing a pulse to be recorded. The drift time allows you to determine the distance of closest approach of the charged particle from that wire [65]. By using multiple stacked drift chambers, it is possible to reconstruct the particle's track.

3.8.1 Horizontal drift chambers

Five HDCs were constructed by Virginia Tech (four plus a backup). They consisted of six wire planes with 32 sensing wires and 33 field wires [8]. The planes were in a $XUVX'U'V'$ orientation, where the U and V wires were placed at an angle of $\pm 43.1^\circ$ relative to the X wires. Due to this geometry, scattered electron tracks were at an angle of $\sim 7^\circ$ relative to the wires, so offset drift chambers were not necessary to resolve left-right directionality.

Wire planes were separated by Mylar foil cathode planes [8, 65]. During operation, a mix of 35% ethane 65% argon was used. The ethane helped to absorb X-rays produced in the chambers when an electron passed through. The cathode planes and field wires were held at -2150 V during operation.

The HDCs were placed on a custom rotator which held two HDC packages in the path of scattered electrons in one octant, and two packages in the opposite octant. The distance between the first and second packages was about 40 cm [8] in the direction of the beam. The rotator required manual rotation by a human operator, and could be locked in place in a variety of configurations.

Each chamber was tested using cosmic rays, which showed position resolutions of $150 - 200$ µm, and single plane efficiencies in excess of 99% [8]. Figure 3.18 shows tracks projected back to the defining collimator using Q_{weak} track reconstruction software. Events are shown to only come from within the collimator, and those that seem to come from the collimator

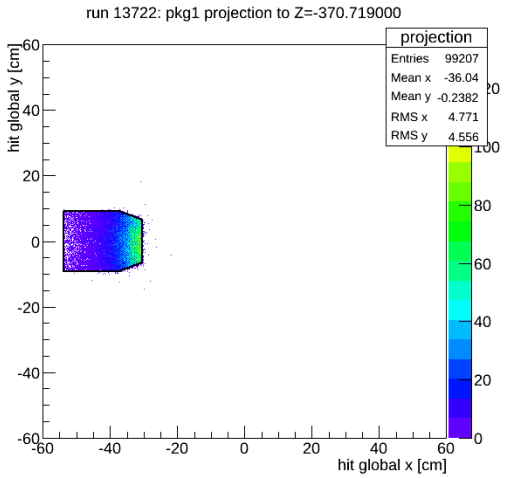

Figure 3.18: Profile of tracks which have been projected to the defining collimator, which is just upstream of the HDCs. Tracks which seem to not come from the hole in the collimator are likely the result of multiple scattering.

edges are likely the result of incorrectly reconstructed tracks due to multiple scattering of the electron.

3.8.2 Vertical drift chambers

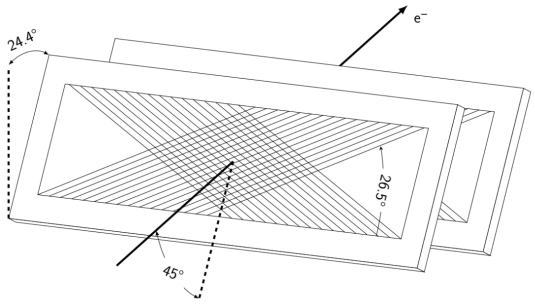

Figure 3.19: Schematic of the Q_{weak} VDCs. Also shown is the path of the scattered electrons (solid black line) and the axis of the VCD (dotted black line). Electrons enter at a 45° angle from the plane of the VDC.

The VDCs were built by The College of William & Mary. Five chambers were build (four in use plus a backup). These drift chambers were built with two wire planes UV orientation [8, 66]. The U and V wires are oriented at $\pm 26.5^{\circ}$ from the long axis of the chamber. A schematic of the VDC chamber can be seen in figure 3.19.

Each chamber consisted of 279 sensing wires and 2 anode wires which were held at ground [8]. High voltage cathode planes, made from Mylar foil, was held at -3800 V. The chambers were filled with a mix of 50% argon and 50% ethane gas.

The VDCs were mounted on a large, mechanical rotator system that mounted two VDCs in one octant, and two more in the opposite content. As with the HDCs, the two VDC chambers were mounted with the second chamber being 53 cm downstream of the first one [8]. The rotator was motorized, but had to be operated from inside the main detector enclosure. It could not be rotated remotely. Another difference from the HDCs is that the chambers were tilted with respect to the path of the incoming electrons such that they entered at 45°. This helped improve spatial resolution of the VDCs.

As with the HDCs, the VDCs were benchmarked with cosmic rays. The single wire efficiency was measured to be $> 98.8\%$, with a position reproducibility better than 3 mm azimuthally and 1 mm radially [8].

3.8.3 Trigger scintillators

Plastic scintillator paddles, made from Bicron BC-408 plastic, were used to provide a fast trigger signal during event mode data taking as well as help study neutral backgrounds [8, 79]. These paddles were installed just upstream of the VDC chambers (one on each side). They were attached to PMTs via a lucite light guide. They were also useful for measuring or rejecting neutral backgrounds. When the trigger scintillators do not see an event but the main detector bars do, a neutral event can be assumed.

3.8.4 Focal plane scanner

The focal plane scanner, often referred to just as the scanner, was build so that there could be some comparison of the image on the main detector bar at low current, event mode running and high current, integration mode running. To this end, the focal plane scanner was created [8]. Figure 3.20 shows a relative rate map of MD 7, which shows the expected mustache shape.

The scanner was made up of two 1 cm^3 overlapping pieces of quartz each forming a 1×1 cm^2 sensitive area. Each quartz cube was read out by its own PMT via an air core light guide. A coincidence between the two PMTs was required to help reduce accidental triggers and reject low energy backgrounds. The scanner could handle up to 1 MHz/cm^2 allowing operation during high current running. The whole apparatus was mounted on a 2D linear motion system that was programmed to scan over the entire main detector bar. The scanner

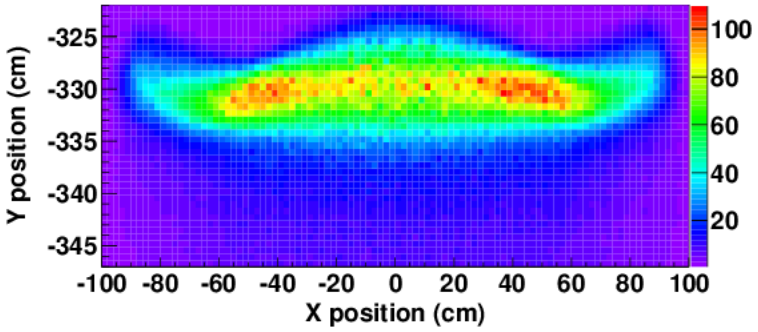

Figure 3.20: Relative rate map of flux on MD 7 created from focal plane scanner data. The expected mustache shape can be seen. The x-axis is in the horizontal direction, and the y-axis is in the vertical direction. The horizontal and vertical scales are chosen differently for ease of illustration.

could be placed upstream or downstream of MD 7, although in the upstream configuration, data taking was interrupted.

3.9 Data acquisition system

The Q_{weak} experiment implemented two data acquisition (DAQ) systems; one for integration mode and one for event mode. Each system used separate hardware due to the different needs of the integration and event mode detectors.

3.9.1 Integration mode DAQ

In integration mode, the PMTs output a current proportional to the number of photoelectrons in the tube. In order to digitize this, low-noise current-to-voltage preamplifiers were used [8]. These preamplifiers could be could be configured to have an impedance of between

0.5 MΩ and 50 MΩ. Radiation hardness testing was done up to 1 kRad and no degradation of performance was detected.

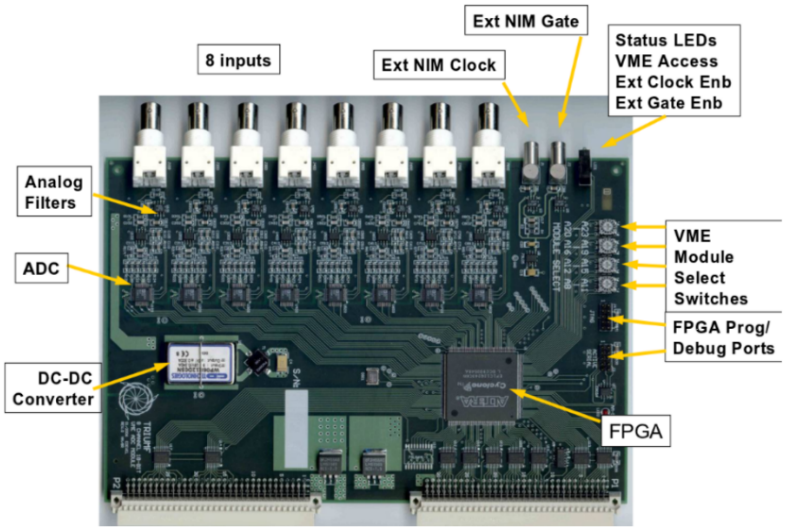

Figure 3.21: Photograph of the VQWK ADC board. These were used to digitize main detector, luminosity monitor, and beam monitor signals.

The integration mode DAQ used custom build sampling-integration analog-to-digital converters (ADCs) referred to as VQWK modules [8]. The VQWK models were custom designed application-specific integrated circuits (ASIC) that were built by TRIUMF, a Canadian national laboratory. The VQWK modules were designed to be low noise and record the integrated the voltage signals of the main detectors, background detectors, and beam monitors. The Q_{weak} DAQ software was written in CODA, a Jefferson Lab DAQ framework [23, 97].

The helicity reversal rate, as stated in section 3.1.1, was 960 Hz. Shown in figure 3.22 is the helicity gate window [8]. $T_{\text{stable}} = 972$ µs is the width of the window when the helicity is stable. $T_{\text{ADC delay}} = 43$ µs is a delay after the start of T_{stable} before the ADC begins

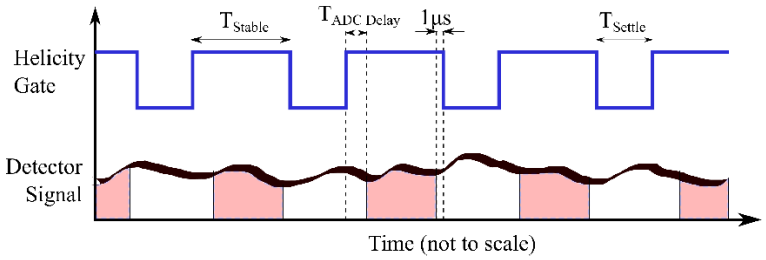

Figure 3.22: Timing diagram of the integration mode DAQ. The shaded area is the part of the signal that is read by the ADCs.

accumulating samples due to computer dead time. The last sample is taken ~ 1 μs before the helicity flips. $T_{\text{settle}} = 70$ μs is the time given for the Pockels cell and source to stabilize.

3.9.2 Event mode DAQ

In event mode, detector signals were collected using hardware based triggers instead of triggering on the helicity signal. Depending on the needs of the study, data taking could be triggered on a variety of sources including trigger scintillator panels, the main detector PMTs, the background detectors and others [8]. Actual data taking rate varied depending on the beam current and trigger source.

The vertical and horizontal drift chambers were read out using custom F1TDC modules build by Jefferson Lab. The F1TDCs are a type of time-to-digital converter (TDC), which, similar to a ADC, digitizes pulses in time. In some cases, multiple wires and detectors could be read out by the same F1TDC using a known time delay module and multiplexing.

Chapter 4

Luminosity monitors

4.1 Introduction

The luminosity monitors refers to two sets of ancillary detectors that were placed into areas where the scattered electron fluxes were much higher than the main detectors, and had a much smaller physics asymmetry. Two sets of detectors were installed. The first, referred to as the upstream luminosity monitors, was installed on the upstream face of the second collimator (see section 3.4.1 for details on the collimator system). The second, referred to as the downstream luminosity monitors, was installed on the downstream face of the rear of the main detector collimator hut (see section 3.4.4 for details on the shielding hut).

The luminosity monitors were built primarily as a null check; to verify that there were no uncorrected false asymmetries in the beam, measure target boiling noise, and to measure

beam current and position for extremely low current running where BCMs and BPMs (see section 3.1.3 for details on beam monitoring) no longer function reliably [8, 65]. The upstream luminosity monitors were very useful for measuring beamline background false asymmetries. The downstream luminosity monitors were also very sensitive to helicity-correlated beam properties and thus provided a crosscheck to regression (see section 3.1.3).

The upstream luminosity monitors accepted electrons scattered at $\sim 5^{\circ}$, which is predominantly Møller scattered electrons [8, 65]. Electrons that scatter at this angle are less sensitive to beam position and energy, so they were useful for measuring target boiling and beamline backgrounds. The downstream luminosity monitor accepted electrons scattered at $\sim 0.5^{\circ}$ and were made up of a mix of elastic $\vec{e}p$ and Møller scattered electrons. Since both sets of luminosity monitors saw a much larger signal than the main detectors, the expected statistical error bars were much smaller but the larger fluxes also required that the detectors be radiation hard.

4.2 Luminosity monitor design

4.2.1 Čerenkov detector hardware

The luminosity monitors were designed and built at Virginia Tech [65]. The design work was primarily done in GEANT3 [6], a high energy simulation framework. Both sets of luminosity

monitors were constructed from the same radiation hard Spectrosil© 2000 fused quartz as the main detector bars.

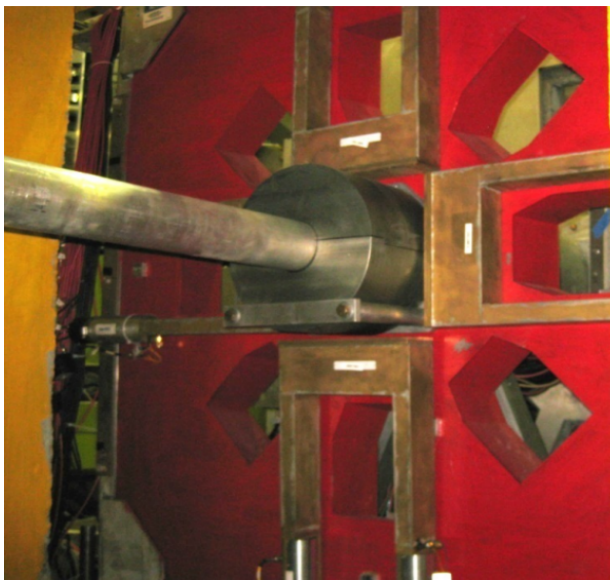

Figure 4.1: Q_{weak} upstream luminosity monitors installed on the second collimator. Beam goes from left to right.

The designs of the upstream and downstream luminosity monitors differed. Four upstream luminosity monitors were built and placed into octants 1, 3, 5 and 7 (see figure 3.16) as shown in figure 4.1. These detectors used a $7 \times 27 \times 2$ cm^3 quartz Čerenkov radiator with 2 cm 45° taper at the side to allow light to escape [8, 65]. CAD drawings can be seen in figure 4.2. Air-core light guides were made from highly reflective aluminum sheet metal (Alanod Miro-Silver 27) and attached to both of the notches on the quartz bars. The light guides were long to move the PMTs far away from the path of scattered electrons. The light guides were purged with N_2 gas to prevent damage of the reflective surface. Light was detected with Hamamatsu R375 PMTs with quartz windows and multi-alkali photocathode. The

multi-alkali photocathode helps to reduce sheet resistance and thus reduce space charge. Two light guides and PMTs were used for each quartz bar.

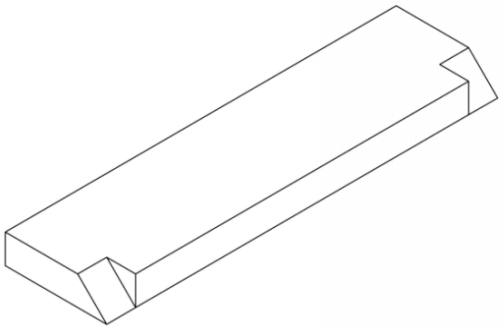

(a) Isometric view of the upstream luminosity monitor quartz bar.

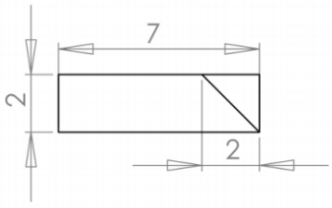

(b) Side view of the upstream luminosity monitor quartz bar.

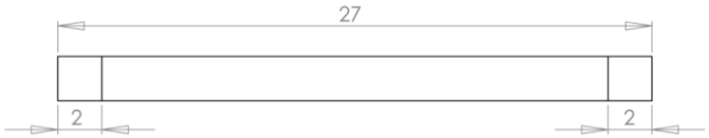

(c) Front view of the upstream luminosity monitor quartz bar.

Figure 4.2: CAD drawings of the upstream luminosity monitors with isometric, front and side views.

The downstream luminosity monitors used a different design. Eight downstream luminosity monitors were installed into all eight octants, downstream of the main detectors and main detector shield wall. These detectors used $4 \times 3 \times 1.3$ cm^3 quartz Čerenkov radiators with a single light guide and PMT [8, 65]. Since these detector bars are so small, the 45° taper, which allows light to escape the quartz bar, extends the entire edge of the detector. CAD drawings can be seen in figure 4.4. The light guides were made from the same high reflectivity aluminum sheet metal and Hamamatsu PMT as the upstream luminosity monitor. N_2 gas was also used in the downstream luminosity monitors to protect the light guides. Each

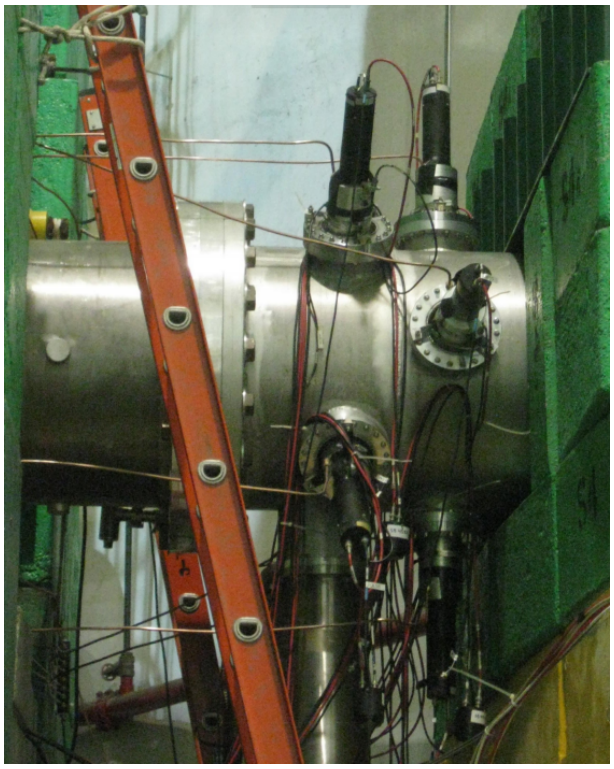

Figure 4.3: Q_{weak} downstream luminosity monitors installed on the beamline. Beam goes from left to right. Also shown are the permanent ladders used for maintenance access.

quartz piece was read out by a single PMT (unlike the upstream luminosity monitors which had two PMTs per quartz bar). 2 cm lead radiators were installed in front of the quartz bars as in the main detectors (see section 3.6). The preradiators were installed to suppress low energy backgrounds.

Both detectors saw larger fluxes than the main detectors. The upstream luminosity monitor saw a signal of $\sim$ 115 GHz and the downstream luminosity monitors saw a signal of $\sim$ 150 GHz [8]. This means they would be subject to up to 4 GRad of radiation throughout their lifetime [8, 65]. Even though Spectrosil© 2000 is generally considered radiation hard to 1 MRad, it has been used without issue up to 2 GRad. Visual inspection of the quartz after

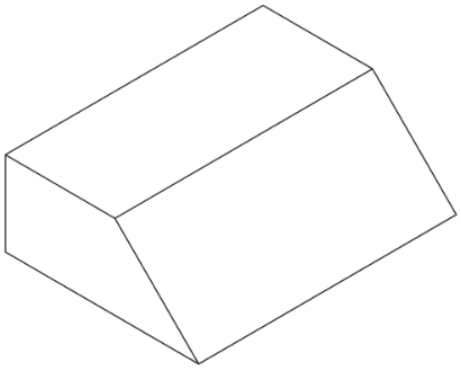

(a) Isometric view of the downstream luminosity monitor quartz bar.

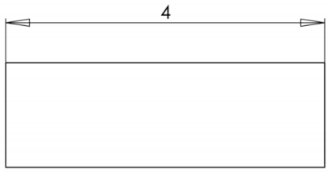

(b) Side view of the downstream luminosity monitor quartz bar.

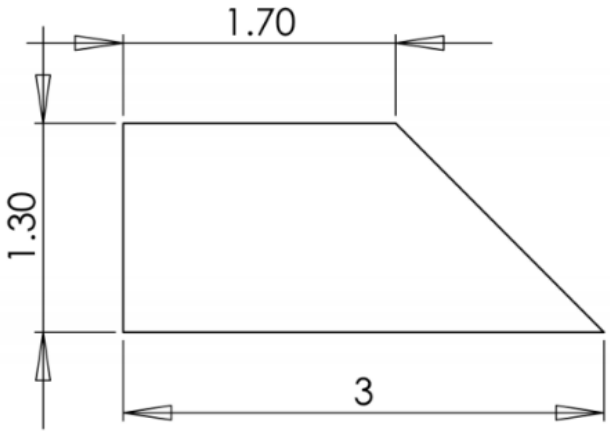

(c) Back view of the downstream luminosity monitor quartz bar.

Figure 4.4: CAD drawings of the downstream luminosity monitors with isometric, front and side views.

the end of the Q_{weak} experiment showed no visible signs of darkening. The light guides also looked visibly clear (see figure 4.8). Use of N_2 prevented residual dust particles in the air from settling onto the light guides and darkening with radiation dose. Some plastic parts were significantly radiation damaged after run 1 and were replaced with radiation hard Macor ceramic which showed no damage after the end of run 2. Efforts to harden the detectors to the extreme radiation environment proved effective.

4.2.2 Detector electronics chain

Because both the upstream and downstream luminosity monitors had to be used in high current, integration mode running as well as low current, event mode running, two sets of PMT bases were constructed (similar to the main detector bases, see section 3.6). Low gain PMT bases (unity gain) were used during high current integration mode running, and high gain PMT bases ($\sim 10^6$) were used during low current event mode running [8, 65]. Both the upstream and downstream luminosity monitors used the same type of PMT bases.

For high gain, a conventional voltage divider PMT base was used [65]. To achieve unity gain for the low gain bases, all the PMT dynodes were tied together, as shown in the unity gain base schematic in figure 4.5. A small current (~ 1 µA) is then read out on the last dynode. This current is proportional to the number of photons hitting the PMT photocathode.

The current signal from the unity gain PMT base goes into a current-to-voltage (I-to-V) preamplifier shown in figure 4.7. These were custom designed and built by TRIUMF [65].

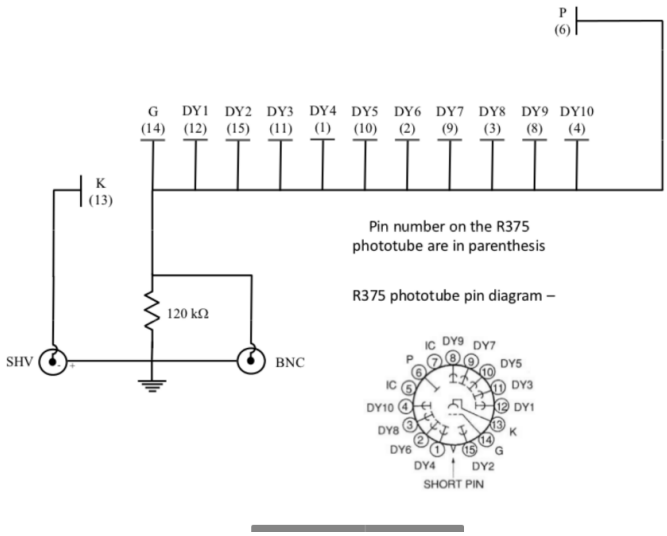

Figure 4.5: Schematic of luminosity monitor unity gain base used with R357 PMTs.

These were placed out of the direct path of scattered electrons and were heavily shielded with lead bricks [8]. The I-to-V preamplifiers could be set to several different gains and effectively acted as a resistor. The preamplifiers were similar in design to the main detector preamplifiers. For the upstream luminosity monitors, 25 MΩ preamplifier setting was used. For the downstream luminosity monitors, 4 MΩ was used. The voltage was then digitized using a VQWK ADC (see section 3.9.1 for details). The entire electronics chain can be seen in figure 4.6. The overall electronic noise of the system was measured by J. Leacock and found to be negligible compared to the counting statistics noise [65].

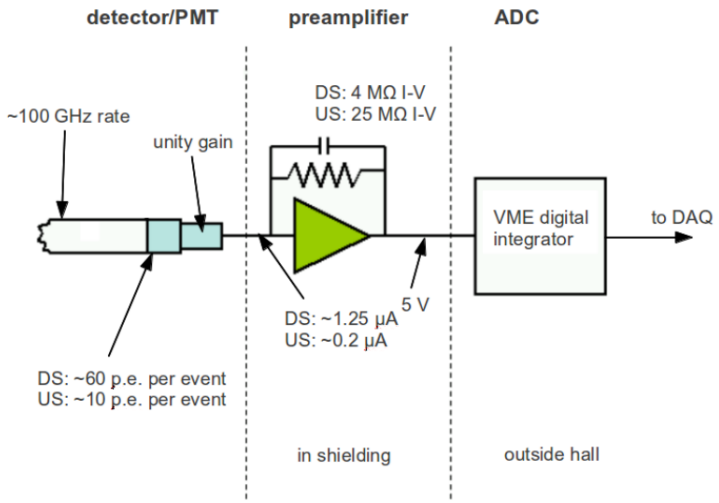

Figure 4.6: Schematic of luminosity monitor electronics chain. Differences between the upstream (US) and downstream (DS) electronics chain is noted.

4.3 Luminosity monitor characterization and performance

The luminosity monitors performed very well given the extreme radiation they were exposed to. Several failures did occur. Since the luminosity monitors were important to the beamline background analysis, care had to be given to how failures were handled.

4.3.1 Luminosity monitor performance and lifespan

During run 1, upstream luminosity monitor 7 had the negative PMT base presumably failed [43]. The exact cause was not determined, but overhaul of the PMT bases between run 1 and run 2 fixed the issue.

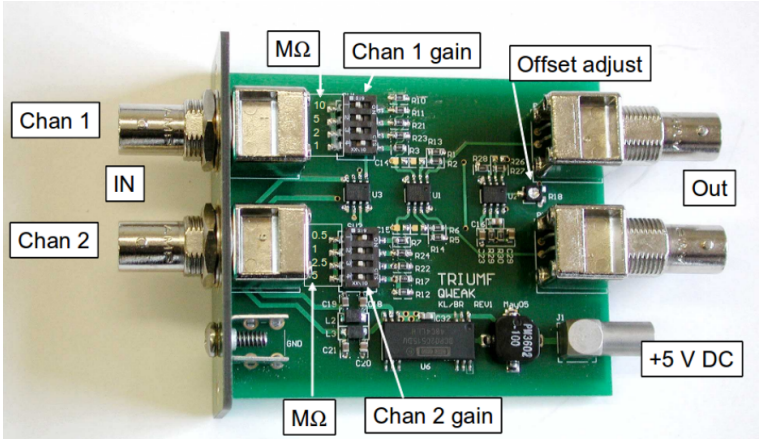

Figure 4.7: The luminosity monitor preamplifier board. One preamplifier could handle two PMT channels.

During run 2, the importance of the upstream luminosity monitors as a background detector was recognized (see section 5.3.3) and effort was put into keeping these detectors working, including emergency maintenance. Upstream luminosity monitor 1 and 5 both had single PMTs fail, and for a short time, both tubes of upstream luminosity monitor 5 failed [43]. These failures were all manifest by saturated ADC signals, and the problem seemed to be radiation damage causing insulation in the PMT bases to break down or cause intermittent shorts to occur. In order to keep at least one PMT alive on each bar, emergency maintenance was conducted to replace PMT bases. In the case of upstream luminosity monitor 5 negative, damage was suspected to be to the PMT itself, as replacing the base did not resolve the saturation.

It was observed that the pedestal values of the detectors, i.e. the signal in the detectors when no beam was present, was a good indicator of when a PMT base was nearing failure [38]. In

some cases, when an increase in drifting was observed, the PMT base would be preemptively replaced when access to the apparatus was granted.

After the running of Q_{weak}, checks were made to confirmed that no unnoticed bad periods existed. The first step taken was to look at the upstream and downstream luminosity monitor pedestals versus time [37]. As stated above, this was used as a metric to predict failure during the run. No obvious bad periods were found using this data.

Luminosity monitor health checks were also done by looking at the yield versus time. Very large yields as well as negative yields are non-physical and subsequent investigation revealed mistakes in mapfiles or luminosity monitor failure earlier than detected by the shift crew. These mistakes were corrected and included in subsequent data analysis.

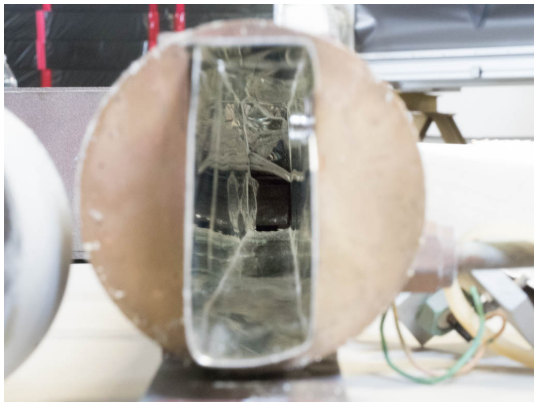

(a) Upstream luminosity monitor light guide after Q_{weak} run. Quartz at the bottom looks clear and light guide has only minimal oxidation.

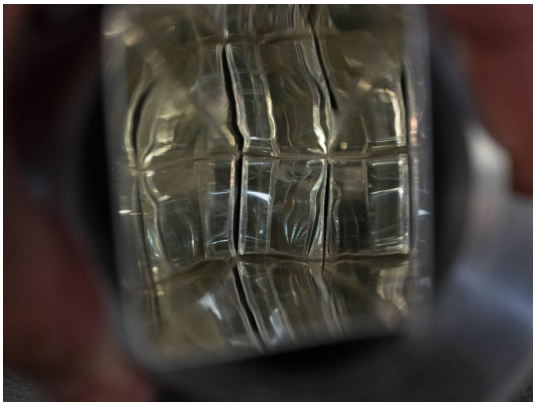

(b) Downstream luminosity monitor light guide after Q_{weak} run. Quartz at the bottom and light guide both look clear.

Figure 4.8: Photographs of upstream and downstream luminosity monitors after Q_{weak} run. Light guides and quartz shown.

When the luminosity monitors were taken apart during the dismantling of the Q_{weak} apparatus, their general condition was observed. Many of the upstream luminosity monitor bases

had extensive radiation damage, in some cases the plastic casing dissolved completely in the hand. Overall condition of the quartz bar was very good, with no visible darkening of the quartz and the light guides remained very reflective to the eye. Pictures of the light guides and quartz can be seen in figure 4.8.

4.3.2 Luminosity monitor as background detector

As previously mentioned, the upstream luminosity monitors signal ended up being dominated by background signals and thus acted more as background detectors than for their designed purpose as target boiling monitors. This proved fortuitous as they were the only consistent measurement of beamline background; as mentioned in section 3.7, all the other background monitors were moved to more ideal locations throughout the running of Q_{weak}. Additionally, a significant portion of the upstream luminosity monitor signal was from the beam collimator, which was thought to be the primary source of beamline background.

During data taking, the upstream luminosity monitor asymmetry width was a useful metric to ensure low background beam was being provided [44]. Asymmetry widths are a measure of the random noise in the system, including beam and detector noise. Certain changes in the beam tuning would create scraping (where electrons inadvertently hit elements inside the accelerator and scatter) and thus halo in the beam. This halo would then interact with the beamline collimator. A very small portion of this signal would make its way to the main detector bars, but a large portion would be seen by the luminosity monitors. This would

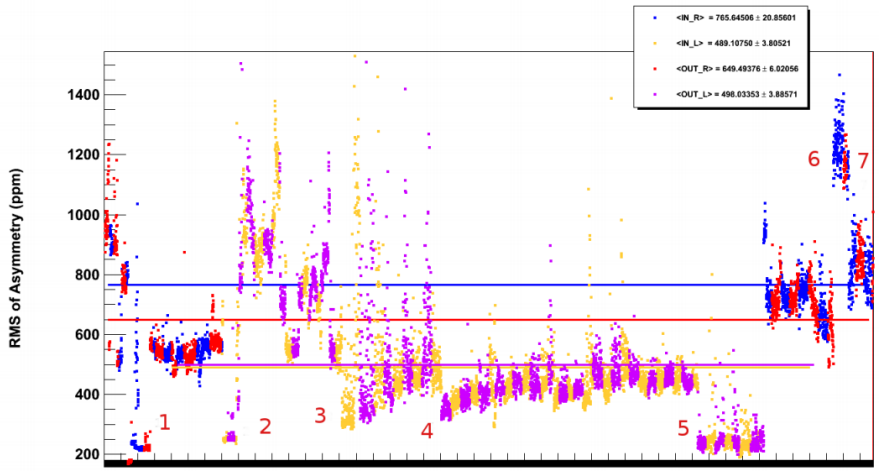

Figure 4.9: Plot of upstream luminosity monitors asymmetry width (ppm) vs time. All numbered jumps correspond with known injector and accelerator changes [44].

cause the asymmetry widths to jump dramatically, and give nearly real time feedback on beam conditions. Figure 4.9 shows the jumps observed in run 2; each number corresponds to a change in beam optics.

Since the luminosity monitors and main detectors both saw beamline background from the same sources, (although the main detectors saw significantly less signal from this source) a correlation could be found between the main detector and upstream luminosity monitor after removing effects from natural beam motion and charge [40, 44]. This was verified using tungsten shutters that blocked electrons scattered through octants 1 and 5 [42, 62]. For details on how this analysis was done, see section 5.3.3.

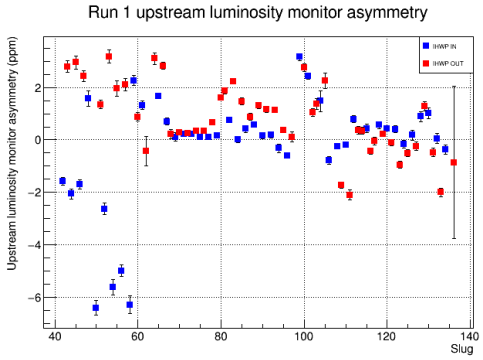

(a) Upstream luminosity monitor asymmetry versus slug for run 1.

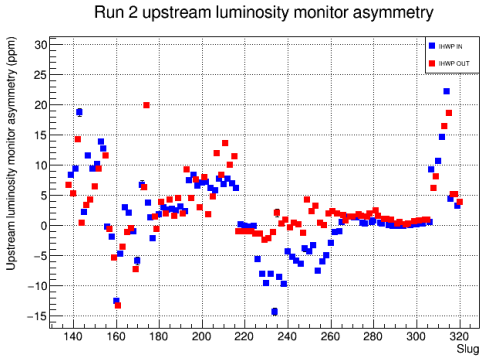

(b) Upstream luminosity monitor asymmetry versus slug for run 2.

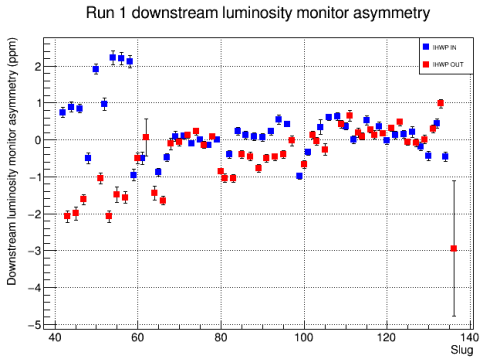

(c) Downstream luminosity monitor asymmetry versus slug for run 1.

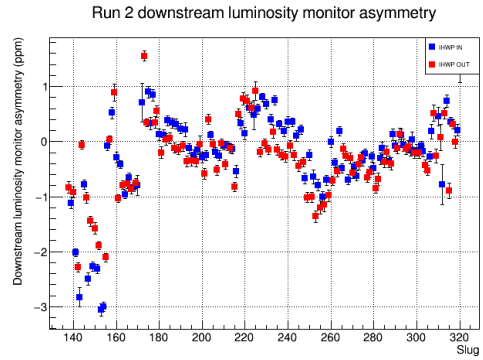

(d) Downstream luminosity monitor asymmetry versus slug for run 2.

Figure 4.10: Upstream and downstream luminosity monitor asymmetry versus slug for run 1 and run 2. Asymmetries have been corrected for helicity correlated beam motion.

4.3.3 Luminosity monitor as null asymmetry check

Part of the luminosity monitor design was to provide a null asymmetry test. Since the luminosity monitors have a much smaller physics asymmetry ($\mathcal{O}$(10 ppb)) than the main detectors, they would be ideal to look for false asymmetries [65].

Both the upstream and downstream luminosity monitors saw very large ($\mathcal{O}$(1 ppm)) asymmetries [39]. This was unexpected, but as discussed throughout this chapter, comes from

the large asymmetry carried by the beamline background. The upstream and downstream luminosity monitor asymmetries during run 1 and run 2 can be seen in figure 4.10. When the slow helicity reversal IHWP is inserted and removed, the asymmetry is expected to flip if it is a true physics asymmetry (or remain zero in an ideal null check). That does not happen here, due to false asymmetry from background. As discussed in section 5.3.3, these monitors were used to make a correction for this background false asymmetry [10, 113].

4.3.4 Handling luminosity hardware failures

The upstream luminosity monitors suffered several hardware failures, as discussed in section 4.3.1. Since the asymmetry would be necessary for the Q_{weak} beamline background correction, a reliable asymmetry had to be calculated for periods where single tubes as well as whole bars failed.

Table 4.1: Upstream luminosity monitor (uslumi) failure modes and how `uslumi_sum` was defined during those periods [43].

Failed uslumi PMTs	`uslumi_sum` definition
7pos	(1neg + 1pos + 3neg + 3pos + 5neg + 5pos + 7neg + 7neg)/8
5pos	(1neg + 1pos + 3neg + 3pos + 5neg + 5neg + 7neg + 7pos)/8
1pos	(1neg + 1neg + 3neg + 3pos + 5neg + 5neg + 7neg + 7pos)/8
5neg & 5pos	(3neg + 3pos + 7neg + 7pos)/4

The Q_{weak} analyser software used map files to store which PMTs were attached to which ADC as well as to tell the software which sums to compute. `uslumi_sum` is the variable used for the straight average of all 8 upstream luminosity monitor PMT asymmetries. The azimuthal

symmetry helps to make the detector less sensitive to transverse leakage and natural beam motion.

In order to preserve symmetry as much as possible, the following scheme was used; if only a single PMT in a bar fails, the good tube in that bar is included twice [43]. If two PMTs in a single bar failed, that bar, and the bar opposite were removed from the sum completely. Table 4.1 shows the various failures observed in Q_{weak} and the definition of `uslumi_sum` for that period.

4.4 Simulation

Extensive simulation was done by J. Leacock in the planning and design phase for the luminosity monitors using GEANT3 [65]. During the running of Q_{weak}, several questions emerged involving the sensitivity of the downstream luminosity monitors to beam position and the source of signal in the upstream luminosity monitors.

In order to address these concerns, basic versions of the upstream and downstream luminosity monitors were implemented in the Q_{weak} Geant4 simulation, which had a more accurate beamline. These consist of rectangular quartz bars of the proper size. Light guides and PMTs, which would be necessary for exact determination of light yields via simulation, were not implemented as for the main detectors because it was deemed unnecessary for these studies. Renderings from Geant4 can be see in figure 4.11.

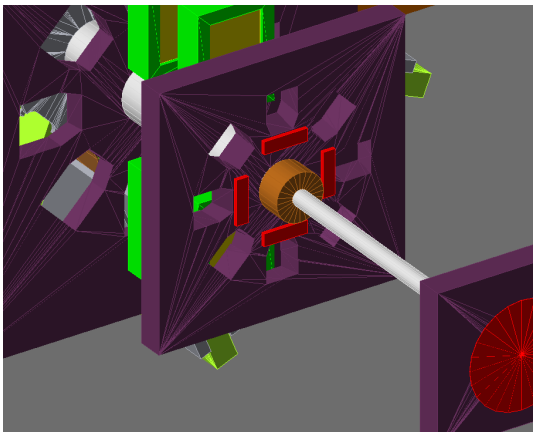

(a) Basic Geant4 implementation of the upstream luminosity monitors.

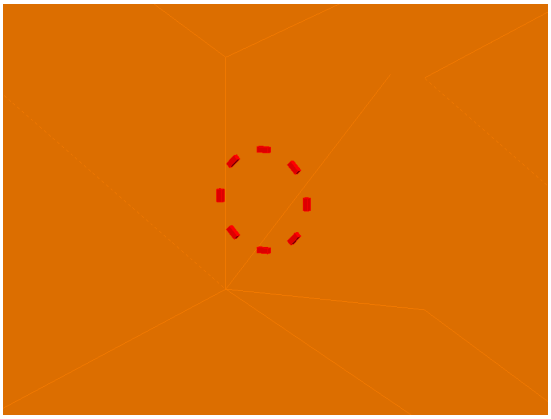

(b) Basic Geant4 implementation of the downstream luminosity monitors.

Figure 4.11: Basic Geant4 implementation of the upstream and downstream luminosity monitors.

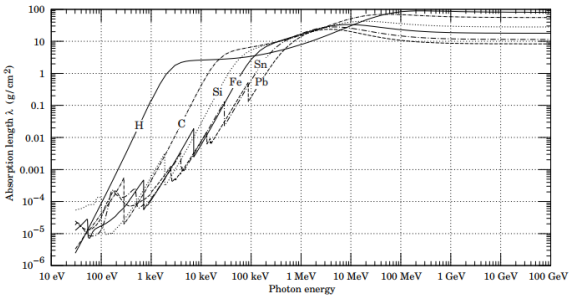

Figure 4.12: Photon attenuation lengths in various materials [85]. For the luminosity monitors, Si is of interest since they are constructed of quartz.

Unlike the Q_{weak} main detectors, for which a complete, realistic hardware implementation was necessary, the luminosity monitors only contain basic implementations of the hardware. As such, no PMTs are implemented. This means that some care must be given when computing rates, since photoelectron cuts cannot be used to rejected hits which do not generate Čerenkov light. For photons, a 1 MeV overall cut is applied (see figure 4.13 for a plot of Čerenkov photoelectrons versus energy), and for events that do pass this cut, an efficiency factor of 0.15 is applied (see figure 4.12 for a plot of photon attenuation in quartz) [26, 85].

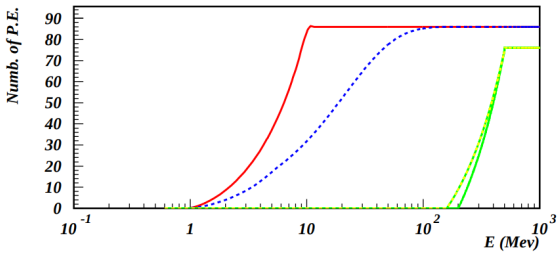

Figure 4.13: Photon and electron photoelectron yields for various particles [26]. Red is electrons, blue is photons, yellow-green is muons and solid green is pions.

For electrons a 10 MeV cut is applied [26]. There is some turn on between 1 and 10 MeV (shown in figure 4.13), but the differences between rates with a 1 MeV and 10 MeV cut are so small that this is negligible in these studies. Rates presented in this section represent the sum of the photon and electron rates for a given physics process which have been extracted separately.

4.4.1 Upstream luminosity monitor signal portion

During run 2, it was determined that the upstream luminosity monitors were very sensitive beamline backgrounds, especially those coming from the beamline collimator (see section 3.4.2). There was nothing but air between the beamline collimator and the upstream luminosity monitors, so they had a large effect on the signal seen by the upstream luminosity monitors.

During run 2, custom built tungsten shutters could be placed into octants 1 and 5 to block elastically scattered electrons and help understand beamline backgrounds. The full details of this study can be found in section 5.3.3, but it seemed that roughly half the signal seen

by the upstream luminosity monitor had scattered from the beam collimator [41]. In some instances, e.g. during times of high halo, the ratio was observed to be higher.

This simulation study was designed to look at sources of upstream luminosity monitor rate from three regions: electrons that pass though the first collimator and hit the quartz, electrons that hit the tungsten beamline collimator and then hit the quartz, and electrons that punch through the tungsten shutters and then hit the quartz. Two different Geant4 generators were used: one simulating e-p scattered electrons, and one simulating Møller scattered electrons.

Previous work had been done by M. McHugh to implement a more accurate version of the tungsten beamline collimator [77]. In order to simulate the signal from the tungsten beamline collimator, events were thrown into an angular range of $0.3^\circ - 4^\circ$ in ϕ and from $0^\circ - 360^\circ$ in θ. 0.3° ϕ was used instead of 0° as the generator can have buffer overflow and divide by zero errors at very small angles. The angular distribution is flat in $\cos(\theta)$ and in ϕ.

The following sources signal were studied: e-p scattered electrons hitting the beamline collimator, Møller electrons hitting the beamline collimator, e-p electrons scattering through the first collimator hole, Møller electrons scattering through the first collimator hole, e-p electrons punching through the tungsten shutter and Møller electrons punching through the tungsten shutters. In order to compute the ratio of blocked rate to unblocked rate, the following formula is used,

$$f_{\text{lumi,msr,sim}} = \frac{R_{\text{ep,punchthrough}} + R_{\text{Møller,punchthrough}} + R_{\text{ep,beamline}} + R_{\text{Møller,beamline}}}{R_{\text{ep,beamline}} + R_{\text{Møller,beamline}} + R_{\text{ep,hole}} + R_{\text{Møller,hole}}}, \qquad (4.1)$$

where $f_{\text{lumi,msr,sim}}$ is the fraction of the simulated signal that the luminosity monitor sees with tungsten shutters installed over the total signal and the various $R_{\langle\text{process}\rangle,\langle\text{region}\rangle}$. This is used to compare to data. The actual fraction from the beamline collimator would not include the punch through rate, since this only occurs when the shutters are installed, and is given as

$$f_{\text{lumi,sim}} = \frac{R_{\text{ep,beamline}} + R_{\text{Møller,beamline}}}{R_{\text{ep,beamline}} + R_{\text{Møller,beamline}} + R_{\text{ep,hole}} + R_{\text{Møller,hole}}}, \tag{4.2}$$

where $f_{\text{lumi,sim}}$ is the actual simulated fraction of signal from the beamline collimator. All the various rates, as simulated, can be seen in table 4.2.

Table 4.2: Upstream luminosity monitor rates from simulation from various regions and physics processes.

Rate source	θ angular range	ϕ angular range	events	Rate (GHz)
$R_{\text{ep,punchthrough}}$	$4^\circ - 13.5^\circ$	$-16^\circ - 16^\circ$	1000000	0.47 ± 0.01
$R_{\text{Møller,punchthrough}}$	$4^\circ - 13.5^\circ$	$-16^\circ - 16^\circ$	1000000	3.3 ± 0.01
$R_{\text{ep,hole}}$	$4^\circ - 13.5^\circ$	$-16^\circ - 16^\circ$	1000000	2.4 ± 0.1
$R_{\text{Møller,hole}}$	$4^\circ - 13.5^\circ$	$-16^\circ - 16^\circ$	1000000	145.7 ± 0.1
$R_{\text{ep,beamline}}$	$0.3^\circ - 4^\circ$	$0^\circ - 360^\circ$	10000000	31.8 ± 21.1
$R_{\text{Møller,beamline}}$	$0.3^\circ - 4^\circ$	$0^\circ - 360^\circ$	1000000	44.0 ± 5.7

Using the values from 4.2 and equations 4.1 and 4.2, it is possible to obtain the simulated experimentally observed ratio as well as

$$f_{\text{lumi,msr,sim}} = 36 \pm 10\ \%, \tag{4.3}$$

$$f_{\text{lumi,sim}} = 34 \pm 10\ \%. \tag{4.4}$$

As discussed in section 5.3.3, the simulated value is close to, but not in perfect agreement with, the measured value of $f_{\text{lumi,msr}} = 50$ %.

4.4.2 Downstream luminosity monitor sensitivity

During the running of Q_{weak}, the sensitivity of the downstream luminosity monitors to position was observed to have a sign opposite of those of the main detectors. For example, over run 2, the downstream luminosity 1 monitor and main detector 1 X-axis position sensitivities are shown in table 4.3.

Table 4.3: Sensitivity of the downstream luminosity monitors and the main detectors.

Detector	Detector X-axis sensitivity (ppm/nm)
Downstream luminosity monitor 1	0.3393 ± 0.0003
Main detector 1 barsum	-0.008429 ± 0.00001

Intuitively, a main detector and a downstream luminosity monitor in the same octant would have the same sensitivities to beam motion. However, that was not observed. The majority of the downstream luminosity monitors comes from the tungsten beamline collimator. This could potentially cause a higher flux of electrons when intuition indicates you would see a smaller flux. The main detector sensitivity does make intuitive sense and the signal increases as the beam moves closer.

In order to verify that this was indeed the cause of the sensitivity discrepancy seen in table 4.3, a study using the newly implemented Geant4 downstream luminosity monitor was conducted. A position scan of the downstream luminosity monitors was conducted and rate

versus position slopes were extracted. Slopes were extracted with and without the beamline collimator in the simulation. An exact match to observed sensitivities is not expected, but opposite signs of the slope with and without the tungsten beamline collimator would confirm the beamline collimator as the source of discrepancy. Also, a similar simulation was run to extract the position versus rate of the main detectors, to confirm it has the opposite sign of the downstream luminosity monitors with the beamline collimator. This will account for opposite signs occurring from the use of different coordinate systems.

The results for this study can be see in in figure 4.14. The slope for downstream luminosity monitor rate versus position without the plug (shown in figure 4.14a) is positive (although the error on the slope is somewhat high). This matches with the main detector versus position slope (shown in figure 4.14c), which is also positive. This intuitively makes sense given the detector geometries. The slope for the downstream luminosity monitor rate versus position with the beamline collimator (shown in figure 4.14b) shows the opposite sign. This agrees with what was shown experimentally and confirms that the beamline collimator is causing this effect. Qualitatively, this makes some sense as well. Without the beamline collimator, things intuitively make sense and the signal increases as you move the beam closer. With the beamline collimator installed, as the beam moves closer to the detector, it scatters and blocks more electrons from entering the detector, resulting in the signal decreasing as the beam moves closer to the detector.

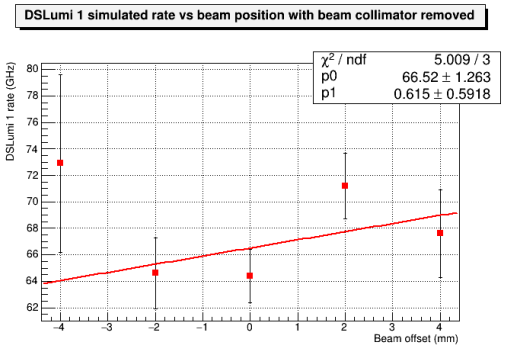

(a) Simulated rate of the downstream luminosity monitor rate versus beam position with beamline collimator removed from simulation. The slope is expected to match the main detector rate versus position slope in sign but not necessarily in magnitude.

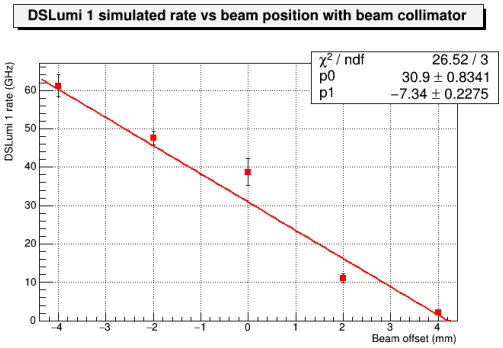

(b) Simulated rate of the downstream luminosity monitor rate versus beam position with beamline collimator included in the simulation. The slope is expected to be opposite that of the main detector rate versus position slope.

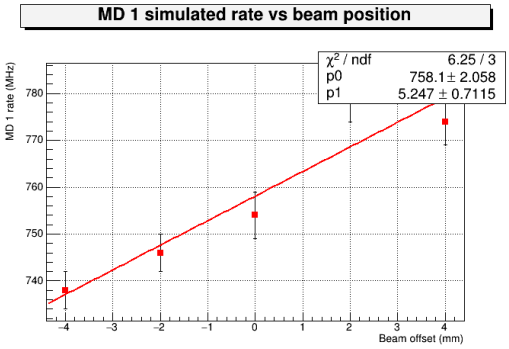

(c) Simulated rate of the main detector rate versus beam postition with beamline collimator included in the simulation.

Figure 4.14: Simulated slopes of downstream luminosity monitor versus beam position with (4.14a) and without (4.14b) beamline collimator and main detector rate versus beam position (4.14c).

Chapter 5

Elastic Electron-Proton Analysis

5.1 Introduction

The Q_{weak} asymmetry analysis was a large undertaking involving work by many individuals across several institutions. As such, some of the analysis described here represents work not done by the author of this thesis. Please see appendix B for a complete list of topics worked on by this author. This thesis will contain the final Q_{weak} result. Several other referenced theses contain a partial analysis or a blinded analysis.

5.2 Extracting the measured asymmetry

5.2.1 Raw asymmetry

In equation 2.51, the asymmetry is related to the cross sections in helicity states + and −. As explained in chapter 3, the Q_{weak} apparatus does not measure the cross section, but the yield integrated over time. The way Q_{weak} calculates the asymmetry first by calculating the asymmetry separately for each tube as [71]

$$A^i_{\text{tube}} = \frac{Y^{+i}_{\text{md}} - Y^{-i}_{\text{md}}}{Y^{+i}_{\text{md}} + Y^{-i}_{\text{md}}}, \tag{5.1}$$

where A^i_{tube} refers to the i-th PMT tube, $Y^{\pm i}_{\text{md}}$ refers to i-th PMT tube signal normalized to beam charged (as seen in equation 3.5). To form the final asymmetry, all 16 PMT asymmetries are averaged as

$$A_{\text{raw}} = \frac{\sum_{i=1}^{16} A^i_{\text{tube}}}{16}. \tag{5.2}$$

This is the raw, uncorrected measurement from the apparatus. There is also no isolation of the physics processes needed to extract the weak charge of the proton.

In order to extract a measured asymmetry, false asymmetries from a variety of sources need to be corrected. A_{raw} can be written as [29]

$$A_{\text{raw}} = A_{\text{msr}} - A_{\text{false}}, \tag{5.3}$$

where the raw asymmetry is a combination of the measured asymmetry from the apparatus and the false asymmetry.

Before a raw asymmetry could be extracted, a consistent dataset had to be defined. The Q_{weak} collaboration analysed the raw DAQ output files several times; each analysis was named with a pass number. In each case, improvements were made to the analysis software which was expected to change the result. Details on the analysis engine changes can be found in R. Beminiwattha's thesis [23]. Additionally, smaller changes were made to the database to correct errors in files that define various detectors and parameters; these changes were designated with a letter. For the final analysis, analysis pass5c+ was used. Here, the plus indicates some data from beam modulation was added back into the final dataset [110, 113].

The raw asymmetries were extracted from run 1 and run 2 separately, since they are technically two separate measurements. How these two results were combined will be discussed later in this thesis. The final extracted raw asymmetries are [113]

$$\text{run 1: } A_{\text{raw}} = -217.99 \pm 13.15 \text{ ppb}, \tag{5.4}$$

$$\text{run 2: } A_{\text{raw}} = -164.01 \pm 7.38 \text{ ppb}, \tag{5.5}$$

where the uncertainty is statistical. At first it may appear that there is a 2σ difference between run 1 and run 2, but, as will be explained in the next section, this is due to different blinding factors and other corrections that differ between run 1 and run 2.

5.3 Extracting the measured asymmetry

As was discussed in section 3.1.3, the Q_{weak} apparatus was designed with strong azimuthal symmetry to reduce false asymmetry from sources like natural beam motion and residual transverse polarization. The experiment is not perfectly symmetric, so measurement and correction for both of these effects needs to be taken into account. There are also several other sources of false asymmetry. Equation 5.3 can be rewritten as [11]

$$A_{\text{msr}} = A_{\text{raw}} + A_{\text{BCM}} + A_{\text{beam}} + A_{\text{BB}} + A_L + A_T + A_{\text{bias}} - A_{\text{blinding}}. \tag{5.6}$$

The various A's refer to false asymmetries which will be discussed throughout this section. Short descriptions and relevant sections for these variables can be found in table 5.1.

Table 5.1: False asymmetry, descriptions, and sections which cover them.

False asymmetry	Description	Section
A_{BCM}	BCM normalization error	5.3.1
A_{beam}	Helicity-correlated beam motion correction	5.3.2
A_{BB}	Beamline background correction	5.3.3
A_L	Nonlinearity correction	5.3.4
A_T	Transverse leakage correction	5.3.5
A_{bias}	Rescattering bias correction	5.3.6
A_{blinding}	Blinding factor	5.3.7

5.3.1 BCM normalization error

Because the detector signals were charge normalized (see equation 3.5), the asymmetry associated with the BCM correction is zero, but there is an error associated with it. Normally,

this would be determined by looking at the double difference between two BCMs (i.e. the difference between two charge asymmetries) in the same location to determine BCM resolution which would determine the error on A_{BCM}.

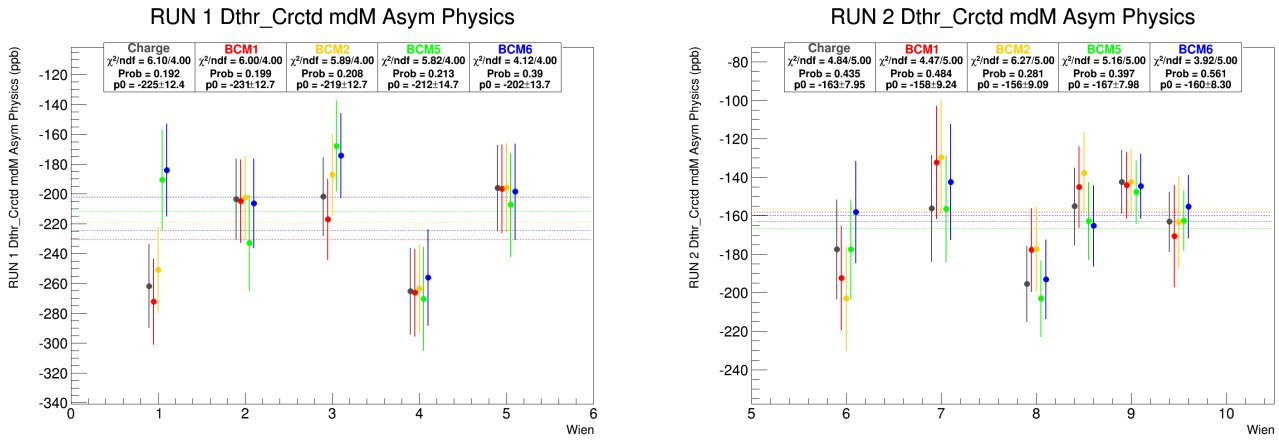

Figure 5.1: Raw physics asymmetries for run 1 and run 2 by wien showing the differences between different BCM normalizations [107].

Due to an unexplained 30% residual charge correlation even after beam normalization with BCM1 and BCM2 [111], the decision was made to renormalise using BCM5 and BCM6. Doing so removed the residual charge correlation as well as improved the χ^2 of null asymmetries [107]. The raw physics asymmetry normalized by the various Q_{weak} BCMs can be see in figure 5.1.

Run 1, as stated above, used a combination of BCM5 and BCM6 to normalize the signal [111]. In run 2, a combination of BCM5, BCM6, and BCM8 was used. Using a combination

of BCM noise and scaled error, the BCM normalization error was determined to be

$$\text{run 1: } A_{\text{BCM}} = 0 \pm 4.44 \text{ ppb}, \tag{5.7}$$

$$\text{run 2: } A_{\text{BCM}} = 0 \pm 2.07 \text{ ppb}, \tag{5.8}$$

where the errors are systematic. This represents the systematic that comes from the BCM resolution which was used to normalize the raw asymmetry. The resolution was determined by comparing the difference between two or more BCMs.

5.3.2 Helicity-correlated beam motion correction

Helicity-correlated beam motion causes a false asymmetry that needs to be corrected. Q_{weak} had two different ways to correct for this effect; linear regression of natural beam motion, described in section 3.1.3, and driven beam modulation described in section 3.1.4. A correction as well as a systematic error were assigned from this as A_{beam} (and was also referred to as A_{reg} in [10]).

Regression relies on natural beam motion to extract the sensitivity to beam motion [112]. Usually, this works well, but in cases where the beam does not move much, beam monitor noise can make it difficult to accurately determine sensitivities. Beam modulation, on the other hand, uses coils to move the beam with a large amplitude and thus determine a more accurate sensitivity. For this reason, except where no beam modulation was available (usually due to hardware issues or lack of implementation), beam modulation was used to

make a correction. In the analysis of the beam modulation data, it was discovered that part of the response to beam dithering could not be explained fully using only the five BPM's [105, 112]. This indicates another unintentional and unmeasured variable was affected by dithering.

Regression and beam modulation were compared to test how well these two methods agreed [105]. While this may sound like a trivial comparison to make, there were several subtleties that needed to be taken care of. Since beam monitors will have correlations, a set of so-called natural monitors were constructed which removed these correlations and normalized to monitor noise [104].

During the beam correction analysis, it was discovered that there were some nontrivial differences between regression and beam modulation [105, 109]. Using the natural monitors, it was discovered that MPX and MPY had large sensitivity discrepancies between beam modulation and natural beam motion, as can be see in figure 5.2. The key to understanding the reason for this lies in the monitor noise [103].

The BPM monitor widths are shown in figure 5.3. Both the X' and Y' show very low monitor noise [103, 106]. As previously stated, using linear regression in cases of low monitor noise tends to produce inaccurate sensitivities. This is the cause for the discrepancies seen in X' and Y' between linear regression and beam modulation [112].

Since beam modulation was not fully constrained with only 5 monitors and no explanation or hidden variable could be found, a scheme dependent systematic error was applied [112]

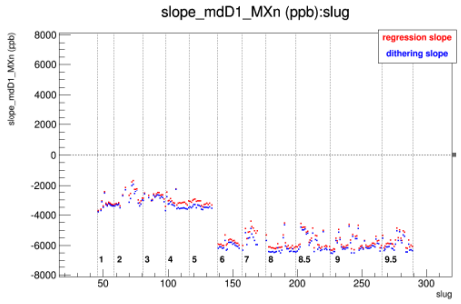

(a) Main detector sensitivity to natural monitor X.

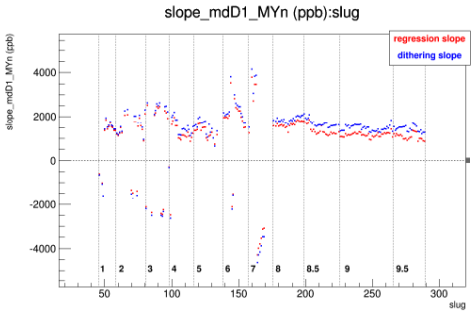

(b) Main detector sensitivity to natural monitor Y.

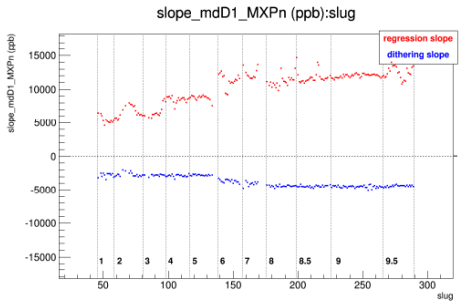

(c) Main detector sensitivity to natural monitor X'.

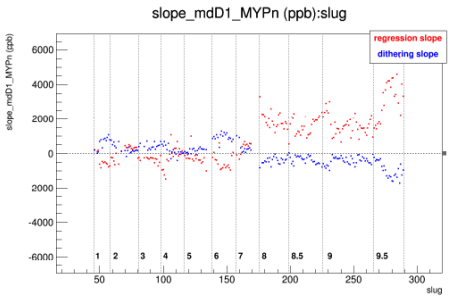

(d) Main detector sensitivity to natural monitor Y'.

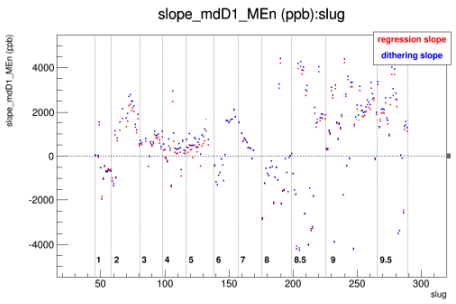

(e) Main detector sensitivity to natural monitor E.

Figure 5.2: Comparison of main detector asymmetry sensitivity between regression (red) and beam modulation (blue) [105]. Presented on the slug timescale.

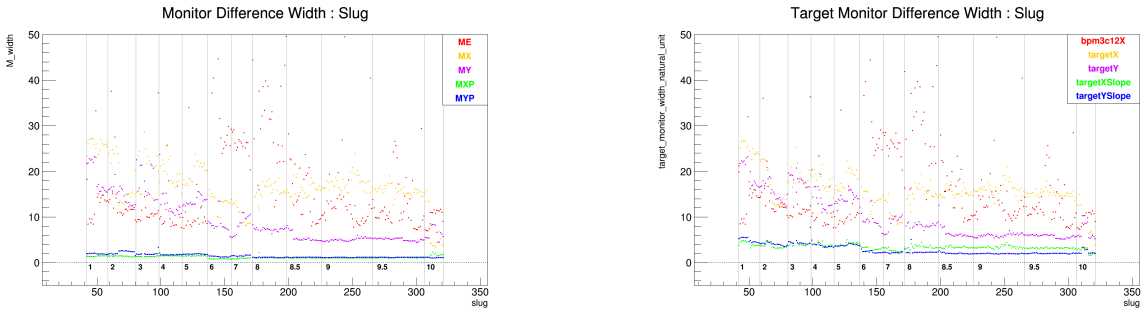

(a) Natural BPM monitor widths.

(b) Physical BPM monitor widths.

Figure 5.3: Both natural and physical BPM monitor widths for all 5 measured variables [103]. Presented on the slug timescale.

as well as a systematic error for how accurately beam modulation could determine sensitivities. Additionally, the beam was modulated 90° out of phase with the fast feedback system (designed to keep the charge asymmetry under 10 ppb, see section 3.1.3 for details). This allowed the phase space to be redundantly measured which helped to constrain the systematic error [11]. A final correction for helicity-correlated beam motion was determined to be [113]

$$\text{run 1: } A_{\text{beam}} = 18.5 \pm 4.11 \text{ (scheme)} \pm 0.08 \text{ (sensitivity) ppb}, \tag{5.9}$$

$$\text{run 2: } A_{\text{beam}} = 0.0031 \pm 1.07 \text{ (scheme)} \pm 0.26 \text{ (sensitivity) ppb}. \tag{5.10}$$

The much larger correction in run 1 is due to larger helicity-correlated position, angle and energy differences.

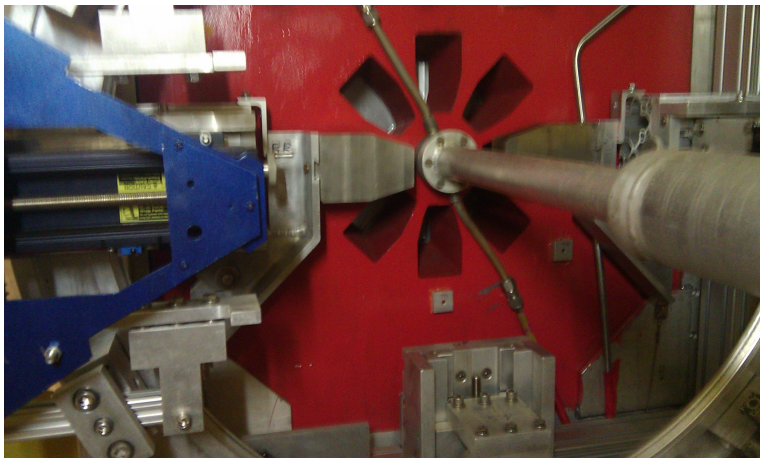

Figure 5.4: Picture of the tungsten shutters installed on collimator 1. The beamline collimator is also shown.

5.3.3 Beamline background correction

Despite the effort put into simulation and shielding (see 3.4.1), a correction for beamline background was still necessary. The beamline background fraction and asymmetry were first measured by using removable tungsten shutters. Installing these shutters took proper planning and production quality data could not be taken while they were installed. Only a few studies were conducted during run 2 and none during run 1 (although several similar studies were done by using lead bricks to block octant 7 were done; see Myers' thesis for details [79]), so an alternate method for studying how the background changed over the entire running of the experiment was also developed.

The tungsten shutters, shown in figure 5.4, were installed on collimator 1 (see section 3.4.1) during the accelerator upgrades between run 1 and run 2. They consist of 9 radiation lengths thick tungsten and would block octants 1 and 5. While this was enough to stop most

scattered electrons passing through the collimator hole, simulations showed that it was not enough to completely stop all scattered electrons [52].

The tungsten shutter studies allowed the Q_{weak} experiment to gain insight into both the asymmetry of the beamline background, as well as what fraction of the main detector and upstream luminosity monitor signal came from the beamline background. The goal of the tungsten shutter studies was to understand the relationship between accelerator optics, halo, and the beamline background. At times, attempts were made to detune the accelerator optics to produce more halo and study its effect on the background. Some runs were short, just to study detector yields and yield fractions, while others were longer to study asymmetries [32].

Table 5.2: Fractional yields in blocked detectors [34, 35, 41]. For uslumi 5, only uslumi5neg was active, see 4.3.4 for details.

Detector	Good halo fractional yield (%)	Bad halo fractional yield (%)	Difference (%)
md1barsum	0.191	0.232	0.041
md5barsum	0.159	0.203	0.044
md9barsum	8.01	9.06	1.05
qwk_uslumi1neg	50.5	59.05	8.54
qwk_uslumi1pos	51.6	61.33	9.73
qwk_uslumi5neg	49.1	58.85	8.54

To determine the fractional yields, runs with the tungsten shutters install were compared to runs where they were removed. The fractional yield is simply the blocked yield divided by the unblocked yield. This was done for a variety of halo conditions. Results by halo conditions and detector can be seen in table 5.2. There is a clear increase in fractional yield in the bad halo conditions. Table 5.2 lacks any error bars. While statistical errors are

negligible because yields are very accurately determined, systematic errors were hard to pin down due to the very small number of runs taken with the tungsten shutters installed and the variability in yield due to a variety of factors. Ultimately, the difference between good and bad halo periods was used to quantify the error (similar to work done for a different blocking method done in run 1, see K. Myers' thesis for details [79]) and

$$f_{\mathrm{BB,LH_2},shutter} = 0.19 \pm 0.06\ \%, \tag{5.11}$$

$$f_{\mathrm{BB,Al},shutter} = 0.65 \pm 0.16\ \%, \tag{5.12}$$

where the errors are statistical, were ultimately taken as the result of this study [36], where $f_{\mathrm{BB,LH_2}}$ is the fractional yield for liquid hydrogen and $f_{\mathrm{BB,Al}}$ is the fractional yield for aluminum.

Table 5.3: Regressed asymmetries in blocked detectors and PMT background detector (unblocked) with statistical errors [33].

Detector	Asymmetry (ppm)
md1barsum	99 ± 7
md5barsum	88 ± 7
uslumi1	44 ± 1
uslumi5	55 ± 1
pmtonl	51 ± 6
pmtltg	62 ± 4

Detector yields can be determined very accurately with only a 1 minute run, but to determine asymmetries requires much longer runs, depending on the size of the asymmetry. Table 5.3 has a list the asymmetries measured during bad halo conditions. Based on the results from

tables 5.2 and 5.3, there is a very small fraction of beamline background that carries a very large asymmetry.

Given the geometry when the octants are blocked and the fact that the upstream luminosity monitor sees a large signal when blocked, the likely source of this background is from the tungsten beam collimator (see section 3.4.2 for details). Based on section 4.4.1, a large part of the upstream luminosity monitor signal did in fact come from the beam collimator. A simulation was also conducted for the main detectors. However, since the signal fraction is much smaller, a much larger number of events was generated. This simulation showed a yield ratio of

$$f_{\mathrm{BB,LH_2,sim,LH_2},sim} = 1.246 \pm 0.31\ \%, \tag{5.13}$$

where errors are statistical and $f_{\mathrm{BB,LH_2},sim}$ is the simulated rate from the tungsten plug. For this simulation, LH_2 electrons were thrown in to the beam collimator using an angular range of

$$\sigma = 0.3 - 4^{\circ}, \tag{5.14}$$

$$\phi = 0 - 360^{\circ}. \tag{5.15}$$

Below 0.3° , the Geant4 generator produces non-physical cross sections. The angular distribution is flat in $\cos(\theta)$ and in ϕ. The yield from this study was compared with a normal Q_{weak} simulation to produce the simulated fractional yield in equation 5.13. This disagrees with the fractional yield measured in the tungsten shutters studies by a factor of $\sim$7. How-

ever, due to the relationship between beam halo and fractional yield, it is difficult to pin down exactly how comparison to data should be done.

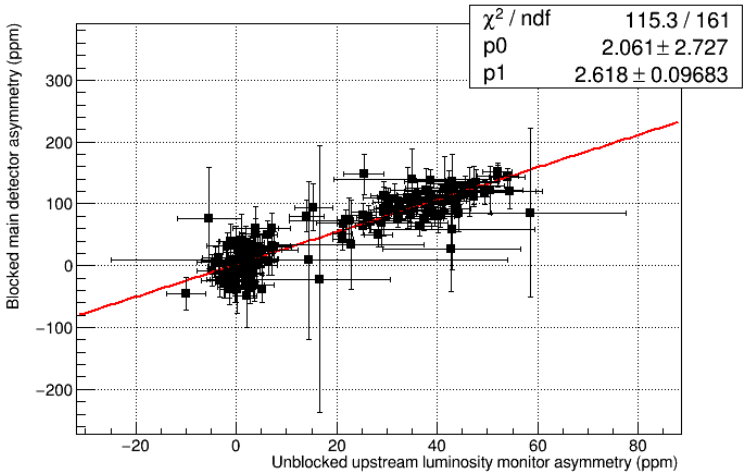

Figure 5.5: Correlation between unblocked upstream luminosity and blocked main detector using all tungsten shutter data available [86].

The final piece of the puzzle was the correlation between the various background detectors (upstream luminosity monitor and the PMT background monitors, see section 3.7) and the blocked main detector asymmetry. Since the PMT background detectors moved several times during the running of Q_{weak}, it was decided that the final correction would be made using the upstream luminosity monitor. The correlation between the upstream luminosity monitor asymmetry and main detector asymmetry for the entire set of tungsten shutter data can be see in figure 5.5.

Since the tungsten shutter studies revealed that a small fraction of the main detector signal carried a large asymmetry, and that this asymmetry was highly correlated to what the

upstream luminosity monitor saw, and that it could change depending on beam conditions, a correction technique was developed to handle these effects [61].

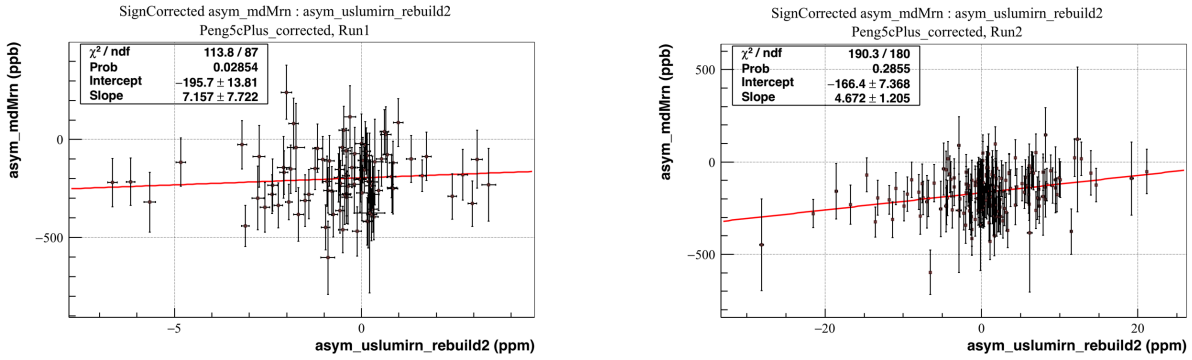

(a) Correlations between main detector and upstream luminosity monitor during run 1.

(b) Correlations between main detector and upstream luminosity monitor during run 2.

Figure 5.6: Correlation between upstream luminosity and main detector for both run 1 and run 2 on the slug level [59, 60]. Units are ppb/ppm.

Large correlations were also observed between the upstream luminosity monitor and main detector asymmetries, as shown in figure 5.6. While the correlation was much smaller during run 2 than the blocked octant study (when comparing figure 5.6 to figure 5.5 take careful note of the units), this is expected because only a small fraction of the main detector signal comes from the beamline background.

The correlation between main detector and beamline background is [87]

$$C^{\mathrm{MD}}_{\mathrm{uslumi}} = f_{\mathrm{BB}} m^{\mathrm{MD}}_{\mathrm{uslumi}}, \tag{5.16}$$

where $C^{\mathrm{MD}}_{\mathrm{uslumi}}$ is the correlation between the main detector and the upstream luminosity monitor, and $m^{\mathrm{MD}}_{\mathrm{uslumi}}$ is the slope. The correlations were determined to be [60]

$$\text{run 1: } C^{\mathrm{MD}}_{\mathrm{uslumi}} = 7.16 \pm 7.72 \text{ ppb/ppm}, \tag{5.17}$$

$$\text{run 2: } C^{\mathrm{MD}}_{\mathrm{uslumi}} = 4.67 \pm 1.21 \text{ ppb/ppm}, \tag{5.18}$$

where the error is from the fit. To compare this result to what was seen in the blocked octant studies, it is possible to take the blocked octant correlation from figure 5.10 and multiply it by the blocked octant fraction from equation 5.12, you get 4.6 ppb/ppm. This agrees very well with equation 5.18. Next, a correction is applied slug by slug using [91]

$$A^i_{\mathrm{BB}} = A^i_{\mathrm{msr}} - C^{\mathrm{MD}}_{\mathrm{uslumi}} A^i_{\mathrm{uslumi}}, \tag{5.19}$$

where i refers to the slug number. To extract a final number for the beamline background, once the slug by slug correction was made, it was compared to the raw A_{msr} to extract [59]

$$\text{run 1: } A_{\mathrm{BB}} = 3.92 \pm 4.23 \text{ (fit)} \pm 0.78 \text{ (model) ppb}, \tag{5.20}$$

$$\text{run 2: } A_{\mathrm{BB}} = -2.36 \pm 0.61 \text{ (fit)} \pm 0.92 \text{ (model) ppb}. \tag{5.21}$$

The Q_{weak} experiment made use of an insertable half-wave plate (see section 3.1.1 for details) and a wien filter as slow helicity reversals. This was done to study how sensitive the experiment was to false asymmetries that don't flip with beam helicity. Beamline background is

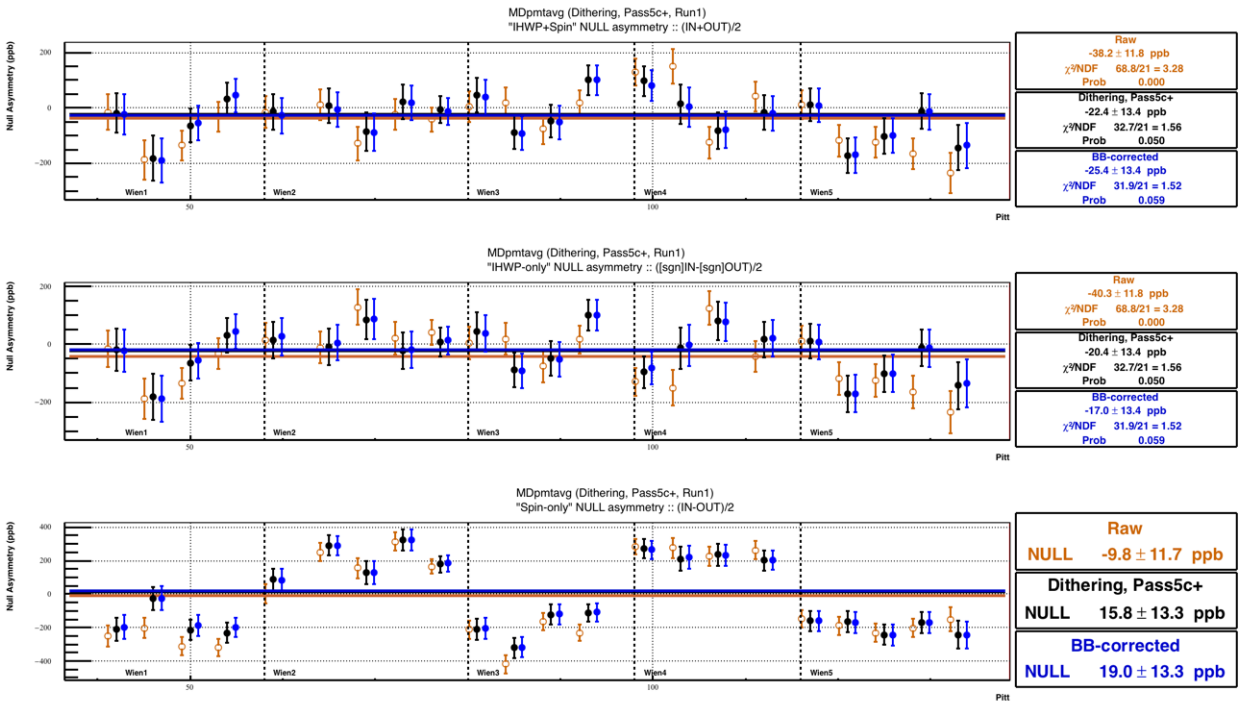

(a) Null asymmetry checks for run 1.

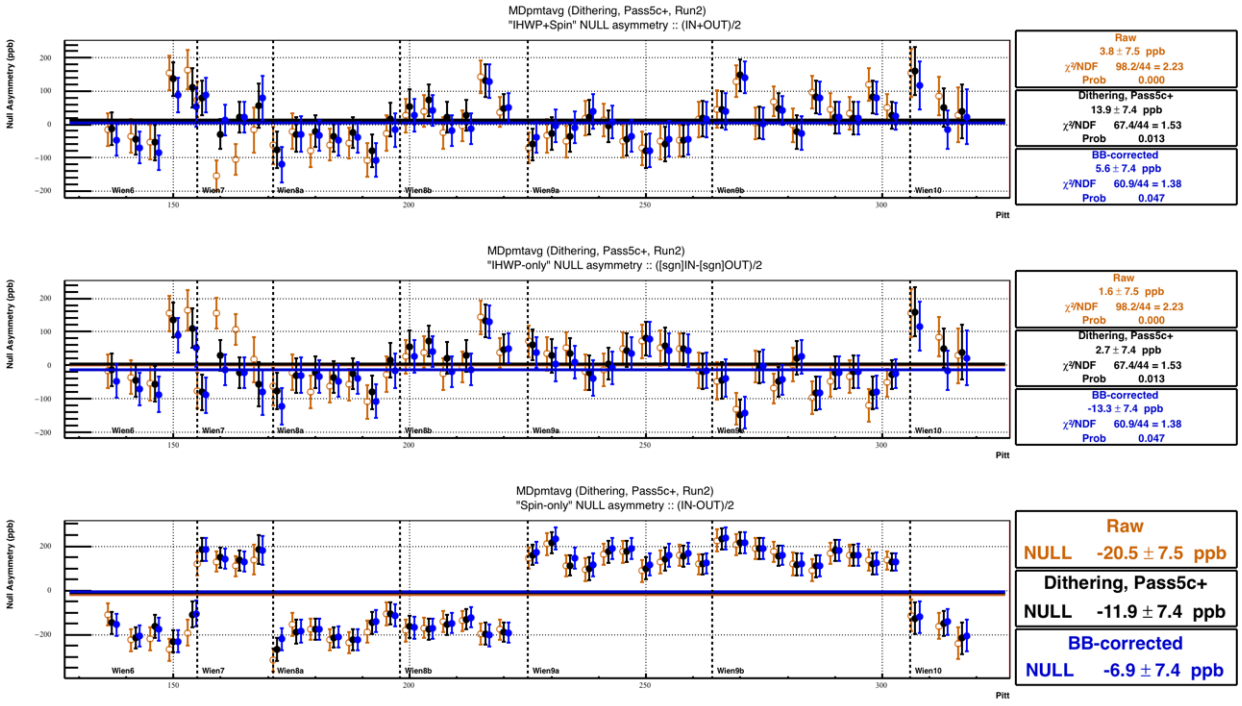

(b) Null asymmetry checks for run 2.

Figure 5.7: Null asymmetry checks for run 1 and run 2, computed on the timescale of several slugs (each point is made up of about 4 slugs) [59, 60].

just such an asymmetry. The null asymmetry can be defined in 3 separate ways: using both IHWP and spin flips, only using IHWP, and only using spin flips. The first way is simply

$$A_{\mathrm{NULL}} = \frac{A_{\mathrm{IN}} + A_{\mathrm{OUT}}}{2}, \tag{5.22}$$

where $A_{\mathrm{IN/OUT}}$ refers to the state of the IHWP. For IHPW only NULL,

$$A_{\mathrm{NULL,IHWP}} = \frac{\mathrm{sgn}A_{\mathrm{IN}} - \mathrm{sgn}A_{\mathrm{OUT}}}{2}, \tag{5.23}$$

where sgn is 1 for IHWP out and -1 for IHWP in. Finally, for spin flip only,

$$A_{\mathrm{NULL,spin}} = \frac{A_{\mathrm{IN}} - A_{\mathrm{OUT}}}{2}. \tag{5.24}$$

Plots of raw, dither corrected, and beamline background corrected asymmetries for run 1 and run 2 are shown in figure 5.7 over the timescale of several slugs (each point represents about 4 slugs). For all three versions of the null, adding in the beamline background correction improves the agreement with zero of the null asymmetry.

The effects of the beamline background correction can also be studied on the physics asymmetry in a similar way as the null. The physics asymmetry can be defined as

$$A_{\mathrm{PHYS}} = A_{\mathrm{IN}} - A_{\mathrm{OUT}}. \tag{5.25}$$

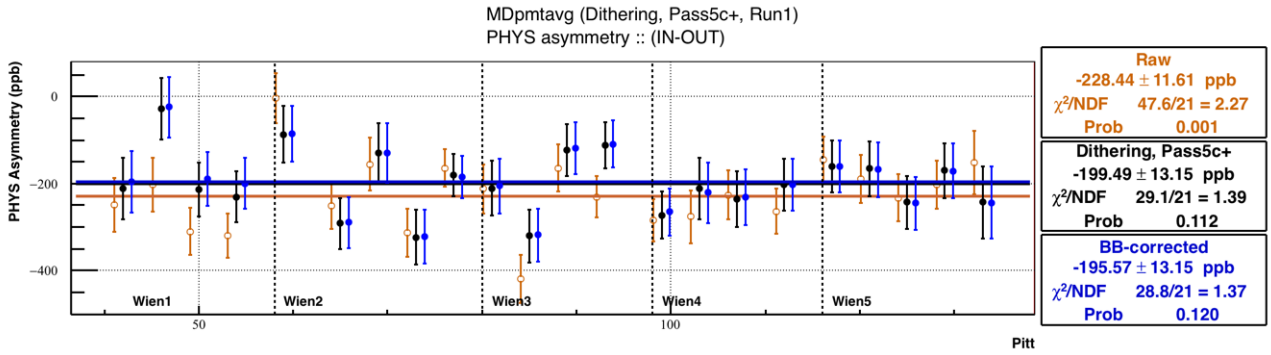

(a) Physics asymmetry checks for run 1.

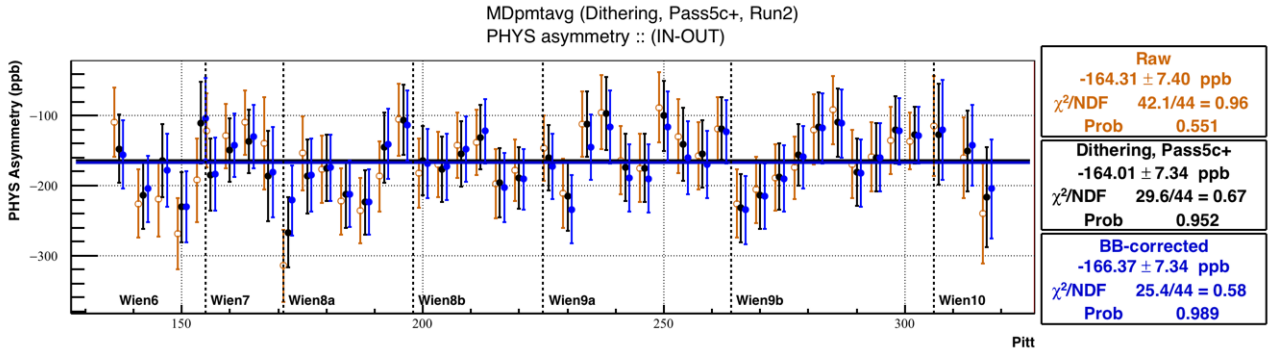

(b) Physics asymmetry checks for run 2.

Figure 5.8: Physics asymmetry checks for run 1 and run 2, computed on the timescale of several slugs (each point is made up of about 4 slugs) [59, 60].

The raw, dither corrected, and beamline background corrected physics asymmetries for run 1 and run 2 are shown in figure 5.8 over the same timescale of the previous null checks. Applying the beamline background correction in all cases improves the probability of the fits.

5.3.4 Nonlinearity

The nonlinearity in the Q_{weak} experiment comes into play in two ways. Taking into account only nonlinearity,

$$A_{\text{msr}} = (1 + \alpha_{\text{det}})A_{\text{phys}} + (\alpha_{\text{det}} - \alpha_{BCM})A_Q, \tag{5.26}$$

where α_{det} is the detector nonlinearity, α_{BCM} is the BCM nonlinearity, and A_Q is the charge asymmetry. The first part comes solely from the detector nonlinearity changing the physics asymmetry, the second part comes from the charge asymmetry.

The initial plan (and one that has been used in previous parity experiments) was to determine the detector nonlinearity using a separate regression scheme that included the normal five variables (see section 3.1.3) plus charge (sometimes referred to as 5+1 regression). Nonlinearity as measured by linear regression is made up of a series of effects including the true nonlinearity and can be written as

$$\alpha_{\text{regression}} = \alpha_{\text{det}} + \alpha_{\text{resolution}} + \alpha_{\text{BB}} + \alpha_{\text{BCM}}, \tag{5.27}$$

where α_{det} is the nonlinearity from the detector electronics, $\alpha_{\text{resolution}}$ is an apparent nonlinearity caused by regressing using the same BCM as charge normalization, α_{BB} is an apparent nonlinearity caused by beamline background, and α_{BCM} is the BCM nonlinearity. Some of these were difficult to properly constrain (specifically α_{BB}) and eventually the detector nonlinearity was determined through bench testing.

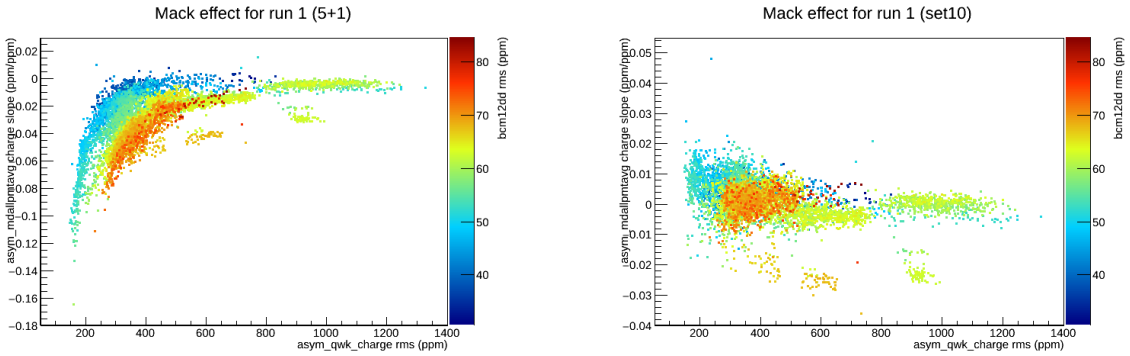

(a) Residual charge slope versus charge noise using 5+1 regression

(b) Residual charge slope versus charge noise using set10 regression.

Figure 5.9: Residual charge slope versus charge noise using 5+1 and set10 regression. A colorized z-axis shows the effect BCM noise. Data shown is from run 1.

5+1 regression used the same BCM combination that was used for for charge normalization (see section 5.3.1 for details). The effect ($\alpha_{\text{resolution}}$ in equation 5.27) occurs when low charge jitter or high BCM noise is present. Figure 5.9a shows a plot of of residual charge slope from regression versus charge noise, with a colorized z-axis also showing the effect of BCM noise. It is clear that there is an effect from both low jitter and noise. In order to combat this effect, a new regression set was developed using another BCM for charge regression referred to as set10. Figure 5.9b shows the same plot but with residual charge slopes from set10 regression. The effect is no longer present and $\alpha_{\text{resolution}} = 0$. All future slopes will be obtained using set10 regression.

α_{BB} was discovered when studying charge slopes during the tungsten shutter running and further studied using another data set where only odd octant main detectors had lead preradiators (referred to as 4 by 4 running). In the tungsten shutter runs, the main signal was blocked and only background was present. In 4 by 4 running, lead preradiators were installed

to reduce a low energy background (see section 3.6 for details). The even unradiated bars thus had a background that wasn't present in the 'blocked' detectors with preradiators.

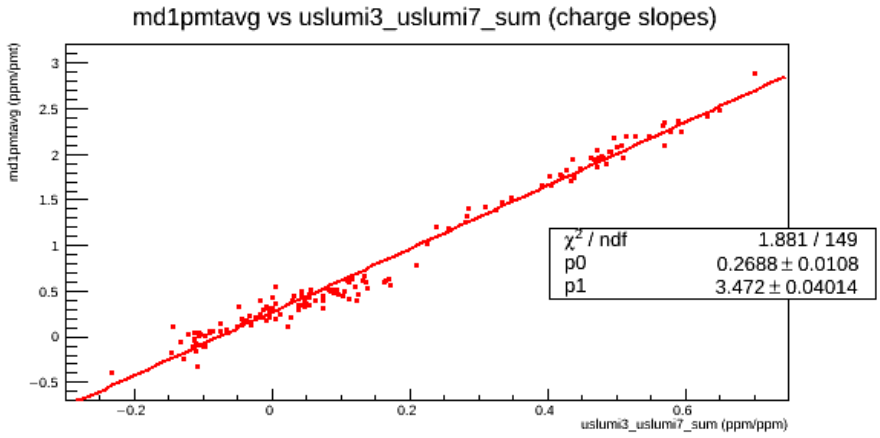

Figure 5.10: Correlation between unblocked upstream luminosity charge slope and blocked main detector charge slope using all tungsten shutter data available. Slopes calculated using set10 regression.

For the tungsten shutter running, blocked main detector residual charge slope was correlated to unblocked upstream luminosity monitor residual charge slope. This can be see in figure 5.10 and shows that the slopes are highly correlated. This means that the charge slope of a background detector is highly correlated to the charge slope from a background in the main detector. This fundamentally does not make sense, since the residual slope should be a property of the detector and electronics change.

A similar study was done with the 4 by 4 data set, only in this case, the unradiated even bars act as the background detector. Figure 5.11 shows the histograms of set10 by octant. Intuitively, there is no reason why the charge slope should change dramatically. However,

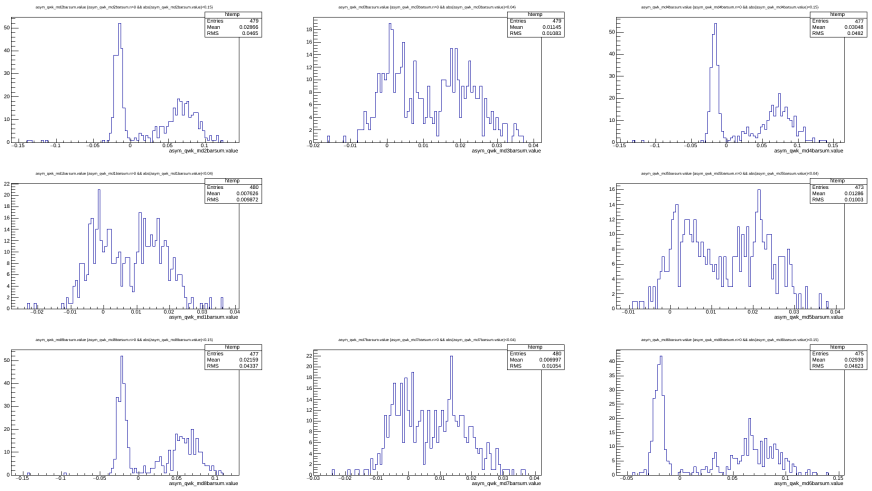

Figure 5.11: Set10 charge slopes by octant during 4 by 4 running, with octant 1 being at at 9 o'clock and going clockwise. Even bars lack lead preradiators. A clear and unexpected difference between charge slopes in blocked and unblocked octants can clearly be seen.

in figure 5.11 both the shapes and averages are different. There is again some effect by background on something which is believed to be simply an electronics effect.

The next study conducted was to look at correlations between blocked and unblocked detectors in the 4 by 4 dataset. Ideally, they would be highly correlated, since both detectors are expected to respond to changes in beam current similarly. Figure 5.12 shows that they are only about 20% correlated. This implies the background seen by the unradiated bars is causing a perceived nonlinearity.

The regression charge slope seems to be dominated by beamline background α_{BB}. Several models explaining this can be constructed, such as varying degrees of beam halo changing the background on a short timescale, thus changing the amount of charge going through the detector. This will look like a change in the beam charge that is not accounted for by charge asymmetry and thus be attributed to the nonlinearity.

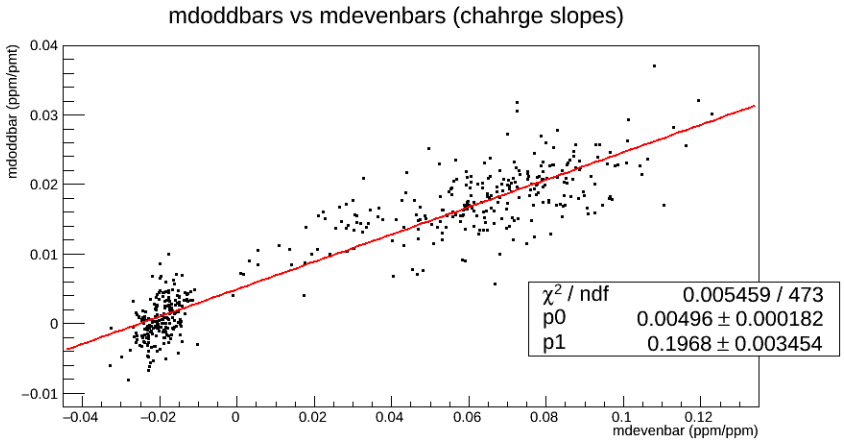

Figure 5.12: Correlation between radiated residual charge slope and unradiated main detector residual charge slope using 4 by 4 data. Slopes calculated using set10 regression. One point is one runlet of data.

Some effort was made to try and replicate beamline background correction techniques to try and extract the true nonlinearity. Main detector charge slopes were plotted versus upstream luminosity charge slope, as shown in figure 5.13. The fit intercept represents the nonlinearity after background effects are removed. The implied nonlinearity is

$$\text{run 1: } \alpha = 0.56 \pm 0.07 \text{ \%}, \tag{5.28}$$

$$\text{run 2: } \alpha = 0.88 \pm 0.03 \text{ \%}, \tag{5.29}$$

where the error is from the fit. There is also some unquantified systematic error as well. This number also includes any nonlinearity from the BCM. For these reasons, it became necessary to also conduct a bench test to determine the detector nonlinearity.

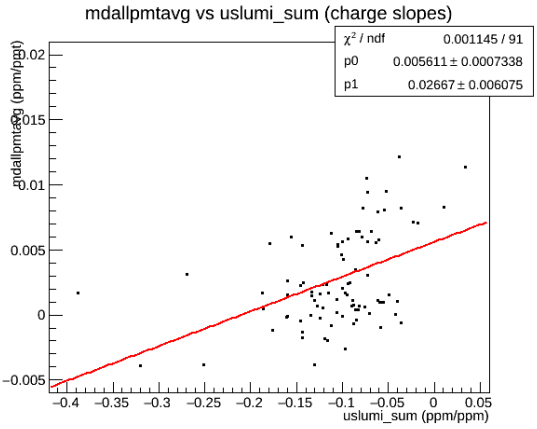

(a) Run 1 main detector charge slope vs upstream luminosity monitor charge slope.

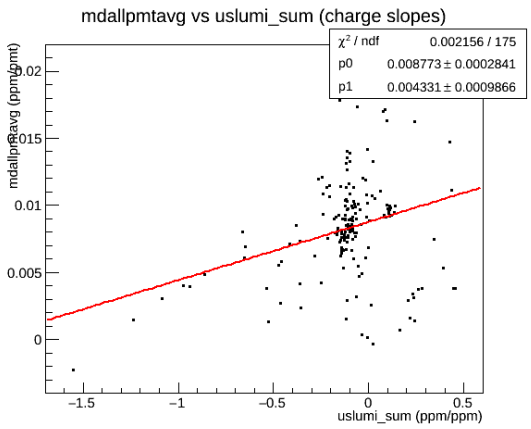

(b) Run 2 main detector charge slope vs upstream luminosity monitor charge slope.

Figure 5.13: Main detector charge slopes versus upstream luminosity monitor charge slopes for both run 1 and run 2. Each data point represents several hours of data.

One common cause of PMT nonlinearity is a space charge effects in the dynode causing the PMT gain to change with signal. The nonlinearity can characterized as

$$I = I_{\text{dark}} + \alpha L + \beta L^2, \tag{5.30}$$

where I is the photocurrent, I_{dark} is the dark leakage current, L is the illumination, α is the linearity, and β are the nonlinearities. In order to extract a dimensionless quantity, rewrite this expression in terms of $x = \beta L/\alpha$

$$I = I_{\text{dark}} + \alpha L(1 + x), \tag{5.31}$$

where x is the nonlinearity. This is the quantity measured in bench testing.

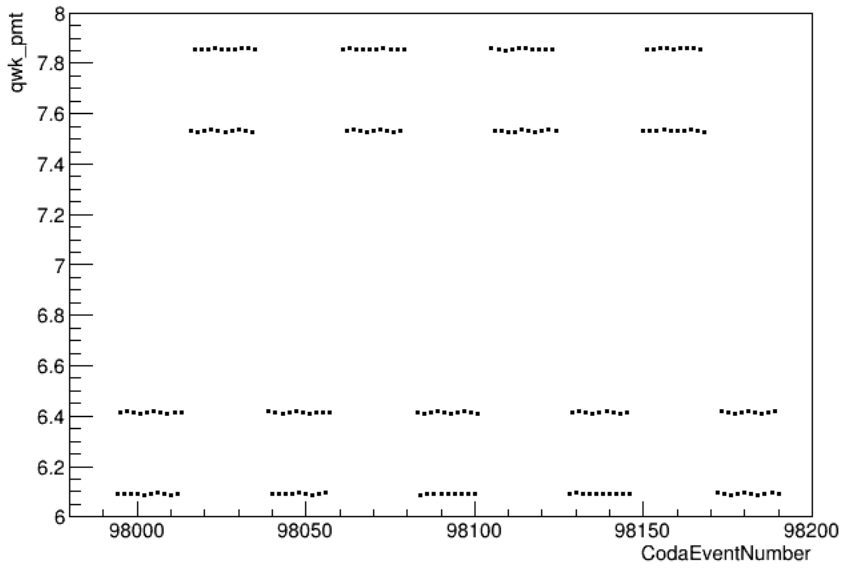

Figure 5.14: PMT signal generated by the bias, slow, and fast LEDs.

In order to measure the nonlinearity, a three LED setup was built. One LED acts as an offset bias, one LED has a slow signal (about 10 Hz) and one LED has a fast signal (varying, about 250 Hz) [74]. Figure 5.14 shows the PMT signal generated by the three LEDs. These LEDs were placed in a custom built dark box with a spare main detector PMT using the full Q_{weak} electronics chain including VQWK modules and preamps (see section 3.6 for details on the PMT and section 3.9.1 for details on the electronics chain). Each LED was a different color to prevent crosstalk.

Since there are three sources of illumination [75],

$$L = L_{\text{bias}} + L_{\text{slow}} + L_{\text{fast}}, \tag{5.32}$$

$$L^2 = L_{\text{bias}}^2 + L_{\text{slow}}^2 + L_{\text{fast}}^2 + 2(L_{\text{bias}}L_{\text{slow}} + L_{\text{slow}}L_{\text{fast}} + L_{\text{fast}}L_{\text{bias}}). \tag{5.33}$$

Then group the terms as

$$I_{\text{bias}} = \alpha L_{\text{bias}} + \beta L_{\text{bias}}^2, \tag{5.34}$$

$$I_{\text{slow}} = \alpha L_{\text{slow}} + \beta L_{\text{slow}}^2 + 2\beta L_{\text{slow}} L_{\text{bias}}, \tag{5.35}$$

$$I_{\text{fast}} = \alpha L_{\text{fast}} + \beta L_{\text{fast}}^2 + 2\beta (L_{\text{slow}} L_{\text{fast}} + L_{\text{fast}} L_{\text{bias}}), \tag{5.36}$$

where I_{fast} is the signal from the fast LED, I_{slow} is the signal of the slow LED, and I_{bias} is the signal of the bias LED. By taking the derivative of I_{fast} with respect to L_{slow}, it is possible to extract the quantity β as

$$\frac{dI_{\text{fast}}}{dL_{\text{slow}}} = 2\beta L_{\text{fast}}. \tag{5.37}$$

Assuming $L_{\text{fast,slow}} \ll L_{\text{bias}}$ and second-order terms can be ignored,

$$L_{\text{fast}} \approx I_{\text{fast}}/\alpha, \tag{5.38}$$

$$dL_{\text{slow}} \approx dI_{\text{slow}}/\alpha, \tag{5.39}$$

and $L \approx I_{\text{bias}}/\alpha$. It is possible to extract the nonlinearity as

$$\beta = \frac{1}{2} \frac{\alpha dI_{\text{fast}}}{I_{\text{fast}}} \frac{\alpha}{dI_{\text{slow}}}, \tag{5.40}$$

$$x = \frac{\beta L}{\alpha} = \frac{1}{2} \frac{dI_{\text{fast}}/I_{\text{fast}}}{dI_{\text{bias}}/I_{\text{bias}}}. \tag{5.41}$$

In terms of experimentally observable values, this is equivalent to [74]

$$x = \frac{1}{2}\frac{dV_{\text{fast}}}{V_{\text{fast}}}\frac{V_{\text{mean}}}{dV_{\text{mean}}}, \tag{5.42}$$

where $V_{\text{fast/slow}}$ refer the output voltage signal from the PMT from the fast and slow LEDs. The four states the two flashing LEDs can be in are hh, hl, lh, ll which correspond to the PMT signal when the LEDs are at low and high states for the slow and fast LED respectively. This can be used to compute voltage changes as

$$V_{\text{fast}} = \frac{(hh - hl) + (lh - ll)}{2}, \tag{5.43}$$

$$dV_{\text{fast}} = (hh - hl) - (lh - ll), \tag{5.44}$$

$$V_{\text{mean}} = \frac{hh + hl + lh + ll}{4}, \tag{5.45}$$

$$dV_{\text{mean}} = \frac{hh + hl}{2} - \frac{lh + ll}{2}. \tag{5.46}$$

The error on these variables is given as

$$\sigma_{V_{\text{fast}}} = \sigma dV_{\text{fast}}/2, \tag{5.47}$$

$$\sigma_{dV_{\text{fast}}} = \sqrt{\sigma_{hh}^2 + \sigma_{hl}^2 + \sigma_{lh}^2 + \sigma_{ll}^2}, \tag{5.48}$$

$$\sigma_{V_{\text{mean}}} = \sigma dV_{\text{fast}}/4, \tag{5.49}$$

$$\sigma_{dV_{\text{mean}}} = \sigma dV_{\text{fast}}/2. \tag{5.50}$$

Since the dominant term here is the error on $\sigma_{dV_{\text{fast}}}$, the error on nonlinearity was approximated as

$$\sigma_x \approx \frac{1}{2}\frac{\sigma_{dV_{\text{fast}}}}{V_{\text{fast}}}\frac{V_{\text{mean}}}{dV_{\text{mean}}}. \tag{5.51}$$

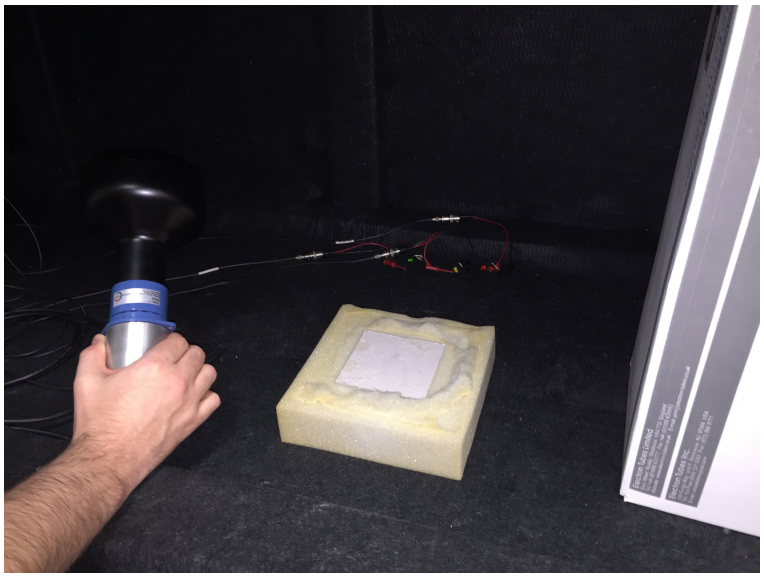

Figure 5.15: The dark box with LEDs and PMT used in the nonlinearity measurement.

Previous attempts had been made to do a bench measurement of the main detector electronics chain nonlinearity [74]. Previous measurements used the same test DAQ stand, however for older measurements, the fast LED signal and the DAQ trigger used two different sources. This led to a very complex analysis and several problems. With the help of DAQ experts, it was eventually possible to trigger the DAQ using the same signal generator driving the fast LED.

A variety of beam currents (and thus PMT voltage signals) were used throughout the running of Q_{weak} including differences between run 1 and run 2 as well as the various ancillary measurements made. For this reason, scans were made of nonlinearities between 1 V and

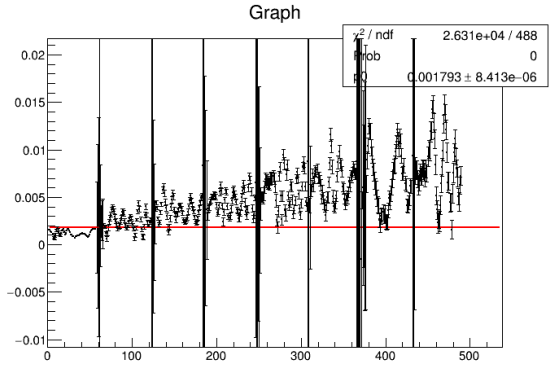

(a) 800V tube voltage signal scan using commensurate frequencies

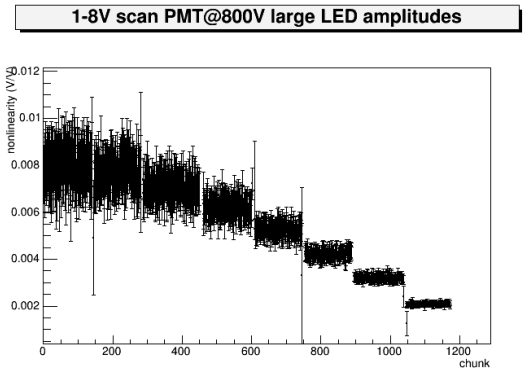

(b) 800V tube voltage signal scan using incommensurate frequencies.

Figure 5.16: Commensurate and incommensurate frequencies in a signal voltage scan. This figure shows nonlinearity versus time. Ever 5 minutes, the bias voltage was changed from 1 V to 8 V. PMT gain set to 800V.

8 V signals, allowing arbitrary signal voltage nonlinearities to be interpolated. In previous studies, an issue was reported where commensurate frequencies (i.e. one frequency is divisible by the other) caused non-statistical fluctuations in measured nonlinearities [74]. Using the newest setup, non-statistical fluctuations was also noticed, as shown in figure 5.16a. Here, $f_{\text{fast}} = 250$ Hz and $f_{\text{slow}} = 10$ Hz where $f_{\text{fast/slow}}$ is the frequency of the fast and slow LEDs. When using incommensurate frequencies of $f_{\text{fast}} = 249.8754$ Hz and $f_{\text{slow}} = 11.2345$ Hz, these issues disappear completely, as see in in figure 5.16b. The reason for this discrepancy is not fully understood, but since using indivisible frequencies fixes the issue, that was the method used going forward.

Signal voltage scans from 1-8 V were conducted for a variety of PMT high voltage settings. The gain of the PMTs is directly related to their high voltage. The main detector PMTs were designed to be run at 1000 V but after the addition of the lead preradiators (which

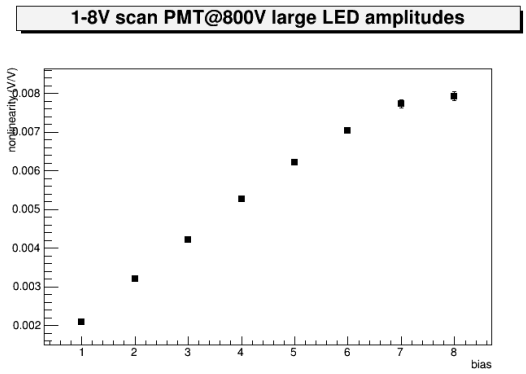

(a) 800V nonlinearity scan from 1-8 V

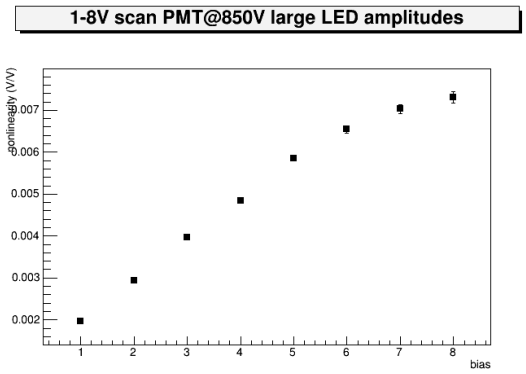

(b) 850V nonlinearity scan from 1-8 V

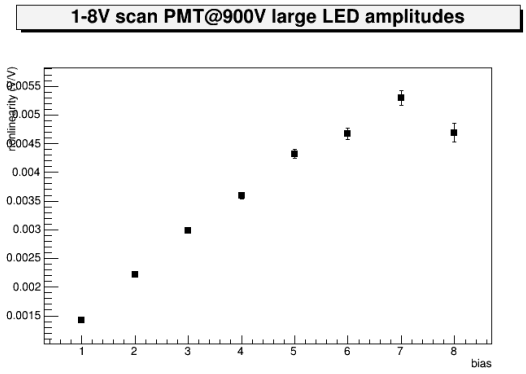

(c) 900V nonlinearity scan from 1-8 V

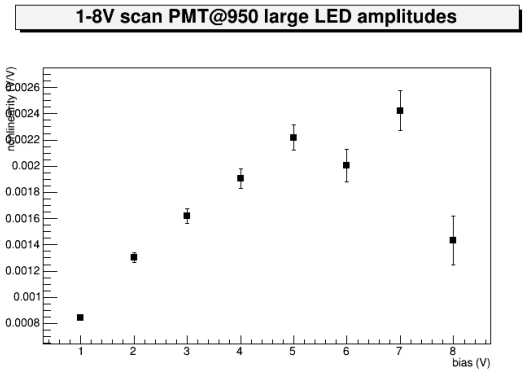

(d) 950V nonlinearity scan from 1-8 V

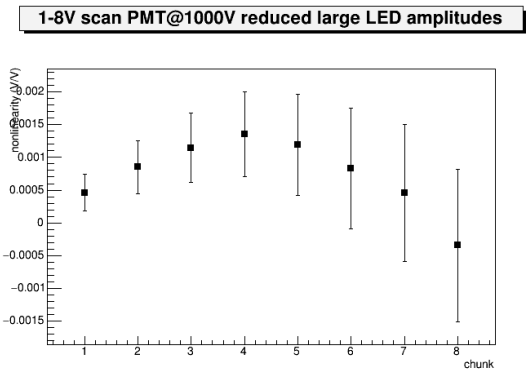

(e) 1000V nonlinearity scan from 1-8 V

Figure 5.17: Nonlinearity scans over a variety of tube high voltage settings. Nominally, Q_{weak} ran with ∼6.2 V signal and 800 V PMT voltage.

increased the number of electrons), the PMT voltage was reduced to 800 V. The results of the scans can be see in figure 5.17. It is possible to see some saturation effects at the higher signal voltages, especially at higher PMT voltages.

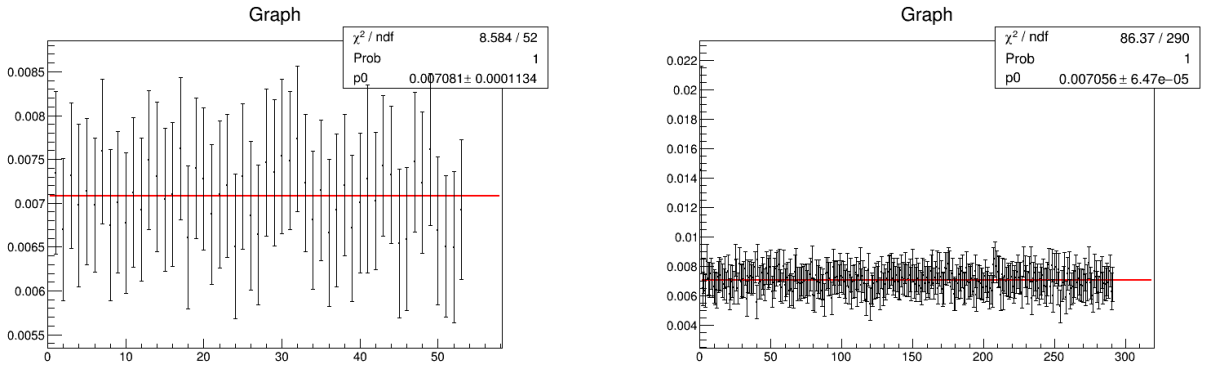

(a) Nonlinearity measurement at 125 Hz

(b) Nonlinearity measurement at 1000 Hz

Figure 5.18: Nonlinearity versus time taken at both 125 Hz and 1000 Hz. Both measurements show a nonlinearity of 0.71%.

In order to understand sources of systematic errors, several other studies were conducted. The measurements in figure 5.17 were done with $f_{\text{fast}} = 249.8754$ Hz, but the fast helicity reversal in Q_{weak} was $f_{\text{helicity}} = 960$ Hz. In order to verify that the nonlinearity did not depend upon f_{fast}, two separate nonlinearity measurements were made at 125 Hz and 1000 Hz, shown in figure 5.18. Both measurements showed no sensitivity to f_{fast}, giving the nonlinearity as 0.71%.

In equation 5.40 and equation 5.41, the assumption is made that $L_{\text{fast,slow}} \ll L_{\text{bias}}$. Generally $V_{\text{fast}} = 0.6$ V and $V_{\text{slow}} = 1.0$ V, since it allowed for nonlinearities to be determined on the timescale of 1 hour. In order to understand how sensitive the experiment was to the assumption that $0.6 \ll 6$, several long runs were conducted with a variety of very small V_{fast}

Table 5.4: A variety of nonlinearity measruements with varying V_{fast} and V_{slow} to understand sensitivity to assumptions.

V_{fast} (V)	V_{slow} (V)	V_{bias} (V)	Nonlinearity (%)
0.643	0.943	6.7	0.698 ± 0.0081
0.325	0.943	6.5	0.706 ± 0.0154
0.167	0.943	6.5	0.666 ± 0.0295
0.123	0.943	6.5	0.684 ± 0.0405
0.307	0.451	6.3	0.695 ± 0.0322
0.152	0.225	6.1	0.746 ± 0.1234
0.021	0.148	6.2	1.715 ± 0.0976
0.040	0.148	6.1	1.222 ± 0.0556

and V_{fast}. The voltages used, as well as the resulting nonlinearity are shown in table 5.4. Good agreement within errors was observed between $V_{\text{fast}} \approx 0.65 - 0.15$ V and $V_{\text{slow}} \approx 0.95 - 0.2$ V, but for the very low V_{fast} runs, very large deviations of $\sim$1% were observed.

The result from the low V_{fast} are thought to be an experimental error and not a true nonlinearity. The primary reasoning behind this is the nonlinearity extracted using regression plus a background correction. The results from equations 5.28 and 5.29 contain both the detector nonlinearity and the BCM nonlinearity. If one then assumes that the low V_{fast} of 1.715 ± 0.0976 V, and using the second part of equation 5.26 with the run 2 regression result in equation 5.29, the implied BCM nonlinearity would be 0.9 ± 0.07 %. However, it is known that the BCM nonlinearity is $< 0.3\%$ [72].

Several attempts were made to find a source for this discrepancy, however, nothing obvious was found and it was determined that time was better spent reducing other errors. Because of the issue with low V_{fast}, a large systematic error was applied. Since the hardware did not change between run 1 and run 2, the run 1 and run 2 values are the same and determined

to be [88]

$$A_L = 0.7 \pm 0.5\ \%. \tag{5.52}$$

For the aluminum data taken during run 2, the nonlinearity was determined to be

$$A_{L_{\mathrm{Al}}} = 0.1 \pm 0.5\ \%. \tag{5.53}$$

In order to produce a final correction, A_{raw} and the blinding factor can be combined to find the nonlinearity correction in ppb as

$$\text{run 1: } A_L = 1.35 \pm 0.96 \text{ ppb}, \tag{5.54}$$

$$\text{run 2: } A_L = 1.19 \pm 0.85 \text{ ppb}, \tag{5.55}$$

where the errors are systematic.

5.3.5 Transverse leakage

Transversely polarized electrons scattering off protons have a parity-conserving transverse asymmetry. In a perfectly symmetric detector, this effect would cancel. Despite strong radial symmetry which reduces transverse leakage, it was necessary to measure the transverse leakage. In order to do this, both the magnitude of the residual transverse polarization as well as the symmetry breaking factor needed to be measured [94, 95]. The residual transverse polarization could be determined by looking at computed main detector dipoles and sinusoidal fits

of dither corrected main detector asymmetries versus octant. The symmetry breaking factor could be determined from the results of fully transverse running as well as using simulation with survey data. In order to make error propagation simpler, no correction was made for transverse leakage, and only an error was applied. Work done by B. Waidyawansa, P. Zang, and P. King determined the final result to be [63]

$$\text{run 1: } A_T = 0 \pm 1.10 \text{ ppb}, \tag{5.56}$$

$$\text{run 2: } A_T = 0 \pm 0.68 \text{ ppb}, \tag{5.57}$$

where the errors are systematic.

5.3.6 Rescattering bias effect in lead preradiators

In parity experiments such as Q_{weak}, a lot of work goes into error budgeting and managing systematic effects before the experiments are even approved. However, since these experiments push the limits of precision, there is the possibility that systematic errors are discovered during or after the experiment. This was the case with the so-called rescattering bias effect; it was only discovered after the experiment finished taking data.

Due to low energy beamline backgrounds, lead preradiators were installed on all eight main detectors (see section 3.6). As the longitudinally polarized scattered electrons pass through the QTor magnetic field (see section 3.5), they precess and become ∼50% transversely polarized [12]. When the electrons enter the lead preradiator and shower, the lead has a parity

conserving left-right asymmetry, leading to a large asymmetry difference (sometimes referred to as a double difference) between left and right tubes.

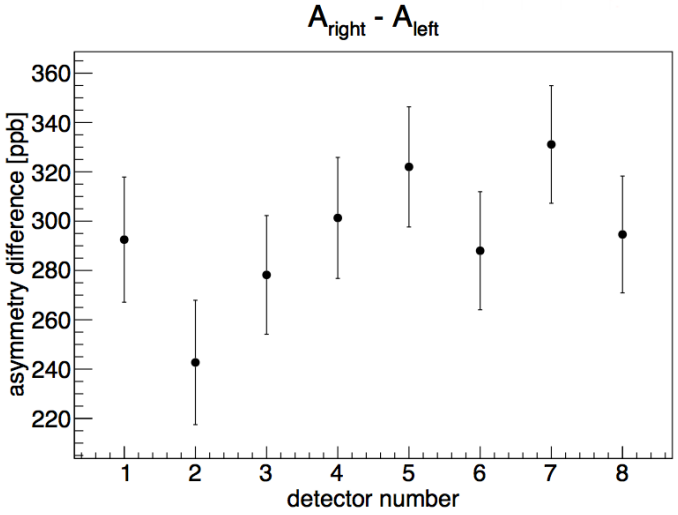

Figure 5.19: A_{DD} vs main detector bar number for the entire Q_{weak} running period.

In Q_{weak}, the difference was defined as

$$A_{DD} = A_{-} - A_{+}, \tag{5.58}$$

where $A_{+/-}$ is the asymmetry seen by the positive and negative PMTs (see figure 3.16 for tube labeling). Since all 16 tubes were averaged together, this effect will cancel to first order. However, since the main detector bars are imperfect and thus have broken symmetry, there will be imperfect cancellation resulting in a bias (similar to how transverse leakage affects the experiment). This apparent asymmetry is referred to as A_{bias}. The value of A_{DD} was very stable throughout both run 1 and run 2 and between different main detector bars. Using both run 1 and run 2, and averaging the value of all 8 detectors together, $A_{DD} = 293 \pm 6$ ppb

[108]. However, the important number is how much false asymmetry comes from symmetry breaking, referred to as A_{bias}.

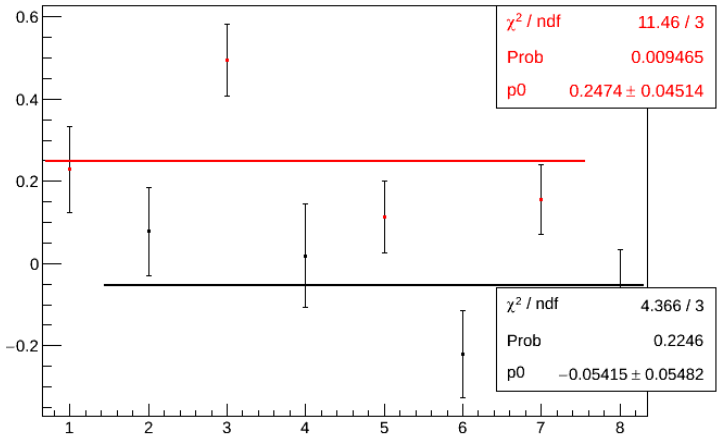

Figure 5.20: A_{DD} versus main detector bar number during the 4 by 4 running period [31]. Here only the odd bars (red) had lead preradiators installed.

In order to confirm that the lead preradiator was responsible for the observed difference, the 4 by 4 dataset, previously used in section 5.3.4 to study the effects of beamline background on charge slope, was used. Here, odd numbered bars had lead preradiators installed, and even bars did not. As such, the odd bars should show a large A_{DD} and the even bars should show none. The result was obtained by calculating the A_{DD} for each tube individually, and then averaging the even and odd bars together. The results show that

$$A_{\mathrm{DD}}^{\mathrm{ODD}} = 240 \pm 61 \text{ ppb}, \tag{5.59}$$

$$A_{\mathrm{DD}}^{\mathrm{EVEN}} = -72 \pm 61 \text{ ppb}, \tag{5.60}$$

where the errors are systematic. This is in very good agreement with the model that the lead preradiators are causing the observed effect. Figure 5.20 shows A_{DD} for each main detector bar.

Since this effect was discovered well after the Q_{weak} apparatus was disassembled, a strategy was developed to assign a correction and error for A_{bias}. Two separate but equally important simulation efforts were undertaken to understand different aspects of the problem. One studied the physics causing this effect to make sure it was well understood, and another studied which bar defects contributed the most to the false asymmetry.

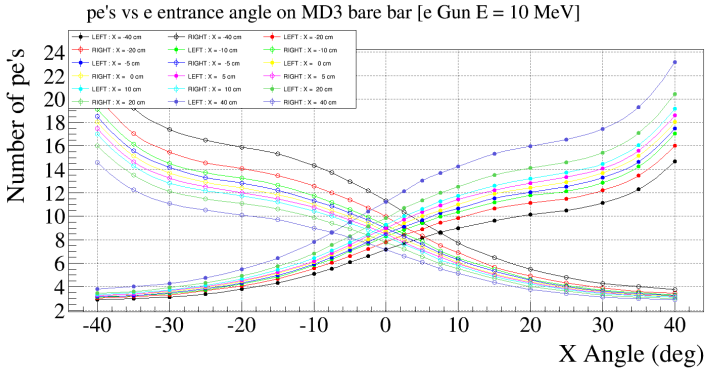

Figure 5.21: Light parameterization [93] which relates angle of incoming electrons to the number of photoelectrons produced for a given energy.

In order to reduce the amount of CPU time needed for simulations, lookup tables were developed to handle optical photon propagation, since this is one of the most computationally expensive parts of the simulation. These lookup tables, referred to as light parameterizations, were generated using a modified version of the standard Q_{weak} Geant4 software. The electron gun was moved in front of MD3 (arbitrarily chosen) between the lead preradiator and the bar [93]. To simulate the fact that electrons hit the main detector bar at an angle of 22.2° , the bar

was tilted in simulation. Simulations were then run with varying beam energy, position of the electron gun in X (i.e. the short, radial axis of the bar), and primary electron entrance angle. Using these simulations, a 4-D lookup table was created which, for a given electron energy, position, and angle, the number of photoelectrons in the PMT could be obtained. A rendering of a light parameterization at fixed energy is shown in figure 5.22. Interpolation was then used to get the number of photoelectrons at arbitrary position, angle and energy. A study was also done of the Y position and angle and it was determined to be a negligible effect for the purposes of this study [81].

Initially, light parameterizations were made of the perfect, ideal main detector bars. Eventually, many light parameterizations were made for ideal bars with defects as well as parameterizations to mimic physical bars. The light parameterizations can be thought of as containing the geometry of the bar. Ideal bars with defects were used to figure out which physical defects had the largest effect on A_{bias}, and then measurements were made of the physical bars. Then, the light responses were matched with light responses of tracking by changing various parameters [57]. Realistic models of all 8 main detector bars were created.

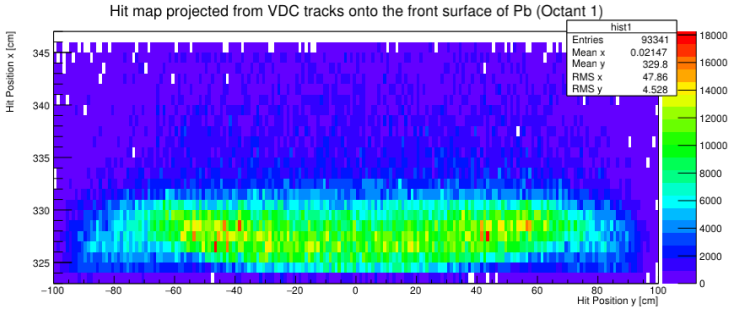

Figure 5.22: MD1 simulated hit map [82].

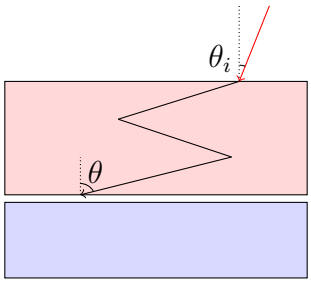

Figure 5.23: Red is primary electron, black is scattering in the lead. Picture assumes only two scatterings in lead but more may occur in simulation. Scatterings exaggerated here for clarity.

In order to use the light parameterizations, maps of where the electrons hit the face of the lead were also generated. Initially, tracking data was used, however, due to efficiency issues in the tracking system, non-physical biases and double differences occurred. For this reason, simulated hit maps were used. Most of the octant to octant variation in the hit map comes from variations in the QTor magnetic field. The field map in the Q_{weak} Geant4 simulation does not have real world data, but the variations in this map are though to be of the same size as real world variations. The use of hit maps prevented the simulation from having to propagate each electron through the magnetic field, saving CPU time.

The final simulation step was to propagate the electrons through the lead. Both simulations handled the physics differently, but produced a final hit map containing the initial positions and angles on the face of the lead and the final positions and angles as they leave the lead. This was then combined with the light parameterizations to generate photoelectrons in each PMT, from which simulated A_{DD} and A_{bias} could be generated.

The first simulation implemented was called the effective model. This simulation was primarily used to quickly study differences between light parameterizations. Electrons were

propagated through the lead using standard Geant4 physics to account for the distortions of the electrons when they shower in the lead. The asymmetry was then calculated based upon the difference between the initial scattering angle of the electron and the final angle of the electron. Based on figure 5.23, this would be

$$\theta_{shower} = \theta - \theta_i. \tag{5.61}$$

The asymmetry then uses one of the six forms given in table 5.5 and shown in figure 5.24, where the asymmetry depends only on θ_{shower}. A scaling factor, also listed in table 5.5, was applied such that the A_{DD} produced by these effective models matched experimental observations. No physics is contained in these models, however they were designed to mimic the effects of actual physics, which is why they depend upon θ_{shower}. Finally, several other types of effective model were implemented which relied purely on the position differences (posdif) across the bar. The position difference model was implemented as an alternate effective model and also proved useful during the error analysis. Some plots may refer to "Greg's position difference model" and the "mackroscopic model", which are both implementations of position difference models.

A much more realistic and advanced Geant4 simulation was also implemented which attempted to reproduce the A_{DD} observed in Q_{weak} and predicted an A_{bias} using actual physics processes. This simulation primarily used two physics processes: 2-γ exchange asymmetry model and Mott scattering [50]. The 2-γ exchange is important for high energy electrons

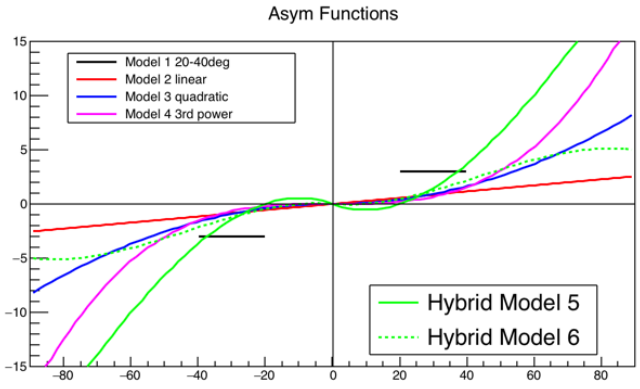

Figure 5.24: Effective models plotted as asymmetry vs $\theta_{scatter}$ [84]. See table 5.5 for functional forms.

while the Mott model is important for the low energy electrons which occur near the end of the shower. The goal of this simulation was to show that there was a good understanding of the physics causing this large observed asymmetry and then to predict an A_{bias} based upon this result.

Table 5.5: Various effective models [84]. Hybrid models have no scaling factor as they are just a combination of other models.

Model	Asymmetry form	Scale factor
Model 1	Constant from 20-40° , 0 otherwise	$0.759 \times 4 \times 10^{-6}$
Model 2	θ_{shower}	$0.713 \times 4 \times 10^{-8}$
Model 3	$\theta^3_{shower}/\lvert\theta_{shower}\rvert$	$0.685 \times 1.5 \times 10^{-9}$
Model 4	θ^3_{shower}	$0.685 \times 1.5 \times 10^{-9}$
Model 5 (hybrid)	$-3.9 \times$ (model 2) $+ 5.8 \times$ (model 3) $- 0.9 \times$ (model 4)	
Model 6 (hybrid)	$-0.9 \times$ (model 2) $+ 2.8 \times$ (model 3) $- 0.9 \times$ (model 4)	

The microscopic model was a very advanced simulation that required implementing significant changes to Geant4. For multiple scattering inside the lead, WentzelVI (for electrons $E > 100$ MeV) and Urban (for electrons $E < 100$ MeV) were modified and added to a special branch of Q_{weak} simulation. In order to add in an asymmetry for 2-photon exchange and

Mott scattering, a track modification of ϕ angles was done after Geant4 had propagated the electrons through the lead using previously mentioned multiple scattering routines. This allowed an arbitrary asymmetry to be added. Another important physics process was depolarization via Bremsstrahlung, which is important for getting the magnitude of the asymmetry correct. Attempts were made to track the spin of the electron as it scattered, however they were unsuccessful. For this simulation, it was assumed the electron spin is fixed in the lab frame [50].

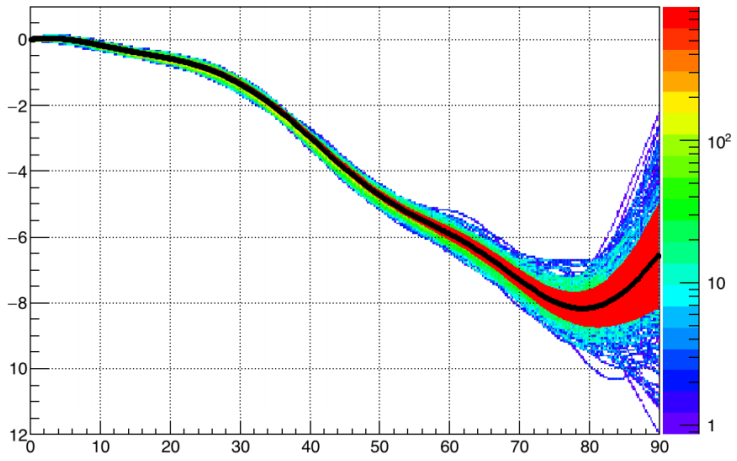

Figure 5.25: Visual representation of the microscopic model generated by GPR [49]. Plotted as asymmetry vs $\theta_{scatter}$.

In order to apply the microscopic model to a variety of different bar models (via light parameterizations discussed above), Gaussian process regression (GPR) was used to take the simulated microscopic model results, sample asymmetry versus θ_{shower}, and produce a smooth functional form with error bands. This was then included as an effective model and quickly run on a variety of different light parameterizations. An example of a functional form derived from GPR is shown in figure 5.25. Two separate GPRs were created and used.

The first, referred to as the central GPR, averages over all energies. The second, referred to as energy dependent GPR, uses energy bins and interpolates between. This is effectively a GPR depending on energy and $\theta_{scatter}$.

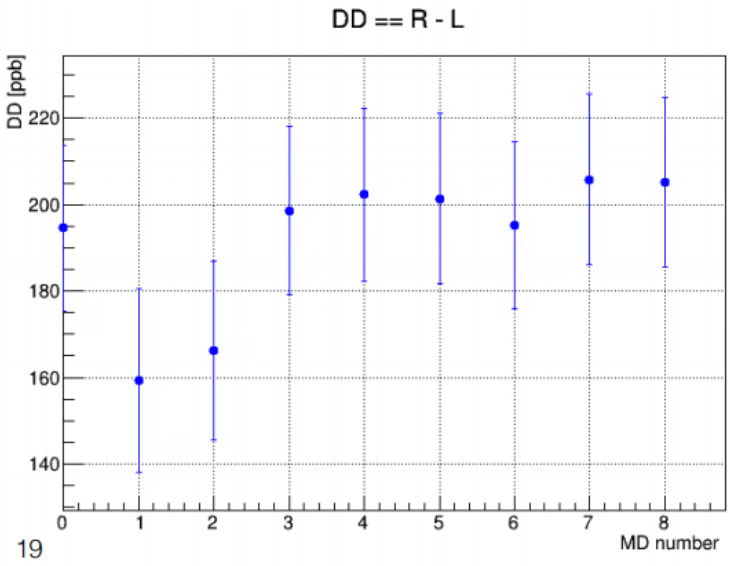

Figure 5.26: A_{DD} versus main detector number as simulated using the microscopic model (i.e. realistic physics models). [50]. Compare to figure 5.19.

The microscopic model predictions of the PMTDD were $\sim$ 200 ppb, versus the observed $\sim$ 300 ppb. Exact simulated values for each main detector can be seen in figure 5.26. However, it does correctly predicted the sign and correct order of magnitude of the effect. Since the simulation makes some assumptions about the spin of the electron as it passes through the lead, perfect agreement with data is not expected. Still, this increases the error slightly by requiring some model dependent uncertainty.

In order to develop accurate optical models, both a simulation effort as well as physical measurements of the bars was necessary. To understand the effects a single defect would have on symmetry breaking, ten ideal models were created. One was a perfect bar (any

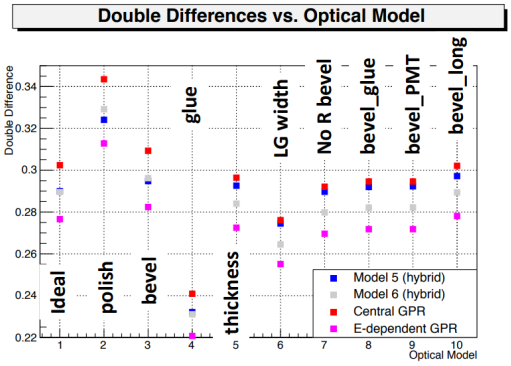

(a) Simulated A_{DD} versus ideal optical model number.

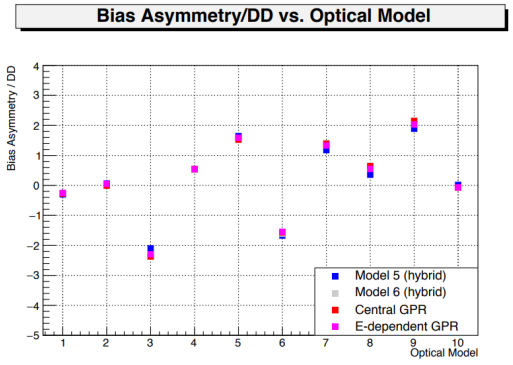

(b) Simulated A_{bias} versus ideal optical model number.

Figure 5.27: Simulated A_{DD} and A_{bias} vs ideal optical model. Only model 1 (const Asym), hybrid models, and GPR are shown.

symmetry breaking here is a good estimate of asymmetry in the image on the bar), and the rest included left-right differences in the polish, bevel, glue joint, thickness of the bar, light guide width, and PMT bevel. Figure 5.27 shows the effect of each defect on A_{DD} and A_{bias}. This helped guide physical measurements to the bevel differences, bar thickness differences, and light guide bevel.

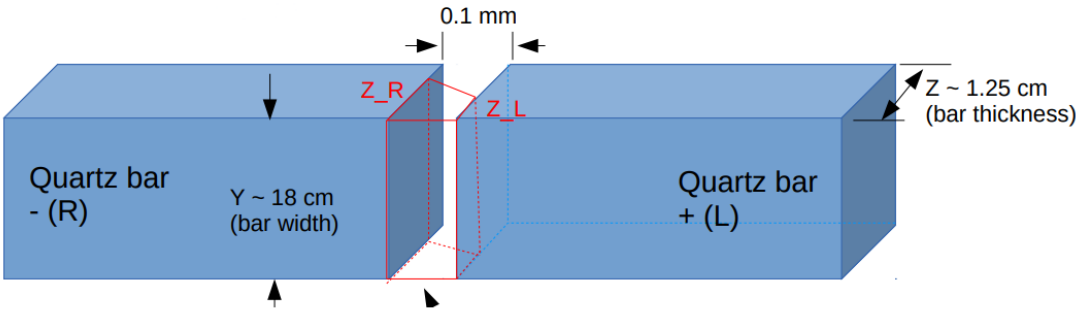

Figure 5.28: Drawing of how broken glue joints in MD1 and MD2 were modeled. [50].

Realistic optical models were created using a combination of measuring physical parameters on bars, plus changing several other simulation parameters until good agreement with the

light curves from tracking data was achieved. One issue that complicated this was MD1 and MD2 had a damaged glue joint (probably from mechanical stress). In order to model this, the broken joint was modeled as half air, half glue, with a gradual change between glue and air as shown in figure 5.28. In some cases, several iterations of an optical model for a bar were done before satisfactory agreement was achieved. Due to logistical issues (main detector bars were still radioactive and difficult to access without specialized help), it was not possible to measure every main detector bar. For this reason, work was focused on main detectors with broken glue joints and poor agreement with tracking. MD1 and MD8 were the only bars to have their bevels measured. All 8 bars had the thickness difference measured.

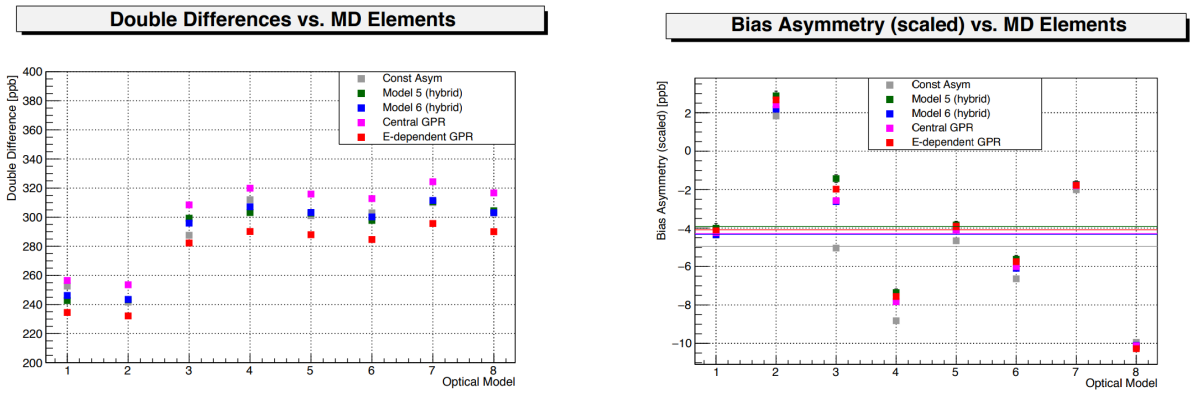

(a) Simulated A_{DD} versus physical optical model number.

(b) Simulated $-1 \times A_{bias}$ versus physical optical model number.

Figure 5.29: Simulated A_{DD} and A_{bias} vs physical optical model. Only hybrid models and GPR are shown.

Figure 5.29 shows A_{DD} and A_{bias} for all eight physical models. Surprisingly good agreement is shown between model 1 (constant asymmetry), the hybrid models, and the GPR models. This is despite the fact that the constant asymmetry model is known to be completely wrong and does not represent expected physics based upon simulation. Previous studies with ideal

light parameterizations combined with this seem to indicate that geometric models are the biggest factor in determining A_{bias}.

Using the GPR result shown in figure 5.29b, it is possible to obtain A_{bias}. The GPR effective model was selected because it represents an actual simulation of the physics processes. Assigning a systematic error to this correction was done in two parts. First, some error had to be assigned for the optical models imperfections. A second error was applied based on the spread of effective models since the microscopic model was not perfect.

The optical model error was broken down into two parts. The first part was a moment study using the position difference from the effective model [50]. The sensitivities were obtained using the ideal bar models with defects. Then, using position differences from tracking, a moment analysis was conducted over the three most important moments: polish, bevel, and light guide. In the case of MD1 and MD8 where the bevels were measured, the bevel moment was excluded. The implied A_{bias} from this analysis averaged over all bars is

$$A_{bias}^{\text{polish}} = -1.2 \text{ ppb}, \tag{5.62}$$

$$A_{bias}^{\text{bevel}} = 3.0 \text{ ppb}, \tag{5.63}$$

$$A_{bias}^{\text{light guide}} = 1.9 \text{ ppb}. \tag{5.64}$$

This implies a total error of 2.3 ppb. The second part of the uncertainty was assigned for model variation in the glue joint. For the broken glue joints, a conservative error of 6 ppb was assigned based on the fluctuations between various glue joint models. For normal glue

joints, an error was applied. This gives a total glue joint error of 1.5 ppb and a total optical model error of 2.7 ppb. Finally, a systematic error was also applied for the variation between various effective models of 1.5 ppb.

Combining the result from the GPR effective model and the above error analysis, a correction for symmetry breaking in the detector can be given as

$$A_{bias} = 4.3 \pm 3.0 \text{ ppb.} \tag{5.65}$$

Given a lot more time and simulation work, it might have been possible to reduce the error on this value, but the effect on the overall Q_{weak} error would be minimal.

5.3.7 Blinding factor

Like many precision tests of theoretical models, Q_{weak} employed a blinding factor. This was done so that it was not possible to introduce any bias in any corrections. Q_{weak} used three different blinding factors, one for the commissioning data which was published separately, one for run 1, and one for run 2. This was done in case, for whatever reason, the decision was made to unblind run 1 and run 2 at different times. This was not deemed necessary and both runs were unblinded at the same time.

Care had to be given on how the blinding was implemented. Blinding was done by combining a randomly selected blinding factor with the asymmetry during analysis. The random factor was confined to a blinding box of ± 60 ppb [64]. To prevent leaking of the blinding factor, the

analyser would only apply this factor to production runs where the LH_2 target was within normal parameters. The blinding factor was also reversed with the IHWP and wien slow helicity reversals. The analyser also checked to make sure the wien filter was not providing transverse polarization, as this would leak the blinding factor. These checks were done by checking various values included in the data by the analyser.

In order to unblind the data, the blinding factor is treated as a false asymmetry. The blinding factors were

$$\text{run 1: } A_{\text{blind}} = 25.34 \text{ ppb}, \tag{5.66}$$

$$\text{run 2: } A_{\text{blind}} = 6.669 \text{ ppb}. \tag{5.67}$$

These were extracted by comparing several runs with the blinder disabled to runs with the blinder enabled. Since these values are set in software, there is no associated error.

5.3.8 Final A_{msr}

With all these pieces in place, it is now possible to calculate A_{msr} using equations 5.6 and the values in previous sections. The final measured asymmetry with all false asymmetries

removed is [11]

$$\text{run 1: } A_{\text{msr}} = -165.6 \pm 13.2 \text{ (stat.)} \pm 8.2 \text{ (sys.) ppb}, \tag{5.68}$$

$$\text{run 2: } A_{\text{msr}} = -167.5 \pm 7.3 \text{ (stat.)} \pm 4.1 \text{ (sys.) ppb}. \tag{5.69}$$

There is very good agreement between run 1 and run 2, despite the large difference in helicity-correlated beam motion correction between runs.

5.4 Extracting the parity-violating asymmetry

At this point, all false asymmetries have been corrected. However, there are still several physics processes present and other considerations to be made before using the Q_{weak} measured asymmetry to extract Q_w^p. The final parity violating asymmetry can be determined using [11]

$$A_{\text{ep}} = R_{\text{tot}} \frac{A_{\text{msr}}/P - \sum_{i=1,3,4} f_i A_i}{1 - \sum_{i=1}^{4} f_i}, \tag{5.70}$$

where

$$R_{\text{tot}} = R_{\text{RC}} R_{\text{Det}} R_{\text{Acc}} R_{Q^2}, \tag{5.71}$$

P is the beam polarization, f_i and A_i are various background physics processes dilution fractions and asymmetries, and R_{tot} is the total radiative and kinematic correction factor. Once A_{ep} is extracted, it can be applied to equation 5.70 to extract Q_w^p. Short descriptions and relevant sections for these variables can be found in table 5.6.

Table 5.6: Physics backgrounds and effects, descriptions, and sections which cover them.

Physics effect	Description	Section
R_{RC}	Electromagnetic radiative correction	5.4.1
R_{Det}	Detector response correction	5.4.1
R_{Acc}	Finite acceptance correction	5.4.1
R_{Q^2}	Q^2 scaling and error	5.4.1
P	Polarization correction	5.4.2
f_1	Aluminum background dilution	5.4.3
A_1	Aluminum background asymmetry	5.4.3
f_2	Beamline background dilution	5.4.3
f_3	Neutral beamline background dilution	5.4.3
A_3	Neutral beamline background asymmetry	5.4.3
f_4	$N \rightarrow \Delta$ dilution	5.4.3
A_4	$N \rightarrow \Delta$ asymmetry	5.4.3

5.4.1 Radiative and kinematic correction

The radiative and kinematic corrections were determined through a combination of simulation and the tracking apparatus. R_{RC} is the total electromagnetic radiative correction from the bremsstrahlung of incident electrons [11]. Bremsstrahlung can cause the electron to lose energy, thus changing the momentum transfer. It can also depolarize the electron before scattering. R_{RC} was determined using a GEANT3 simulation by comparing the Q^2 result with and without bremsstrahlung [91] and was simulated to be

$$R_{\mathrm{RC}} = 1.010 \pm 0.005. \tag{5.72}$$

Because the main detector response varies over the entire bar, and due to the magnetic optics of the Q_{weak} spectrometer, Q^2 will be correlated with main detector bar response [11],

causing the asymmetry to be correlated with detector response. The tracking system was used to measure the correlation between detector response and Q^2. R_{Det} is a correction for this and was measured to be determined to be

$$R_{\mathrm{Det}} = 0.9895 \pm 0.0021. \tag{5.73}$$

R_{Acc} is another correction factor coming from finite acceptance of the spectrometer. Since Q_{weak} has a finite acceptance, A_{msr} represents an average over a range Q^2 [11]. R_{Acc} corrects the asymmetry to reflect the asymmetry that would come from scattering at the average Q^2. This was calculated using simulation to be

$$R_{\mathrm{Acc}} = 0.977 \pm 0.002. \tag{5.74}$$

The final correction comes from the fact that Q^2 changed between run 1 and run 2. Run 2 was chosen as the reference run, and run 1 was scaled to match [11]. To make global fitting simpler, Q^2 is taken to be known perfectly, and the error from Q^2 is included as the error bar here. This is not an error from the scaling. The Q^2 values were determined using simulation which was benchmarked using experimental data from the tracking apparatus. The scaling

factor was determined to be [19]

$$\text{run 1: } R_{Q^2} = 0.9928 \pm 0.0055, \tag{5.75}$$

$$\text{run 2: } R_{Q^2} = 1.0000 \pm 0.0055. \tag{5.76}$$

5.4.2 Polarization result

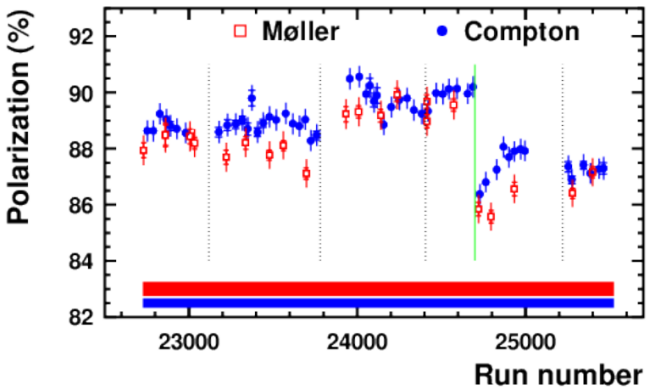

Figure 5.30: Beam polarization over run 2 showing Møller and Compton data together. Red squares are the Møller data points and blue circles are the Compton data points. Error bars show the statistical errors, and the additional systematic errors are show by the red and blue bands. Vertical lines correspond to changes in the injector.

Shown in figure 5.30 are the polarization data taken with both the Møller and Compton polarimeters (see section 3.2) during run 2. Good systematic agreement is seen between the two methods used [8, 80]. All the data points are consistent, even between the Møller and

Compton. The final values for beam polarization are [51]

$$\text{run 1: } P = 87.7 \pm 1.1\ \%, \tag{5.77}$$

$$\text{run 2: } P = 88.7 \pm 0.6\ \%. \tag{5.78}$$

The final parity-violating asymmetry will depend on accurately knowing the polarization, so the ability to know the polarization to less than 1% was a key goal in the design phase.

5.4.3 Physics backgrounds

Table 5.7: Physics background asymmetries and their dilutions [11].

Quantity	Run 1	Run 2
f_1	2.471 ± 0.056 %	2.516 ± 0.059 %
A_1	1.514 ± 0.077 ppm	1.515 ± 0.077 ppm
f_2	0.193 ± 0.064 %	0.193 ± 0.064 %
f_3	0.12 ± 0.20 %	0.06 ± 0.12 %
A_3	-0.39 ± 0.16 ppm	-0.39 ± 0.16 ppm
f_4	0.018 ± 0.004 %	0.018 ± 0.004 %
A_4	-3.0 ± 1.0 ppm	-3.0 ± 1.0 ppm

The ability of the Q_{weak} experiment to quantify and remove physics background processes was studied well before the experiment ran [26]. There were four backgrounds, although beamline background is corrected for when extracting A_{msr}. The fractional dilution of the beamline background (b_2) is still important when determining A_{ep}. Thus, beamline background is excluded in the numerator of equation 5.70 but the dilution is included in the denominator. The remaining backgrounds are aluminum window background (b_1), the neutral beamline

background (b_3), and the inelastically scattered electron background (b_4). For results see table 5.7.

Electrons scattering off aluminum nuclei in the target windows (see section 3.3 for details on the aluminum windows) creates the dominant physics background in Q_{weak} [11]. The asymmetry (A_1) was measured using a 4% aluminum target constructed from the same alloy as the target windows. 4% refers to the fact the target is 0.04 radiations lengths thick. Some simulation was required to adjust for the different acceptances of the upstream and downstream windows [20]. The dilution (f_1) was measured using low current data taken with an empty target. These data, combine with simulation of radiative effects, were used to determine the dilution [73]. For results see table 5.7.

The beamline background dilution (f_2) determination has already been discussed in section 5.3.3 and is given in equation 5.11. Another beamline background comes from low energy neutral particles. This primarily comes from secondary scatterings in the collimator and QTor magnet [77]. The asymmetry A_3 was determined using simulation of neutral events in the main detector. The dilution was measured using low current scans at various QTor currents with trigger scintillators (see section 3.8.3 for details) installed. The trigger scintillators will only produce light when interacting with a charged particle whereas the main detector will produce light for any high energy particle. This allowed the trigger scintillators to reject events from charge particles and thus measure the fraction from neutral particles only. Some correction was also applied to remove events from f_2. For results see table 5.7.

While the inelastic $N \to \Delta$ (which occurs when the electron excites the hydrogen nucleus to a Δ) peak occurs at lower energies, some of the radiative tail overlaps the elastic electron-proton peak [11, 65]. Dedicated data was taken on the $N \to \Delta$ peak to measure the asymmetry. This was then scaled up by Q^2 to the elastic asymmetry to give A_4. f_4 was estimated using simulation. For results see table 5.7.

5.4.4 Final $A_{\mathbf{ep}}$

It is now possible to extract the final parity-violating asymmetry arising only from elastic electron-proton scattering using equation 5.70. For run 1 and run 2 individually, this was determined to be

$$\text{run 1: } A_{\text{ep}} = -223.5 \pm 15.0 \text{ (stat.)} \pm 10.1 \text{ (sys.) ppb,} \tag{5.79}$$

$$\text{run 1: } A_{\text{ep}} = -227.2 \pm 8.3 \text{ (stat.)} \pm 5.6 \text{ (sys.) ppb.} \tag{5.80}$$

This shows very good agreement between run 1 and run 2. These can be combined together to give

$$A_{\text{ep}} = -226.5 \pm 7.3 \text{ (stat.)} \pm 5.8 \text{ (sys.) ppb.} \tag{5.81}$$

This includes proper handling of correlated errors between run 1 and run 2.

Chapter 6

Results

With the isolation of A_{ep} in section 5.4.4, it is now possible to apply theoretical results from section 2.4.3 to extract physical quantities like Q_w^p and $\sin^2\theta_W$. These quantities can then be compared to theoretical predictions.

6.1 Extracting the weak charge of the proton

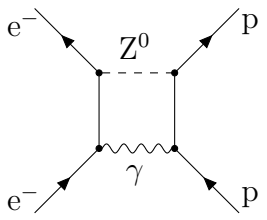

Figure 6.1: Feynman diagram for the electroweak radiative correction $\Box_{\gamma Z}$. (TikZ [92] courtesy of J.C. Cornejo.)

In order to extract Q_w^p, a global fit analysis of the world's parity-violating electron-scattering (PVES) data is made. From before,

$$\frac{A_{ep}^{PV}}{A_0} = Q_w^p + Q^2 B(Q^2, \theta). \tag{6.1}$$

is used for the global fit. The world PVES data helps to determine the hadronic term $B(Q^2, \theta)$. Before this could be done, corrections for electroweak radiative correction $\Box_{\gamma Z}$ had to be made. The Feynman diagram for this effect is shown in figure 6.1. This correction depends on Q^2 and θ. A description of how this correction was made can be found in the preliminary Q_{weak} paper [10]. This correction had to be made for every asymmetry used in the global fit. At the Q_{weak} kinematics, this effect was a 0.00459 ± 0.00044 correction to Q_w^p [48].

The global fit analysis procedure was conducted after making radiative corrections. The procedure used is fully described in a previous publication [102]. The fit was a 3 dimensional fit over Q^2 and θ and had five free parameters: the neutral weak quark coupling constants (see section 2.4.3 for details) C_{1u} and C_{1d}, the strange charge radius ρ_s, the magnetic moment μ_s, and the isovector weak axial form factor $G_A^{Z(T=1)}$. In order to visualize this fit in two dimensions, the result is rotated into the forward angle ($\theta = 0$). The projection is done using [71] using

$$A_{\text{ep}}^{\text{data}}(\theta = 0, Q^2) = A_{\text{ep}}^{\text{data}}(\theta, Q^2) - \left[A^{fit}(\theta, Q^2) - A^{fit}(0, Q^2)\right], \tag{6.2}$$

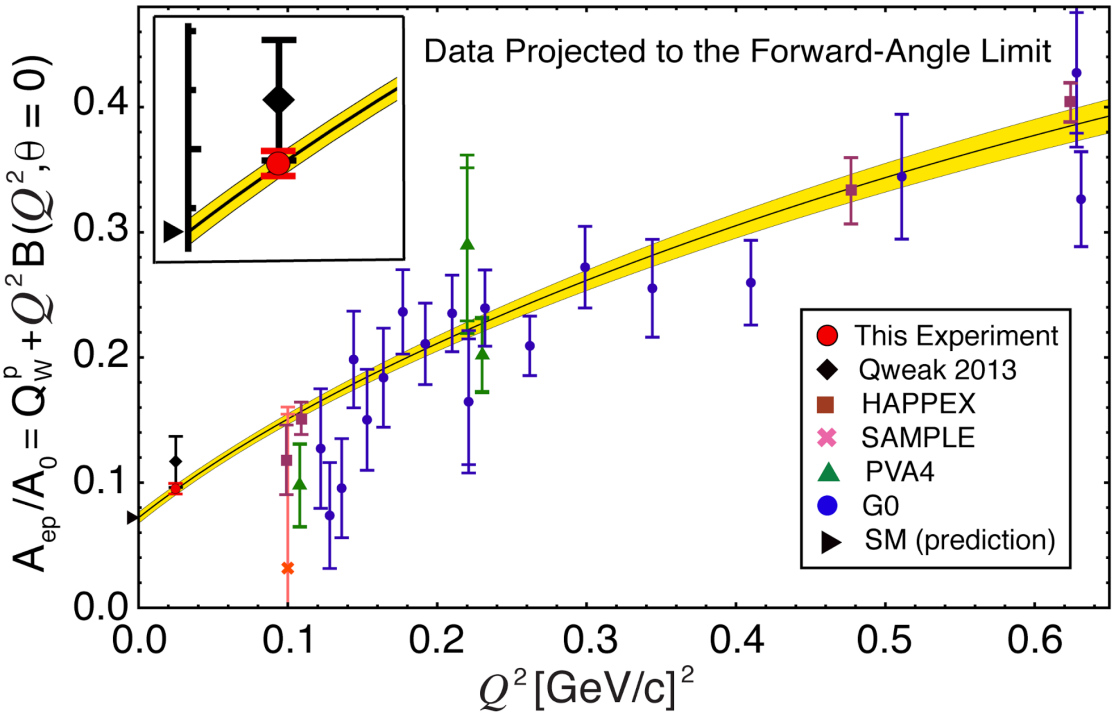

Figure 6.2: Global fit of world PVES data projected into $\theta = 0$ forward angle [11]. All points on this plot of been corrected for the $\Box_{\gamma Z}$. The black line represents fit and the yellow band represents the uncertainty. The arrow at $Q^2 = 0$ represents the Standard Model predicted value for Q_w^p. The inset shows the final Q_{weak} data point in red and the commissioning data point in black [10].

where $A_{\text{ep}}^{\text{data}}(\theta, Q^2)$ refers to measured asymmetry from data at θ and Q^2 and $A^{\text{fit}}(\theta, Q^2)$ refers to the asymmetry as calculated by the fit at θ and Q^2. The forward angle fit can be seen in figure 6.2. This fit uses the world PVES data [4, 7, 9, 13, 14, 15, 18, 21, 56, 69, 70, 90] on hydrogen, deuterium and helium. By calculating $A^{fit}(0,0)$, Q_w^pcan be extracted to be [11]

$$Q_w^p(PVES) = 0.0719 \pm 0.0045. \tag{6.3}$$

If the lattice QCD (LQCD) value for the strange form factor is taken over measured values (the LQCD strange form factor has a much higher precision than the experimentally mea-

sured strange form factor) [53] then the weak charge becomes

$$Q_w^p(PVES + LQCD) = 0.0684 \pm 0.0039, \tag{6.4}$$

which has an improvement in error. These values can be compared to the Standard Model predicted valued of [85]

$$Q_w^p(SM) = 0.0708 \pm 0.0003. \tag{6.5}$$

This shows very good agreement with the Standard Model predicted value of Q_w^p.

6.2 Extracting the weak coupling constants and neutron weak charge

By combining PVES data with APV data it is also possible to determine the neutral weak quark couplings and the neutron weak charge. Since PVES and APV provide nearly orthogonal constraints to the isovector and isoscalar combinations (see section 2.4.3), it is possible to extract individual values of C_{1u} and C_{1d}. Using the measurements of the weak charge of ^{133}Cs [99] with atomic corrections [45], it is possible to extract the quark neutral weak

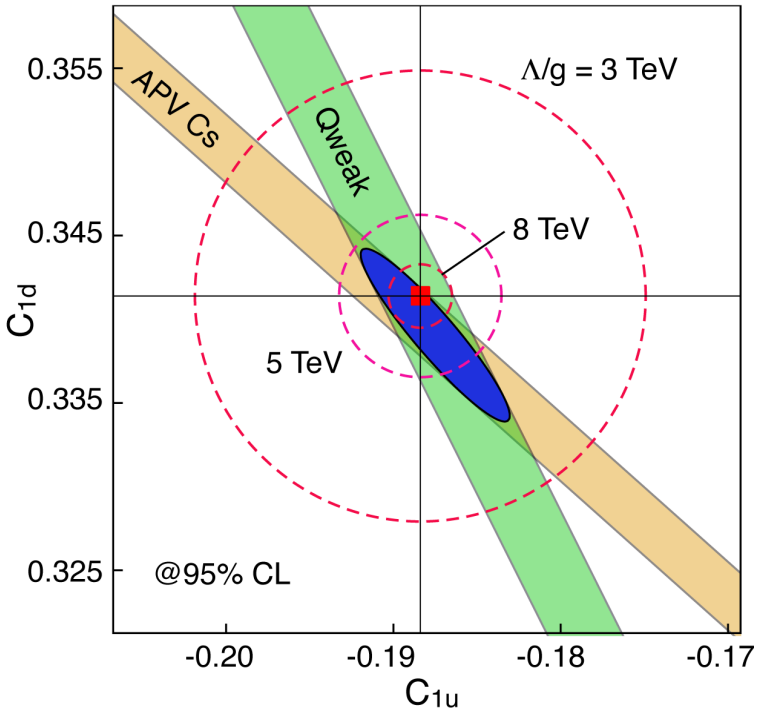

Figure 6.3: Constraints on the quark coupling constants [11]. This plot is computed using $Q_w^p(PVES)$. The green band represents the Q_{weak} constraint (using world PVES data) and the gold band represents the latest ^{133}Cs APV data. The blue ellipse represents the 95% confidence-level constraint using the combination of PVES and APV. The red square represents the Standard Model predicted values of the weak coupling constants and the red contours represent the mass reach Λ/g for couplings to new physics.

coupling constants as

$$C_{1\text{u}} = -0.1874 \pm 0.0022, \tag{6.6}$$

$$C_{1\text{d}} = 0.3389 \pm 0.0025. \tag{6.7}$$

With these values, it is then possible to determine the weak charge of the neutron to be

$$Q_w^n(PVES + APV) = -0.9808 \pm 0.0063. \tag{6.8}$$

This can be compared to the Standard Model predicted value of [85]

$$Q_w^n(SM) = -0.975 \pm 0.0063. \tag{6.9}$$

Again, there is good agreement between the experimental value and the Standard Model.

6.3 Extracting the weak mixing angle

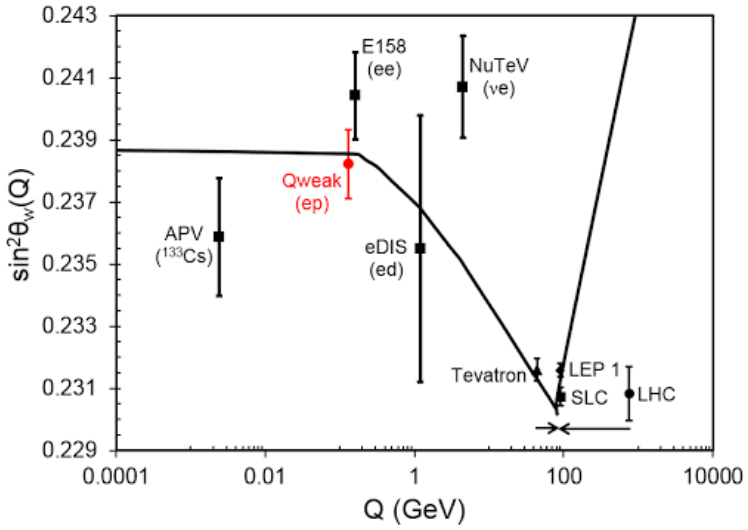

Figure 6.4: The running plot of $\sin^2\theta_W$ versus energy scale Q [11]. The black line represents the Standard Model predicted value ($\overline{MS}$ scheme [85]), with various experimental data points included.

As briefly discussed in chapter 1, the value of Q_w^p is related to the weak mixing angle $\sin^2\theta_W$.

Including radiative effects, this can be written as [48]

$$Q_w^p = (\rho + \Delta_e)(1 - 4\sin^2\theta_W + \Delta_e') + \Box_{WW} + \Box_{ZZ} + \Box_{\gamma Z}. \tag{6.10}$$

Since Q_w^p is suppressed in the Standard Model, a 6.25% measurement of Q_w^p results in a 0.45% precision on $\sin^2\theta_W$ [11]. Figure 6.4 shows the Q_{weak} result for $\sin^2\theta_W$, as well as the Standard Model prediction [48] and several other experimental results both at the Z-pole and at lower Q^2 [85]. Q_{weak} has determined $\sin^2\theta_W$ to be

$$\sin^2\theta_W(Q=0) = 0.2384 \pm 0.0011, \tag{6.11}$$

which has the smallest uncertainty of all the low energy experiments. Again, good agreement with the Standard Model is shown. Even though $\sin^2\theta_W$ is precisely measured at the Z-pole, some models of new physics (for example dark photon models [30]) predict large effects at lower energies, but almost no effect at the Z-pole [11]. While Q_{weak} is not precise enough to confirm or rule out this theory, it does rule out some of the phase space.

6.4 Mass reach and summary

This result has not been included yet in analyses of new physics, but some general model-independent limits on the mass scale of allowed new physics can be made. As shown in the previous section, Q_w^p, Q_W^n , and $\sin^2\theta_W$ are both in good agreement with Standard Model predictions. This already makes TeV scale new physics seem unlikely at first glance. Q_{weak}, since it scatters electrons off of protons, would be sensitive for semi-leptonic new physics which is complementary to previous measurements of which are sensitive primarily to either

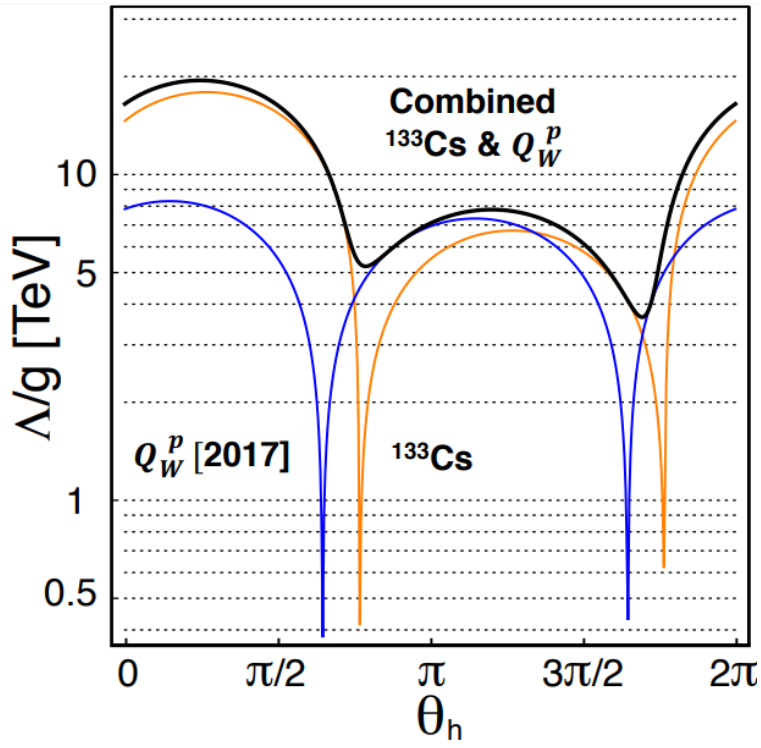

Figure 6.5: The mass reach of the Q_{weak} experiment blue, ^{133}Cs APV in red, and the combined mass reach in black at the 95% confidence level. Λ/g effectively sets the scale of new physics, and θ_{h} is the flavor mixing angle in the Lagrangian for new physics.

purely leptonic new physics (E158 [16]) and different quark linear combinations (^{133}Cs APV [45]).

When discussing searches for new physics, it is helpful to discuss the mass reach. The general form of Standard Model Lagrangian is

$$\mathcal{L}_{\text{SM}}^{\text{PV}} = -\frac{G_F}{\sqrt{2}}\bar{e}\gamma_\mu\gamma_5 e\sum_q C_{1q}\bar{q}\gamma^\mu q. \tag{6.12}$$

The Lagrangian of new physics, which has a similar form to the Standard Model Lagrangian, can be written as

$$\mathcal{L}^{\mathrm{PV}}_{\mathrm{BSM}} = -\frac{g^2}{\Lambda^2}\bar{e}\gamma_\mu\gamma_5 e\sum_q h^q_V \bar{q}\gamma^\mu q, \tag{6.13}$$

where the sum over q is a sum over the up and down quarks, Λ is the mass scale of new physics, g is the coupling, and

$$h^u_V = \cos\theta_h, \tag{6.14}$$

$$h^d_V = \sin\theta_h, \tag{6.15}$$

where θ_h is the flavor mixing angle for coupling of the new physics particle with the up- and down-quark types. The mass reach effectively shows the energy scales of new physics which Q_{weak} has probed and ruled out for comparison to energy frontier experiments.

The mass reach of Q_{weak}, ^{133}Cs APV, and the combined result can be seen in figure 6.5. This shows the Λ/g versus θ_{h} phase space. Q_{weak} rules out new semi-leptonic physics at $\Lambda/g < 7.5$ TeV at 95% confidence level. If one assumes the maximal contact interaction coupling [46] of $g^2 = 4\pi$, then the mass reach of Q_{weak} would become $\Lambda = 26.5$ TeV at the 95% confidence level. The Q_{weak} result will be included in upcoming analyses of new physics.

In experimental nuclear physics, what you don't find can often be as interesting as what you do find. Despite not finding any significant deviations from the Standard Model, Q_{weak} could still play an important role in defining the model of new physics discovered in other experiments. As new, complementary measurements and theory start to be published, Q_{weak}

will have an impact on how these results are interpreted. Q_{weak} has also set the stage for future parity-violating experiments to come which will improve upon techniques developed from this experiment.

Bibliography

[1] How CEBAF Works. URL `https://www.jlab.org/visitors/science/works.html`.

[2] G. Aad et al. The ATLAS Experiment at the CERN Large Hadron Collider. *JINST*, 3:S08003, 2008. doi: 10.1088/1748-0221/3/08/S08003.

[3] Georges Aad et al. Combined Measurement of the Higgs Boson Mass in *pp* Collisions at $\sqrt{s} = 7$ and 8 TeV with the ATLAS and CMS Experiments. *Phys. Rev. Lett.*, 114: 191803, 2015. doi: 10.1103/PhysRevLett.114.191803.

[4] A. Acha et al. Precision Measurements of the Nucleon Strange Form Factors at Q**2 0.1-GeV**2. *Phys. Rev. Lett.*, 98:032301, 2007. doi: 10.1103/PhysRevLett.98.032301.

[5] P. A. Adderley et al. Two Wien Filter Spin Flipper. *Conf. Proc.*, C110328:862–864, 2011.

[6] S. Agostinelli et al. Geant4–a simulation toolkit. *Nuclear Instruments and Methods in Physics Research Section A: Accelerators, Spectrometers, Detectors and Associated Equipment*, 506(3):250 – 303, 2003. ISSN 0168-9002. doi: http://dx.doi.org/10.1016/

S0168-9002(03)01368-8. URL http://www.sciencedirect.com/science/article/pii/S0168900203013688.

[7] Z. Ahmed et al. New Precision Limit on the Strange Vector Form Factors of the Proton. *Phys. Rev. Lett.*, 108:102001, 2012. doi: 10.1103/PhysRevLett.108.102001.

[8] T. Allison et al. The Qweak experimental apparatus. *Nuclear Instruments and Methods in Physics Research Section A: Accelerators, Spectrometers, Detectors and Associated Equipment*, 781(0):105 – 133, 2015. ISSN 0168-9002.

[9] D. Androic et al. Strange Quark Contributions to Parity-Violating Asymmetries in the Backward Angle G0 Electron Scattering Experiment. *Phys. Rev. Lett.*, 104:012001, 2010. doi: 10.1103/PhysRevLett.104.012001.

[10] D. Androic et al. First determination of the weak charge of the proton. *Physical Review Letters*, 111:141803, 2013. doi: 10.1103/PhysRevLett.111.141803. URL http://link.aps.org/doi/10.1103/PhysRevLett.111.141803.

[11] D. Androic et al. Precision Measurement of the Weak Charge of the Proton. submitted.

[12] Androic, D. et al. Qweak: First direct measurement of the proton's weak charge. *EPJ Web Conf.*, 137:08005, 2017. doi: 10.1051/epjconf/201713708005. URL https://doi.org/10.1051/epjconf/201713708005.

[13] K. A. Aniol et al. Measurement of the neutral weak form-factors of the proton. *Phys. Rev. Lett.*, 82:1096–1100, 1999. doi: 10.1103/PhysRevLett.82.1096.

[14] K. A. Aniol et al. Constraints on the nucleon strange form-factors at Q**2 0.1-GeV**2. *Phys. Lett.*, B635:275–279, 2006. doi: 10.1016/j.physletb.2006.03.011.

[15] K. A. Aniol et al. Parity-violating electron scattering from ^{4}He and the strange electric form factor of the nucleon. *Phys. Rev. Lett.*, 96:022003, Jan 2006. doi: 10.1103/PhysRevLett.96.022003. URL `http://link.aps.org/doi/10.1103/PhysRevLett.96.022003`.

[16] P. L. Anthony et al. Precision measurement of the weak mixing angle in Moller scattering. *Phys. Rev. Lett.*, 95:081601, 2005. doi: 10.1103/PhysRevLett.95.081601.

[17] D. S. Armstrong and R. D. McKeown. Parity-Violating Electron Scattering and the Electric and Magnetic Strange Form Factors of the Nucleon. *Ann. Rev. Nucl. Part. Sci.*, 62:337–359, 2012. doi: 10.1146/annurev-nucl-102010-130419.

[18] D. S. Armstrong et al. Strange quark contributions to parity-violating asymmetries in the forward G0 electron-proton scattering experiment. *Phys. Rev. Lett.*, 95:092001, 2005. doi: 10.1103/PhysRevLett.95.092001.

[19] David Armstrong. R_q2 and dR_q2 for Run 1 and Run 2. URL `https://qweak.jlab.org/elog/Analysis+Simulation/1660`.

[20] Kurtis Bartlett and Katherine Mesick. Final Determination of the Effective aluminum window asymmetry(A_b1+-dA_b1) using Monte Carlo method. URL `https://qweak.jlab.org/elog/Analysis+Simulation/1651`.

[21] S. Baunack et al. Measurement of Strange Quark Contributions to the Vector Form Factors of the Proton at Q**2=0.22 (GeV/c)**2. *Phys. Rev. Lett.*, 102:151803, 2009. doi: 10.1103/PhysRevLett.102.151803.

[22] Douglas H. Beck and Barry R. Holstein. Nucleon structure and parity-violating electron scattering. *International Journal of Modern Physics E: Nuclear Physics*, 10(1):1, 2001. ISSN 02183013.

[23] Rakitha S. Beminiwattha. *A Measurement of the Weak Charge of the Proton through Parity Violating Electron Scattering using the Qweak Apparatus: A 21% Result*. PhD thesis, Ohio University, 2013.

[24] Rene Brun and Fons Rademakers. ROOT — an object oriented data analysis framework. *Nuclear Instruments and Methods in Physics Research Section A: Accelerators, Spectrometers, Detectors and Associated Equipment*, 389(1–2):81 – 86, 1997. doi: http://dx.doi.org/10.1016/S0168-9002(97)00048-X.

[25] Cliff Burgess and Guy Moore. *The Standard Model: A Primer*. Cambridge, 2007.

[26] R. D. Carlini et al. The Qweak experiment: A search for new physics at the TeV scale via a measurement of the proton's weak charge, 2007.

[27] R. J. Celotta and D.T. Pierce. Sources of polarized electrons. *Advances in Atomic and Molecular Physics*, 16:101, 1980.

[28] S. Chatrchyan et al. The CMS Experiment at the CERN LHC. *JINST*, 3:S08004, 2008. doi: 10.1088/1748-0221/3/08/S08004.

[29] Juan Carlos Cornejo. *Compton Scattering Polarimetry for the Determination of the Proton's Weak Charge Through Measurements of the Parity-Violating Asymmetry of* ^{1}H*(e,e')p*. PhD thesis, The College of William & Mary, 2016.

[30] Hooman Davoudiasl, Hye-Sung Lee, and William J. Marciano. Muon $g2$, rare kaon decays, and parity violation from dark bosons. *Phys. Rev.*, D89(9):095006, 2014. doi: 10.1103/PhysRevD.89.095006.

[31] Wade Duvall. Final 4 by 4 analysis, . URL `https://qweak.jlab.org/elog/Analysis+Simulation/1428`.

[32] Wade Duvall. [W-shutter] complete runlist, . URL `https://qweak.jlab.org/elog/Analysis+Simulation/697`.

[33] Wade Duvall. [W-shutter] Regressed asymmetries and correlations from high gain study, . URL `https://qweak.jlab.org/elog/Analysis+Simulation/726`.

[34] Wade Duvall. [W-shutter] Fractional yields in blocked MD's in 'good' halo conditions, . URL `https://qweak.jlab.org/elog/Analysis+Simulation/779`.

[35] Wade Duvall. [W-shutter] Background detector yields during run 'high gain' study (with normal/unblocked yields), . URL `https://qweak.jlab.org/elog/Analysis+Simulation/783`.

[36] Wade Duvall. W-Shutter test results, . URL https://qweak.jlab.org/DocDB/0023/002373/014/MD_Asymmetries_Summary.pdf.

[37] Wade S. Duvall. Uslumi pedestals over run1 and run2, . URL https://qweak.jlab.org/elog/Analysis+%26+Simulation/1257.

[38] Wade S. Duvall. Lumi pedestal over time, . URL https://qweak.jlab.org/elog/Analysis+Simulation/481.

[39] Wade S. Duvall. Background detector asymmetries for run ii, . URL https://qweak.jlab.org/elog/Analysis+Simulation/505.

[40] Wade S. Duvall. Background detector correlations and main detectors, . URL https://qweak.jlab.org/elog/Analysis+Simulation/534.

[41] Wade S. Duvall. Background detector yields during 'good halo' study (with normal/unblocked yields), . URL https://qweak.jlab.org/elog/Analysis+Simulation/786.

[42] Wade S. Duvall. [w-shutter] run 2 correlations, . URL https://qweak.jlab.org/elog/Analysis+Simulation/836.

[43] Wade S. Duvall. General issues, current, lumi mapfile history, . URL https://qweak.jlab.org/elog/Management/8.

[44] Wade S. Duvall. Main detector and background detector asymmetry correlation and uslumi widths. Q_{weak} Collaberation Meeting, April 2012. URL https://qweak.jlab.org/DocDB/0016/001626/001/lumi_width.pdf.

[45] V. A. Dzuba, J. C. Berengut, V. V. Flambaum, and B. Roberts. Revisiting parity non-conservation in cesium. *Phys. Rev. Lett.*, 109:203003, 2012. doi: 10.1103/PhysRevLett.109.203003.

[46] E. Eichten, Kenneth D. Lane, and Michael E. Peskin. New Tests for Quark and Lepton Substructure. *Phys. Rev. Lett.*, 50:811–814, 1983. doi: 10.1103/PhysRevLett.50.811. [,369(1983)].

[47] F. Englert and R. Brout. Broken Symmetry and the Mass of Gauge Vector Mesons. *Phys. Rev. Lett.*, 13:321–323, 1964. doi: 10.1103/PhysRevLett.13.321.

[48] Jens Erler, Andriy Kurylov, and Michael J Ramsey-Musolf. The Weak charge of the proton and new physics. *Phys. Rev.*, D68:016006, 2003. doi: 10.1103/PhysRevD.68.016006.

[49] Ciprian Gal. PMTDD: Microscopic Mott Scattering and effective models. URL `https://qweak.jlab.org/DocDB/0024/002411/001/170113_CollMtg_GPR_PhaseSpace_CGal.pdf`.

[50] Ciprian. Gal et al. Qweak DD studies. in preparation.

[51] David Gaskell. Run 2 final polarizations - updated proposal. URL `https://qweak.jlab.org/elog/DAQ+Analysis/334`.

[52] Valerie Gray. LH2 in Run 1 and Run 2 configurations with the W Shutter - # hits and <PE>. URL `https://qweak.jlab.org/elog/Analysis+Simulation/911`.

[53] Jeremy Green, Stefan Meinel, Michael Engelhardt, Stefan Krieg, Jesse Laeuchli, John Negele, Kostas Orginos, Andrew Pochinsky, and Sergey Syritsyn. High-precision calculation of the strange nucleon electromagnetic form factors. *Phys. Rev.*, D92(3):031501, 2015. doi: 10.1103/PhysRevD.92.031501.

[54] M. Hauger et al. A High precision polarimeter. *Nucl. Instrum. Meth.*, A462:382–392, 2001. doi: 10.1016/S0168-9002(01)00197-8.

[55] Peter W. Higgs. Broken symmetries, massless particles and gauge fields. *Phys. Lett.*, 12:132–133, 1964. doi: 10.1016/0031-9163(64)91136-9.

[56] T. M. Ito et al. Parity violating electron deuteron scattering and the proton's neutral weak axial vector form-factor. *Phys. Rev. Lett.*, 92:102003, 2004. doi: 10.1103/PhysRevLett.92.102003.

[57] Michael Gericke Jie Pan. Benchmarking Light Yield in QweakSimG4. URL `https://qweak.jlab.org/DocDB/0023/002305/003/CollabMeetFeb2016-PMTDD_FocusSession.pdf`.

[58] Donald C. Jones. *Measuring the Weak Charge of the Proton via Elastic Electron-Proton Scattering*. PhD thesis, The University of Virginia, 2015.

[59] Emmanouil Kargiantoulakis. Proposed Beamline Background Corrections, Run1 and Run2, . URL `https://qweak.jlab.org/elog/Analysis+Simulation/1652`.

[60] Emmanouil Kargiantoulakis. Beamline Backgrounds Correction, . URL https://qweak.jlab.org/DocDB/0023/002390/001/16-11-14_BeamlineBackgrounds.pdf.

[61] Emmanouil Kargiantoulakis. *A Precision Test of the Standard Model via Parity-Violating Electron Scattering in the Qweak Experiment*. PhD thesis, The University of Virginia, 2015.

[62] Manolis Kargiantoulakis. USLumi signal composition, . URL https://qweak.jlab.org/elog/Analysis+Simulation/1157.

[63] Paul King. Update for the Run1 and Run2 Transverse Asymmetry Leakage error contributions, . URL https://qweak.jlab.org/elog/Analysis+Simulation/1663.

[64] Paul King. Summary of blinding factor algorithm, . URL https://qweak.jlab.org/elog/Management/24.

[65] John D. Leacock II. *Measuring the Weak Charge of the Proton and the Hadronic Parity Violation of the $N \rightarrow \Delta$ Transition*. PhD thesis, Virginia Polytechnic Institute and State University, 2012.

[66] John Poague Leckey IV. *The First Direct Measurement of the Weak Charge of The Proton*. PhD thesis, College of William & Mary, 2012.

[67] T. D. Lee and Chen-Ning Yang. Question of Parity Conservation in Weak Interactions. *Phys. Rev.*, 104:254–258, 1956. doi: 10.1103/PhysRev.104.254.

[68] C. W. Leemann, D. R. Douglas, and G. A. Krafft. The Continuous Electron Beam Accelerator Facility: CEBAF at the Jefferson Laboratory. *Ann. Rev. Nucl. Part. Sci.*, 51:413–450, 2001. doi: 10.1146/annurev.nucl.51.101701.132327.

[69] F. E. Maas et al. Measurement of strange quark contributions to the nucleon's form-factors at Q**2 = 0.230-(GeV/c)**2. *Phys. Rev. Lett.*, 93:022002, 2004. doi: 10.1103/PhysRevLett.93.022002.

[70] F. E. Maas et al. Evidence for strange quark contributions to the nucleon's form-factors at q**2 = 0.108 (GeV/c)**2. *Phys. Rev. Lett.*, 94:152001, 2005. doi: 10.1103/PhysRevLett.94.152001.

[71] Scott MacEwan. *The Weak Charge of the Proton: A Search For Physics Beyond the Standard Model*. PhD thesis, University of Manitoba, 2015.

[72] David Mack and JaiWei Mei. Beam Current Normalization Issues Part II. URL `https://qweak.jlab.org/DocDB/0013/001369/001/BCMLinearityMarch2011.pdf`.

[73] Joshua Magee. *A Measurement of the Parity-Violating Asymmetry in Aluminum and its Contribution to a Measurement of the Proton's Weak Charge*. PhD thesis, The College of William & Mary, 2016.

[74] Robert Mahurin. Description of Qweak PMT linearity tests using the EEL126 test stand., . URL `https://qweak.jlab.org/DocDB/0018/001838/001/eeltest.mahurin.pdf`.

[75] Robert Mahurin. Linearity measurements in the main detectors: an update, . URL https://qweak.jlab.org/DocDB/0016/001696/002/2012-08-02.md_3led.pdf.

[76] Juliette Mammei. *Parity-Violating Elastic Electron Nucleon Scattering: Measurement of the Strange Quark Content of the Nucleon and Towards a Measurement of the Weak Charge of the Proton*. PhD thesis, Virginia Polytechnic Institute and State University, 2010.

[77] Martin J. McHugh III. *A Measurement of the Transverse Asymmetry in Forward-Angle Electron-Carbon Scattering Using the Q_{weak} Apparatus*. PhD thesis, The George Washington University, 2017.

[78] M. J. Musolf, T. W. Donnelly, J. Dubach, S. J. Pollock, S. Kowalski, and E. J. Beise. Intermediate-energy semileptonic probes of the hadronic neutral current. *Phys. Rept.*, 239:1–178, 1994. doi: 10.1016/0370-1573(94)90040-X.

[79] Katherine E. Myers. *The First Determination of the Proton's Weak Charge Through Parity-Violating Asymmetry Measurements in Elastic e + p and e + Al Scattering*. PhD thesis, The George Washington University, 2012.

[80] A. Narayan et al. Precision Electron-Beam Polarimetry at 1 GeV Using Diamond Microstrip Detectors. *Phys. Rev.*, X6(1):011013, 2016. doi: 10.1103/PhysRevX.6.011013.

[81] Victoria Owen. MD Optical Response Simulations. URL https://qweak.jlab.org/elog/Detector/160427_105527/PMTDD_XChange.pdf.

[82] Jie Pan. Hit maps at the front surface of Pb pre-radiator generated from LH2 simulation (all octants). URL https://qweak.jlab.org/elog/Detector/117.

[83] Jie Pan. *Towards a Precision Measurement of Parity-Violating e-p Elastic Scattering at Low Momentum Transfer*. PhD thesis, University of Manitoba, 2012.

[84] Kent Paschke. PMT-DD with effective models. URL https://qweak.jlab.org/elog/Detector/124.

[85] C. Patrignani et al. Review of Particle Physics. *Chin. Phys.*, C40(10):100001, 2016. doi: 10.1088/1674-1137/40/10/100001.

[86] Mark Pitt. Qweak Beamline Background, . URL https://qweak.jlab.org/DocDB/0022/002231/003/pitt_jlab_brief_aug_21.pdf.

[87] Mark Pitt. Qweak Beamline Background Summary, . URL https://qweak.jlab.org/DocDB/0022/002228/001/pitt_beamline_summary_aug_2015.pdf.

[88] Mark Pitt and Wade Duvall. Wiki-Update: $A_{nmiscarity}$. URL https://qweak.jlab.org/DocDB/0023/002380/001/pitt_nmiscarity_nov_2016_collab_meet.pdf.

[89] C.K. Sinclair, P.A. Adderley, B.M. Dunham, J.C. Hansknecht, P. Hartmann, M. Poelker, J.S. Price, P.M. Rutt, W.J Schneider, and M. Steigerwald. Development of a high average current polarized electron source with long cathode operational lifetime. *Physical Review Special Topics - Accelerators and Beams*, 10:023501, 2007.

[90] D. T. Spayde et al. The Strange quark contribution to the proton's magnetic moment. *Phys. Lett.*, B583:79–86, 2004. doi: 10.1016/j.physletb.2004.01.002.

[91] Adesh Subedi. *Determination of the weak charge of the proton through parity violating asymmetry measurements in the elastic e+p scattering.* PhD thesis, Mississippi State University, 2014.

[92] Till Tantau. *The TikZ and PGF Packages.* URL `http://sourceforge.net/projects/pgf/`.

[93] Buddhini Waidyawansa. Studying the electron entrance angle dependance of pe's in a bare bar, . URL `https://qweak.jlab.org/elog/Analysis+Simulation/1538`.

[94] Buddhini Waidyawansa. Transverse Leakage Error For the Full Run, . URL `https://qweak.jlab.org/DocDB/0022/002245/006/BPW_AT_Leakage_talk_10_02_2015_updated.pdf`.

[95] D. Buddhini P. Waidyawansa. *A 3% Measurement of the Beam Normal Single Spin Asymmetry in Forward Angle Elastic Electron-Proton Scattering using the Qweak Setup.* PhD thesis, Ohio University, 2013.

[96] Peiqing Wang. *A Measurement Of The Proton's Weak Charge Using An Integration Čerenkov Detector System.* PhD thesis, University of Manitoba, 2011.

[97] William A. Watson III, Jie Chen, Graham Heyes, Edward Jastrzembski, and David Quarrie. Coda: A scalable, distributed data acquisition system. In *Proceedings of the Real Time Conference, 1993*, page 296, 1993.

[98] Steven Weinberg. A Model of Leptons. *Phys. Rev. Lett.*, 19:1264–1266, 1967. doi: 10.1103/PhysRevLett.19.1264.

[99] C. S. Wood, S. C. Bennett, D. Cho, B. P. Masterson, J. L. Roberts, C. E. Tanner, and Carl E. Wieman. Measurement of parity nonconservation and an anapole moment in cesium. *Science*, 275:1759–1763, 1997. doi: 10.1126/science.275.5307.1759.

[100] C. S. Wu, E. Ambler, R. W. Hayward, D. D. Hoppes, and R. P. Hudson. Experimental Test of Parity Conservation in Beta Decay. *Phys. Rev.*, 105:1413–1414, 1957. doi: 10.1103/PhysRev.105.1413.

[101] C. Yan, R. Carlini, and D. Neuffer. Conference Proceedings CC930517. page 2136, 1993.

[102] R. D. Young, R. D. Carlini, A. W. Thomas, and J. Roche. Testing the standard model by precision measurement of the weak charges of quarks. *Phys. Rev. Lett.*, 99:122003, Sep 2007. doi: 10.1103/PhysRevLett.99.122003. URL `http://link.aps.org/doi/10.1103/PhysRevLett.99.122003`.

[103] Peng Zang. Natural Monitor Variables I - Monitor Width Comparison, . URL `https://qweak.jlab.org/elog/Analysis+Simulation/1444`.

[104] Peng Zang. Natural Monitor Variables 0 - Definition and Procedure, . URL https://qweak.jlab.org/elog/Analysis+Simulation/1451.

[105] Peng Zang. Natural Monitor Variables III - Regression and Dithering Correction Comparison, . URL https://qweak.jlab.org/elog/Analysis+Simulation/1454.

[106] Peng Zang. Natural Monitor Variables VI - "Beam Correction" to Beam Position Monitors, . URL https://qweak.jlab.org/elog/Analysis+Simulation/1483.

[107] Peng Zang. Renormalized Main Detector - Null and Physics Asymmetries, . URL https://qweak.jlab.org/elog/Analysis+%26+Simulation/1558.

[108] Peng Zang. PMTDD - Dither Corrected Results, . URL https://qweak.jlab.org/elog/Analysis+Simulation/1576.

[109] Peng Zang. Tentative Quantization of Regression and Dithering Discrepancy, . URL https://qweak.jlab.org/elog/Analysis+Simulation/1588.

[110] Peng Zang. Final dataset - from pass5c to pass5c+, . URL https://qweak.jlab.org/elog/Analysis+%26+Simulation/1629.

[111] Peng Zang. BCM Renormalization (Pass5c+), . URL https://qweak.jlab.org/DocDB/0023/002344/010/BCM_Normalization_in_RUN1_and_RUN2_Pass5c%2B_new_mdMrn_norm.pdf.

[112] Peng Zang. Beam Correction Summary, . URL https://qweak.jlab.org/DocDB/0023/002376/006/Beam_Correction_Summary.pdf.

[113] Peng Zang. Main Detector Asymmetry Summary, . URL https://qweak.jlab.org/DocDB/0023/002373/014/MD_Asymmetries_Summary.pdf.

Appendices

Appendix A

Software breakdown and documentation

A.1 Database rootfiles

The database rootfile (a rootfile is a data structure provided by the ROOT data analysis framework [24]) was written solely by the author of this dissertation with guidance from P. King and K. Paschke. Prior to the creation of the database rootfiles, in order to conduct analysis, data had to be extracted from a MySQL database. This created several problems. First, it required a certain amount of expertise just to get the data you needed. Second, the database queries could take quite some time to produce the needed data. If several collaborators were extracting data at the same time, this process would slow even further.

Third, and possibly most important, slight variations in the MySQL query could result in slight variations in datasets. This could cause issues when comparing results causing people to spend time finding the cause of variations. In rare cases, the entirely wrong dataset would be used.

The idea behind the database rootfile was to store all of the runs that passed a certain set of cuts (described below) in a single rootfile. One rootfile would be generated per regression scheme. Within a single dataset, the ROOT friending feature (which allows you to effectively combine rootfiles for analysis) could be used to do analysis using more than one regression set. This guarantees that the entire collaboration is using the same dataset. Rootfiles that contained the slopes and normalized PMT yields were also generated.

Table A.1: Cuts used for determining the runlets for the database rootfile for production datasets. For ancillary data sets, the target, run quality and good for could be changed.

MySQL column	MySQL table	value
`quality_id`	`runlet`	'1'
`good_for_id`	`run`	contain '1' and '3'
`slope_correction`	`analysis`	'off'
`slope_calculation`	`analysis`	'off'
`target_position`	`slow_controls_settings`	'HYDROGEN-CELL'

The cuts used to produce good production datasets can be see in table A.1. For ancillary data sets, the `target_position` could be changed. Since the `quality_id` and `good_for_id` were never reliably set during these ancillary periods, most groups produced a list of runs to be included. The rootfile generator could read in this list and would only select those runs.

Table A.2: Sign correction determination for a given IHWP and wien reversal.

precession_reversal	wien_reversal	ihwp_setting	sign_correction
normal	normal	out	1
normal	normal	in	-1
normal	reverse	out	-1
normal	reverse	in	1
reverse	normal	out	-1
reverse	normal	in	1
reverse	reverse	out	1
reverse	reverse	in	-1

Once a runlist was created, data was extracted from the `md_data`, `lumi_data`, and `beam` tables. Which detectors were extracted was controlled by a series of mapfiles. These were parsed by a simple, custom parser.

Aside from extracted data from the Q_{weak} MySQL database, a sign correction to correct for all slow helicity reversals was computed and inserted into the database. This took into account the `wien_reversal`, `precession_reversal`, and `ihwp_setting` from the `slow_controls_settings` table. Values of how this is computed can be seen in table A.2. This allowed a collaboration wide standard for sign correction to be used.

The database rootfiles proved to be a very useful tool used by the entire collaboration. They allowed quick access to data with only basic knowledge of ROOT. The beam modulation group, who ultimately did not use the MySQL database adopted a similar model of storing results that was friendable to the database rootfiles.

The code for the database rootfile generator can be found in the Q_{weak} SVN repository under `Extensions/QwDBTree`.

Appendix B

Personal Contributions

As with many dissertations resulting from work done by a large collaboration, this dissertation strives to tell the whole story of the Q_{weak} experiment, not just the fragments which represent the work of the author. As such, much of the work here was done by many people across many institutions (see published works [10, 11] for a complete author list). This appendix will detail the work which I contributed or for which I was solely responsible.

B.1 Hardware

I joined the Q_{weak} collaboration in May 2011, which was well after the installation of the apparatus, but during the 6 month down time for accelerator upgrades. During this time I helped to overhaul the luminosity monitors, particularly the downstream luminosity moni-

tors, which where completely rebuilt to replace radiation damaged parts and reattach the preradiators. This effort was assisted by J. Leacock, A. Lee, and M. Pitt.

During run 2, I was the primary contact for maintenance for the luminosity monitors. When the apparatus was switched from integration mode to tracking mode I was responsible for changing over the luminosity monitor bases (although sometimes this was done by M. Pitt). I also made a few accesses to perform emergency maintenance on the luminosity monitor. These repairs had to be quickly (usually swapping out a PMT base) due to the high radiation environment. Over the course of the experiment I received 100 mrem dose, mostly during repairs.

During run 2, I also took over 300 hours of shifts as either shift leader or target operator. This involved making sure the data taking went smoothly as shift leader and making sure the target stayed within safe operating parameters as target operator.

After the running was completed, I worked on measuring the nonlinearity of the main detectors using a bench test. While I led this effort, I was assisted by A. Lee and M. Pitt. Both hardware and software changes were made to the DAQ to make this possible. These changes were made primarily by P. King with assistance from me. M. Pitt and myself also conducted a number of studies to determine the main detector nonlinearity.

B.2 Analysis contributions

There may be some overlap between this section and appendix B.4, which details my contributions to the Q_{weak} body of software. Near the end of run 2 and after, I worked closely with the beamline background group, particularly E. Kargiantoulakis (who was ultimately in charge of producing the final correction). During run 2, along with S. MacEwan, I planned and executed several background studies with the tungsten shutters. I was also in charge of analysis of this dataset. I helped with the early luminosity monitor studies which helped establish their role as an important background detector.

I also worked closely with the beam correction group, in charge of correcting for helicity-correlated beam effects. I was in charge of a series of analyses studying charges slopes. This included the special 4-by-4 period which required changes to the analysis engine. Once it was determined that charge regression would not be suitable to determine nonlinearity, M. Pitt and I were responsible for analysing the data from nonlinearity bench studies and ultimately producing the nonlinearity. The analysis of the nonlinearity data was conducted by me with guidance and input from M. Pitt. I also assisted in some early studies on beam position differences and slopes.

I was involved with with the pass5b replay as well as the pass5c data quality updates. I helped submit jobs and check that they succeeded. I also made sure all the luminosity monitor mapfiles were properly defined for all the failure periods for both the analyser and

regression. For pass5c, I was in charge of taking all the run quality changes and updating values in the MySQL database. I also assisted in the replay of many smaller datasets.

While studying upstream luminosity monitor failure and how to define detector asymmetries during failed periods, I inadvertently discovered the secondary scattering effect caused by the lead preradiator. Aside from the discovery, I also used the 4-by-4 data set to confirm the source of the effect was in the lead, helped to study how the effect changes over time, and worked extensively with the effective models, particularly producing results from new hitmaps and light parameterizations from other members of the secondary scattering group (C. Gal, J. Pan, K. Paschke).

B.3 Simulation

Aside from the work on QwGeant4 described in section B.4, I also ran several simulations. Simulations studying the signal fractions from the beamline collimator in both luminosity monitors and main detectors were run and analysed by me. This work would not have been possible without updated beamline collimator implemented by M. McHugh and guidance from the simulation group. I also ran several simulations to assist with various acceptance corrections and for theory comparisons. I was responsible for all simulations and analysis involving the upstream and downstream luminosity monitors.

B.4 Software

When I joined Q_{weak} in May 2011, the corpus of the software already existed. I did, however, make important contributions to the three main pieces of Q_{weak} software: QwAnalysis, which processed raw data files and produced asymmetries, linRegBlue, which did linear regression and beam modulation, and QwGeant4, the Q_{weak} Geant4 simulation. One of my most important contributions was the database rootfile, discussed in appendix A.1.

B.4.1 QwAnalysis

I made a few small changes to the base code of the analyser mostly involving charge normalization in the luminosity monitors, and other small contributions. Some improvements were also made into how data was inserted into the MySQL database. I also contributed to a standard set of scripts included with the analyser which showed how to interact with the database and extract data in ROOT for analysis.

My biggest contributions to the QwAnalysis software was updating mapfiles. Mapfiles stored various PMT to detector mappings and defined various variables used or produced in the analysis. This process involved checking if runs failed (a group effort), then looking at log files to determine the reason for the failure, and then updating the mapfile.

B.4.2 linRegBlue

My contributions to linRegBlue are similar to that of QwAnalysis. I updated the base linRegBlue scripts to account for changes in detector status and defined several new regression sets. Additionally, for the tungsten shutter data set, I implemented a custom version of linRegBlue to allow regression of these runs using a variety of different slopes (i.e. using unblocked slopes to regress blocked runs).

B.4.3 QwGeant4

I was also in charge of implementing both the upstream and downstream luminosity monitors in QwGeant4. I received invaluable input from K. Bartlett, W. Deconinck, and M. McHugh. Despite not attempting a realistic implementation with photoelectron counting, this was a large effort including a lot of overhead required by Geant4 to implement detectors. I also assisted with a various number of small simulation tasks including adding some variables and making changes to the code to run a few specialized simulations.